Regulation of In Vivo Mitochondrial Energetics by Oxidative Stress throughout Life: A Multi-Modal Spectroscopy Approach

Michael Patrick Siegel

A dissertation

submitted in partial fulfillment of the

requirements for the degree of

Doctor of Philosophy

University of Washington

2012

Reading Committee:

David Marcinek, Chair

Martin Kushmerick

Michael Regnier

Kenneth Schenkman

Program Authorized to Offer Degree:

Bioengineering

University of Washington

Abstract

Regulation of In Vivo Mitochondrial Energetics by Oxidative Stress throughout Life:

A Multi-Modal Spectroscopy Approach

Michael P. Siegel

Chair of Supervisory Committee:

David J. Marcinek, Research Associate Professor

Department of Radiology, Adjunct of Bioengineering

Age-related skeletal muscle degeneration contributes to lost quality of life and an increased health care burden for the aging population. At the crossroads of energy production, cell signaling, and free-radical production, mitochondria are implicated in this loss of skeletal muscle function with age. Here we test the hypothesis that in vivo mitochondrial function is depressed in old organisms as a result of reversible modulation by oxidative stress rather than irreversible accumulation of oxidative damage to proteins, lipids, and DNA. Oxidative stress-induced reduction of mitochondrial coupling efficiency has been implicated as a negative feedback mechanism responsible for mitigating mitochondrial reactive oxygen species production, and provides a possible link between age-related oxidative stress and age-related loss of function. To measure in vivo mitochondrial energetics on a timescale compatible with fluctuations in oxidative stress, we present a multi-modal system for simultaneous measurements of metabolite concentrations using ^{31}P magnetic resonance spectroscopy and tissue oxygenation using near infrared optical spectroscopy in mouse skeletal muscle. Using this technique we demonstrate the reduction of mitochondrial coupling efficiency (P/O ratio) in a pharmacological (paraquat treatment) model of

oxidative stress in the absence of intrinsic mitochondrial defects, with a similar responses in genetic (CuZn-superoxide dismutase knock-out and glutathione deficient) models. We find that this phenomenon persists throughout life, but that the energetic consequences of depressed mitochondrial efficiency become amplified by age. By treating old mice with the mitochondrial-targeted antioxidant SS31 we demonstrate that depressed mitochondrial function is a reversible phenomenon of aging, as mitochondrial energetics were rapidly restored to young levels. SS31-treatment also improved in situ muscle fatigue and live endurance capacity in old mice, indicating that the rapid recovery of mitochondrial energetics has important implications for improving physical ability of aged organisms. This work demonstrates a powerful new technology for measuring acute metabolic changes in vivo, a new way of thinking about age-related functional losses, and a promising suggestion that targeting mitochondrial oxidative stress with SS31 will have therapeutic benefits for aging humans.

Table of Contents

List of Figures

List of Tables

Acknowledgements

Special thanks to everyone that contributed to this work. In no particular order: Tim Wilbur, Mark Mathis, and Atlas Trieu for contributing tremendous quality work to the assembly of both multi-modal spectroscopy systems, with special thanks to Tim for moving the art of mouse ischemia cuff construction into the 21st century; Donghoon Lee, Eric Shankland, and Lynne Spencer for expanding my knowledge and ability in the field of magnetic resonance research; Rudy Stuppard for the countless rounds of HPLC, westerns, gels, and surgeries, as well as the general education in doing good bench work; Shane Kruse for executing much of the ex vivo respirometry data presented here and then teaching me how to do the rest - plus the Amplex Red assay that got slid into Chapter 5 at the last minute; Gary Knowels for the treatments, gels, surgeries, MouseOx experiments, and general willingness to help with anything at any time; Mary-Ellen Harper, Terry Kavanagh, Holly van Remmen, and Hazel Szeto for the contribution of mouse models and materials; Heather Hopkins for nine long rounds of afterhours Rotarod; Justin Percival for his diligence conducting in situ fatigue tests; everybody that contributed any portion of as much as one experiment or analysis that became all or part of a figure presented here, including Glen Banks, Daniel Chen, Jorming Goh, Martha Mathiason, Dave Niles, Wenbo Qi, Adam Salmon, and Collin White; my committee for providing constructive guidance and support at every step along the way; and of course my family and friends who put up with me day in and day out.

Final, special thanks to my advisor, Dave Marcinek, for taking me on as his first graduate student and seeing this through with me all the way to the end.

Chapter 1

Introduction

Human life expectancy has increased dramatically over the past century (13). Due to improved methods for treating or preventing typically life-ending conditions such as cancer, heart disease, and diabetes, humans are routinely living long enough to experience the debilitating effects of age. Considering skeletal muscle alone, the symptoms associated with age include wasting, weakness, and fatigue, accounting for reduced quality of life and increased dependence on care-givers (180). These effects exact a debilitating toll on individuals and health-care systems worldwide (2).

Put forth by Denham Harman in 1956 (64), the free radical theory of aging was one of the earliest theories to try and explain the etiology of age-related decline. This theory proposed that exposure to free radicals generated by cellular metabolism causes oxidative damage to macromolecules like proteins and nucleic acids, and results in the degenerative manifestations of age. In 1972 Harman extended his theory to implicate reactive oxygen species (ROS) generated by mitochondria, the "cellular powerhouses", as the free radicals responsible for this oxidative damage (65). While this theory was accepted by many, recent data has clouded the notion that age-related decline is a manifestation of oxidative damage alone. Significantly, positive benefits of ROS and oxidative stress have been realized in the regulation of important cellular processes including mitochondrial biogenesis (140), activation of antioxidant defenses (52, 62), and the beneficial adaptations associated with exercise (57, 144). In addition, establishing a direct link between the magnitude of age-related oxidative stress, the level of oxidative damage to macromolecules, and the degree of functional losses in aged organisms has been difficult (39, 162). Finally, antioxidant treatments have found limited success in extending lifespan (78, 181, 194).

This murkiness in the relationship between oxidative damage and age has led aging research in a new direction. The free radical theory of aging has evolved to yield the "oxidative stress hypothesis of aging" suggesting that oxidative regulation of gene expression by genetic and epigenetic means is responsible for the presentation of an aged genetic program (161), and the "redox stress hypothesis of aging" which implicates redox-sensitive changes to signaling proteins as reversible mechanisms by which an oxidative cellular environment can depress function (162). A number of oxidation-sensitive post-translational modifications have been found to modulate function independent of damage, particularly involving cysteine residues in metabolic enzymes (80, 109). Taken together a story begins to emerge that cell function may be reversibly modulated by a shift in the oxidative environment of aged tissues rather than irreversibly compromised by oxidative damage.

Persistent evidence does support the notion that tissues in aged organisms are oxidatively stressed due to an imbalance favoring pro- over anti-oxidant processes (96, 141, 163). As a result, significant attention has remained on mitochondria as important players in the aging process. Mitochondria are responsible for generating the majority of the cell's ATP as well as a significant portion of the cell's ROS (167) through the processes of oxidative phosphorylation. As illustrated in Fig. 1.1, a collection of five membrane-bound protein complexes (complexes I-V) in the inner mitochondrial membrane (IMM) constitute the electron transport chain (ETC), which translates energy from carbon-based energy sources into a proton gradient across the IMM. The majority of the electrochemical energy stored by this proton gradient is coupled to the synthesis of ATP by the F_0F_1 ATPase (complex V), while a small percentage is dissipated as heat when protons bypass complex V in a process called uncoupling (19, 121). Along the way a small percentage of molecular oxygen can be errantly reduced at complexes I and III to form superoxide anion, a short-lived member of the ROS family (165). Due to the link between electron flux

through the ETC and the proton gradient across the IMM, the rate of electron transfer slows under conditions when this gradient is steepest (i.e. high IMM potential, $\Delta\psi$), and the probability of forming superoxide increases (121). Thus, high $\Delta\psi$ facilitates production of ATP while low $\Delta\psi$ mitigates ROS production and reduces oxidative stress.

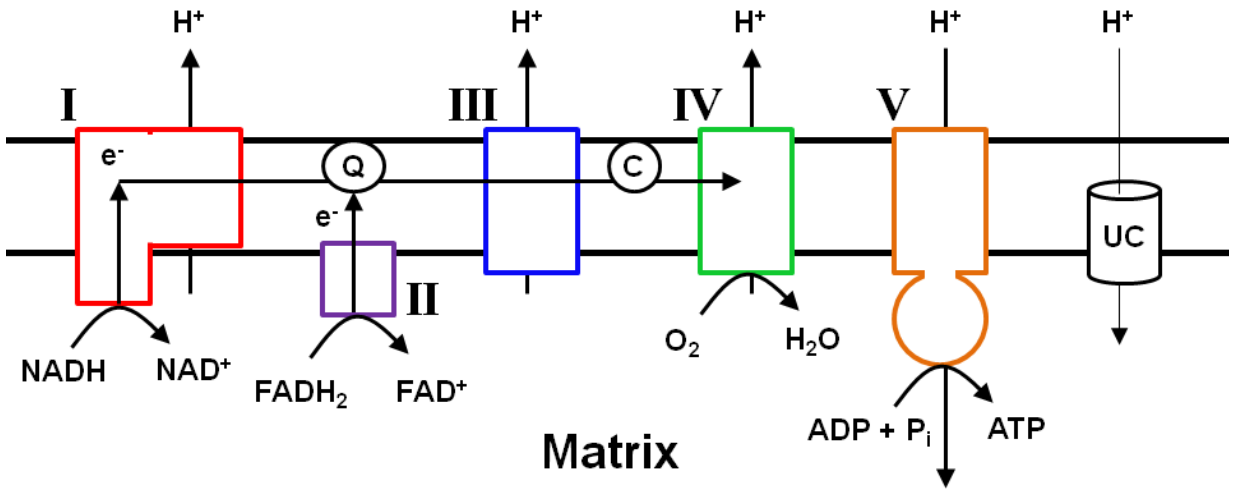

Figure 1.1. Generated by catabolism of carbon-based fuel sources, the reduced cofactors NADH and $FADH_2$ donate electrons to the ETC at complexes I and II, respectively. These electrons are passed along the ETC in a series of redox reactions, linked to proton-pumping at complexes I, III, and IV which move protons out of the mitochondrial matrix. The energy stored in the electrochemical gradient generated by this pumping action is harnessed to synthesize ATP at complex V or dissipated by uncoupling (UC). Lipid-soluble ubiquinone (Q) shuttle electrons between complexes I/II and III, and water soluble cytochrome c (C) shuttles electrons between complexes III and IV.

Depressed mitochondrial function is a hallmark of aging and is often blamed on self-induced oxidative damage (26, 77, 124, 130, 142). However, the role of mitochondrial metabolism in generating ROS also makes mitochondria a key regulator of the oxidative environment, and a probable site for ROS-mediated mechanisms that modulate function. Receiving particular attention over the past 20 years, is a hypothesis suggesting that oxidative homeostasis is maintained by a negative feedback loop involving ROS and mitochondrial coupling efficiency (20, 159). This hypothesis suggests that oxidative stress induces mild

uncoupling, thereby reducing ROS production at the cost of a slight reduction in ATP production efficiency. The precise mechanism responsible for this scheme is under dispute, and much research attention has been devoted to the family of recently discovered uncoupling proteins (UCP1-5) in this process (45, 66, 175, 179). Such a mechanism complicates the role of mitochondria in aging, as ostensibly depressed mitochondrial function (i.e. $\downarrow\Delta\psi$ and reduced coupling efficiency) may result from physiological regulation of mitochondrial efficiency by oxidative stress rather than pathological oxidative damage.

While data supporting such a scenario has been mounting, acceptance of this mechanism would represent a shift in our understanding of the aging process. Complicating the matter, limited methods for observing mitochondria as they respond to changes in an intact cellular environment has made firm scientific conclusions elusive (21). Typical approaches for studying mitochondrial function rely on histological or biochemical assessments of mitochondrial form, content, or damage (18, 96, 126, 131) and ex vivo approaches that assess mitochondrial respiration(61), membrane potential (82, 150), or ROS production (63, 185). These approaches represent powerful tools to characterize intrinsic mitochondrial qualities outside the body or in cultured tissue, but they are poorly suited for measuring physiological modulations in vivo. ROS are generally short-lived molecules (138) that initiate complex physiological changes (14, 47, 194) that are difficult to recreate and measure in an ex vivo medium. As a result, the limitations of existing ex vivo methodology bear particular significance for studying the relationship between mitochondria and oxidative stress.

The work presented here overcomes this limitation with a novel in vivo approach that uses simultaneous magnetic resonance and optical spectroscopy to measure mitochondrial metabolism in mouse skeletal muscle. This technology is used to test the hypothesis that oxidative stress regulates mitochondrial

coupling efficiency in vivo, which would support a novel explanation for age-related changes in mitochondrial function and associated debilitation.

Dissertation Overview

The body of this dissertation takes the form of four chapters, the final three of which represent work that has been published, is under review for publication, or is currently in preparation for submission. Chapter 2 presents the development and validation of a multi-modal spectroscopy system capable of characterizing in vivo mitochondrial metabolism over the course of a single, one-hour experiment. Chapters 3 through 5 harness the benefits of this unique approach to study the relationship between oxidative stress and in vivo mitochondrial function in the context of aging. In Chapter 3, the fundamental notion of oxidative stress-control of mitochondrial efficiency is tested by pharmacologically and genetically inducing oxidative stress in young mice and using in vivo spectroscopy to observe the manner in which mitochondrial energetics are regulated. Chapter 4 extends the pharmacological strategy employed in Chapter 3 to determine whether mitochondrial regulation by oxidative stress remains a relevant physiological phenomenon through old age. In Chapter 5, a therapeutic intervention is used to exploit the notion that depressed function of old mitochondria is a consequence of the oxidative environment rather than oxidative damage. Old mice are treated with a mitochondrial-targeted antioxidant and the benefits of this treatment are characterized at the mitochondrial and whole organism level. Concluding remarks are provided in Chapter 6.

Chapter 2

Development of a Multi-Modal Spectroscopy Tool for Studies of In Vivo Mitochondrial Energetics in Mouse Skeletal Muscle*

Abstract

Despite the relevance of studying mitochondrial function in health and disease, methods for measuring in vivo mitochondrial metabolism are lacking. To overcome the difficulty of characterizing in vivo physiology using ex vivo assays, non-invasive approaches using ^{31}P magnetic resonance (MR) spectroscopy to assess phosphometabolite concentrations and near-infrared (NIR) optical spectroscopy to assess tissue oxygenation in skeletal muscle have been developed. These advances vastly expanded the ability of scientists to observe in vivo mitochondrial physiology, but still presented a number of limitations. Importantly, these approaches use separate experiment sessions to acquire MR and optical spectra, preventing measurement of short-term physiological changes and increasing physical stress on both human and animal subjects. To address this limitation and permit studies of changes in the oxidative environment that occur on a shorter timescale, we present the development of a multi-modal MR and optical spectroscopy system for studies of in vivo mitochondrial energetics in mouse skeletal muscle. We validate this new system through a series of in vivo studies on adult wild-type mice.

This chapter presents the development of multi-modal spectroscopy for a 7T magnet at the University of Washington Medical Center. This system was later used as a model for development of a similar system for use with a 14T magnet at the University of Washington South Lake Union Campus. A provisional patent application (UW ROI #1184) has been filed covering this technology.

Introduction

Mitochondria are often referred to as the "cellular powerhouses," responsible for synthesizing the majority of ATP from carbon-based energy sources like sugar, fat, and protein during aerobic metabolism (151). In addition to this crucial role in cellular energetics, mitochondria are key integrators of intracellular signaling (23), involved in the maintenance of calcium homeostasis (24), and a central player in programmed cell death (168). As a consequence of these important roles, mitochondria have been implicated in numerous debilitating conditions including neurodegenerative disease (26), insulin resistance (145), obesity (67), and muscle wasting (107). Despite the significance that an understanding of mitochondrial function has from diagnostic, therapeutic, and basic research perspectives, methods for measuring in vivo mitochondrial function are lacking (21).

The gold-standard for measuring mitochondrial function is a decades-old technique, which uses an oxygen-sensitive electrode to monitor oxygen flux in a chamber containing isolated mitochondria, cells, or live tissue biopsies (75). By measuring mitochondrial respiration under different substrate concentrations, and/or in the presence of specific electron transport chain (ETC) complex inhibitors, valuable insight into the intrinsic functional properties of mitochondria can be gained. Complementing this method, ex vivo approaches exist to measure mitochondrial qualities such as inner mitochondrial membrane potential (Δψ, (82, 150)), calcium handling (60), and reactive oxygen species (ROS)

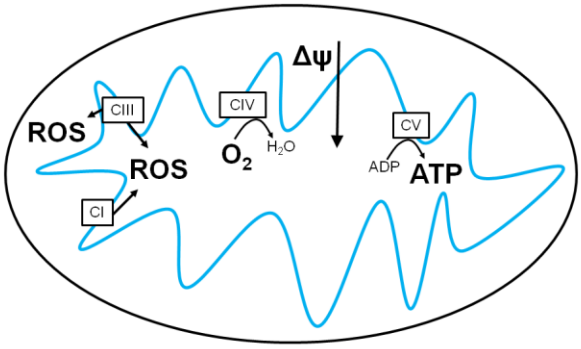

Figure 2.1. Mitochondrial metabolism consumes oxygen to establish a membrane potential (Δψ) which is used to drive synthesis of ATP. This process produces ROS at Complexes I and III as an inevitable byproduct.

production (63, 185). In addition, classic histological methods can provides insight into mitochondrial distribution, shape, and size (18), and biochemistry can shed light on protein composition, oxidative damage, and expression of mitochondrial and nuclear genes related to regulation of mitochondrial biogenesis and behavior (7, 96, 131).

While these approaches provide novel insights into ex vivo mitochondrial form and function, they are unable to observe mitochondria in their native environment inside the body of a living organism. Complicating this even further, questions have arisen concerning the sensitivity of mitochondria and surrounding tissue to sample preparation for ex vivo assays, particularly in the case of skeletal muscle (129, 132). As a result, many ex vivo assays are good at comparing test groups to controls under defined experimental conditions, but these conditions cannot be expected to represent the conditions that mitochondria experience in vivo.

To overcome this limitation, progress has been made in the development of non-invasive spectroscopy techniques capable of measuring in vivo mitochondrial function. In particular, magnetic resonance (MR) spectroscopy has been applied to measure phosphometabolite concentrations and ATP flux (16, 34, 93) and near infrared (NIR) optical spectroscopy has been applied to measure oxygen flux (11, 103, 153) in live muscle. Since the net results of mitochondrial metabolism are the reduction of oxygen to water and the synthesis of ATP from ADP and inorganic phosphate (P_i), the combination of these noninvasive approaches provides a good view of mitochondrial function. Experiments require perturbation of the in vivo system (which in the case of skeletal muscle includes ischemia and/or contraction), and have already demonstrated value in characterizing the in vivo physiology of aging in humans (4) and mice (106).

Published reports before 2012 involve separate experiment sessions to acquire MR and optical spectroscopy data (hereafter referred to as single-mode spectroscopy). In the case of human studies this involves prolonged discomfort during two experiments, and for mouse studies the consequences of multiple experiments are magnified as animals must be repeatedly anesthetized to acquire data. Furthermore, separate experiment sessions limit researchers to studies of physiological conditions that are unlikely to change significantly for multiple hours or days. This places a burden on the need for reliable controls and prohibits studies of rapidly changing physiological processes that are typical of pro- or anti-oxidant effects on the intracellular environment (40, 194). To permit studies of in vivo oxidative stress on a shorter timescale, we present a multi-modal MR and optical spectroscopy system for studies of in vivo mitochondrial metabolism in mouse skeletal muscle. This system is capable of acquiring the entire suite of physiological measurements provided by MR and optical spectroscopy during a single rest-ischemia-recovery experiment lasting less than one hour.

Theory

In vivo analysis of mitochondrial metabolism using MR and optical spectroscopy relies on the distinct spectral profiles of surrogate markers of ATP and oxygen flux, and the spectral changes that take place in these markers during periods of rest, ischemia, and recovery. Because the net results of mitochondrial metabolism are the reduction of oxygen at complex IV and the synthesis of ATP at complex V, an overall picture of mitochondrial health can be gained by measuring these two events. In the case of skeletal muscle, the surrogate markers are phosphocreatine (PCr) that exists in equilibrium with ATP, and the oxygen saturations of hemoglobin (Hb) and myoglobin (Mb), which deliver oxygen from blood to mitochondria. Skeletal muscle is uniquely suited for measuring these surrogates non-invasively due to its large superficial volume, high concentration of phosphometabolites, and the ease with which it can be perturbed without endangering organism health (111). Furthermore, skeletal muscle has high metabolic demand making it a relevant tissue for studies of mitochondrial health (198). Methods have been established to assess metabolite concentrations (at rest), mitochondrial oxygen consumption and resting cellular ATP demand (during ischemia), and mitochondrial phosphorylation capacity (during recovery from ischemia) using single-mode spectroscopy. The theory that underlies these approaches is presented elsewhere (16, 34, 105) and reviewed briefly below.

MR Analysis of Mitochondrial ATP Production

In vivo ^{31}P MR spectroscopy during rest, ischemia, and recovery can be used to measure mitochondrial ATP production in skeletal muscle (16). Due to the unique energy demands of skeletal muscle, PCr exists at high concentration within skeletal muscle cells and buffers ATP concentration through activity of the creatine kinase (CK) reaction:

$$PCr + ADP^{-} + H^{+} \xleftrightarrow{CK} Cr + ATP \qquad (1)$$

Where *Cr* represents phosphate-free creatine. This energy buffer maintains constant ATP concentrations despite fluctuations in ATP supply (e.g. oxidative phosphorylation) and demand (e.g. muscle contraction). Maintaining constant ATP concentration is critical for maintaining a healthy cellular energy state, because the energy that fuels cellular activity is derived from ATP hydrolysis. ATP hydrolysis yields a significant amount of energy due to the large concentration discrepancy between ATP and its hydrolytic byproduct

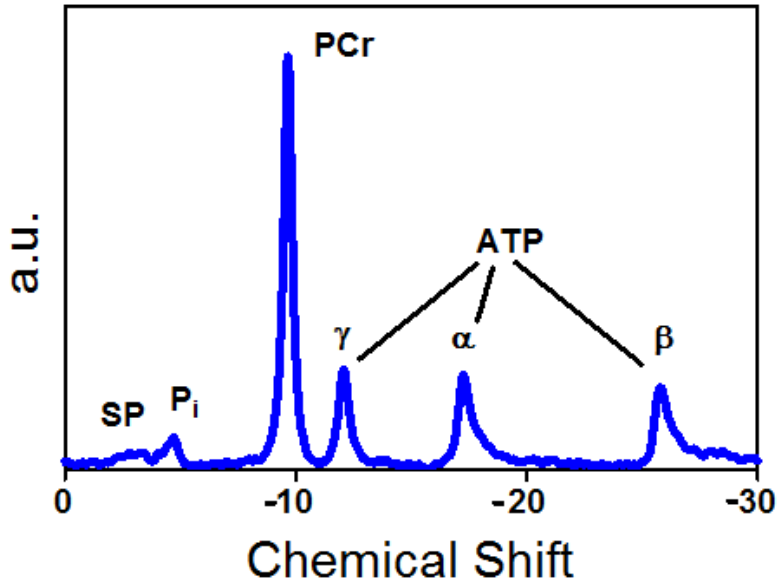

Figure 2.2. Peak areas from MR spectra are proportional to metabolite concentrations, illustrating the discrepancy between PCr, ATP, and ADP concentrations in skeletal muscle. PCr peak area is approximately 4 times greater than each phosphate peak of ATP (γ, α, and β) and the phosphate peaks of ADP in solution are below signal-to-noise limitations beneath the γ and α phosphate peaks of ATP. SP represents sugar phosphate intermediates of glycolysis and P_i is inorganic phosphate.

ADP (122). In young, resting mouse skeletal muscle, typical concentrations measured in our lab (see Tables 3.2, 4.1, and 5.1) for PCr are roughly 40mM, while ATP is maintained near 10mM and ADP near 10μM. These concentration discrepancies are evident in a typical ^{31}P MR spectrum acquired from the muscles of the mouse distal hindlimb (Fig. 2.2). As illustrated, the PCr peak is large relative to other peaks and well above signal-to-noise limitations of typical MR systems (111). As a result, changes in

PCr peak magnitudes can be measured accurately in live skeletal muscle using MR spectroscopy, and changes in peak magnitude can be converted into absolute concentrations using post-mortem analysis of phosphometabolite concentrations (discussed in Methods). Measurements of PCr flux can then be translated into measures of mitochondrial ATP production as discussed in the next paragraph.

The activity of the CK reaction (Equation 1) is coupled to ATP hydrolysis in skeletal muscle by a net process referred to as the Lohmann reaction (91):

$$PCr + ADP + \beta H^+ \xleftrightarrow{CK} Cr + ATP \qquad (2)$$

$$ATP \xleftrightarrow{ATPase} ADP + P_i + \alpha H^+$$

Where *ATPase* represents the net activity of all enzymes that catalyze the hydrolysis of ATP, and α and β are coefficients reflecting the variable proton stoichiometry of this reaction. In the case of skeletal muscle, *ATPase* includes (but is not limited to) myosin ATPase on contractile myofilaments and ion pumping ATPases bound to membranes, and can be considered constant under resting condition. Furthermore, under resting conditions, the relationship between $\Delta\psi$ and the ATP/ADP ratio links the rate of mitochondrial ATP production to the rate of ATP hydrolysis (121). Eliminating oxidative phosphorylation by ischemia effectively translates the rate of oxidative ATP production by mitochondria into a steady decline of PCr, which can be measured using MR spectroscopy (91). During return of blood flow after ischemia, PCr follows a monoexponential recovery defined by a time-constant, τ, that is directly related to the maximal rate of oxidative ATP production (ATPmax), due to reversal of Equation 1 under conditions of unlimited oxidative phosphorylation (34, 110, 123):

$$ATP\max = \frac{1}{\tau} \times \Delta[PCr] \qquad (3)$$

Optical Analysis of Mitochondrial Oxygen Consumption

Inspired oxygen is delivered to skeletal muscle by Hb in the blood and shuttled to mitochondria by Mb packed within skeletal muscle cells (191). Hb and Mb bind oxygen reversibly and have distinct absorption spectra in the NIR region of the electromagnetic spectrum (Fig. 2.3). Due to unique changes that occur in these spectra as a result of oxygen-dissociation, NIR spectroscopy can be used to quantify the oxygen saturations of Hb and Mb (Hb_{sat} and Mb_{sat}, respectively). Mitochondrial oxygen consumption can be determined as follows:

Under resting conditions with adequate blood flow, oxygen supply exceeds mitochondrial demand (190). During ischemia, however, mitochondria are left to respire with a finite amount of total oxygen bound to Hb and Mb or dissolved in the vascular or intracellular compartments. Total oxygen in this closed system can therefore be described as (103):

$$TO_2 = Hb_{sat} \times [Hb] + P_{O_2Vasc} \times O_{2sol} + Mb_{sat} \times [Mb] + P_{O_2Cell} \times O_{2sol} \quad (4)$$

Where TO_2 represents total oxygen, P_{O2Vasc} and P_{O2Cell} represent the partial pressures of oxygen in the vascular and intracellular compartments respectively, and O_{2sol} represents the solubility of oxygen in water. Making assumptions for O_{2sol} based on published empirical data (98) and using post-mortem biochemical analysis to quantify *[Hb]* and *[Mb]*, the remaining variables can be determined from Hb_{sat} and Mb_{sat} based on the known binding kinetics of Hb and Mb with oxygen:

$$P_{O_2Vasc} = \left[\frac{Hb_{sat} \times P_{50}^{n}}{(1 - Hb_{sat})} \right]^{\frac{1}{n}} \quad (5)$$

$$P_{O_2Cell} = \frac{Mb_{sat} \times P_{50}}{1 - Mb_{sat}} \quad (6)$$

Where P_{50} for Hb and Mb, as well as the Hill coefficient for Hb-oxygen binding (n), can be assumed from published values (8, 103, 156). As the primary oxygen sink in skeletal muscle cells, mitochondrial oxygen consumption can then be measured by quantifying the rate at which total oxygen decreases during ischemia.

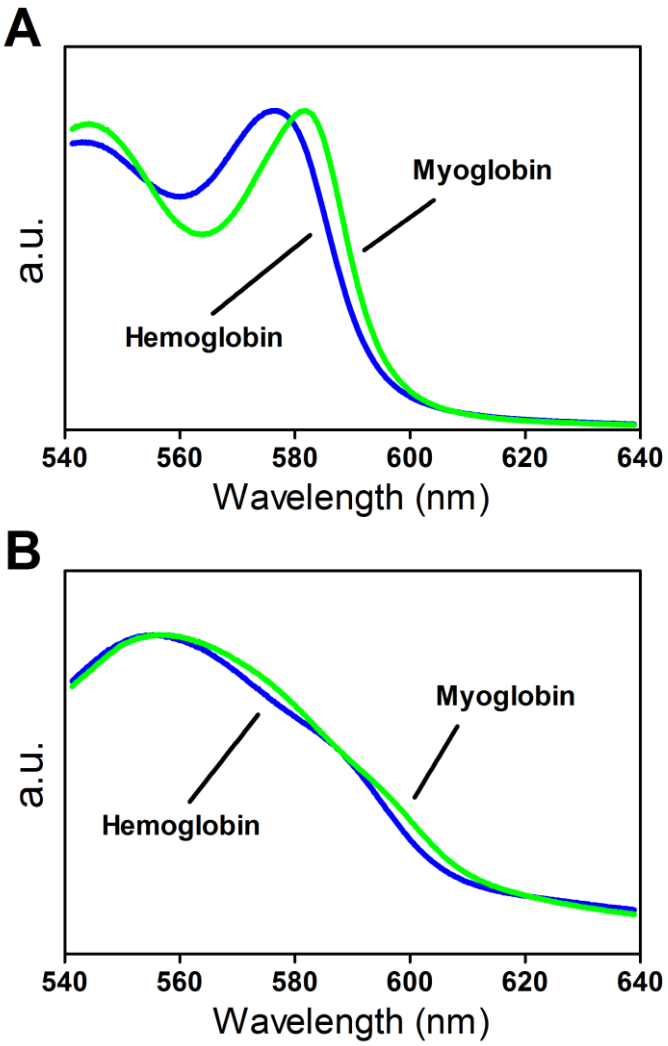

Figure 2.3. Hb and Mb have similar yet distinct absorption spectra in the NIR region of the electromagnetic spectrum under (A) oxygenated and (B) deoxygenated conditions. Spectra are from Hb or Mb in solution with 1% intralipid, converted to OD using a 1% intralipid reference, and normalized to respective maxima for the ease of comparison.

Methods

Animals

Validation studies were approved by the Institutional Animal Care and Use Committee of the University of Washington. Female C57BL/6J mice from Jackson Laboratory (Bar Harbor, ME) were used between 8 and 12 months of age. All mice were kept on a 12 hour light/dark cycle with free access to water and standard mouse chow until immediately prior to experimentation. Mouse body temperatures were maintained by forced air at 36°C ± 1°C throughout in vivo experiments. Mice were allowed to fully recover following in vivo experiments and were returned to long-term housing. Paraquat (Item 36541, Sigma) was dissolved in saline and administered via intraperitoneal injections.

Hardware

We modified a custom-built MR-probe for use in a vertical bore 7T magnet (Oxford Instruments, Oxford, UK) for simultaneous acquisition of MR and optical spectra in the mouse distal hindlimb. The original probe was based on a system presented previously (106), and developed by the Electronics/RF Coil Lab at the University of Washington with the intent of conducting single-mode MR spectroscopy at both ^{1}H (300.5 MHz) and ^{31}P (121.7 MHz) frequencies using a manual switching mechanism to change between the two nuclei. It consists of a horizontal, three-turn solenoid, transmit-receive RF coil with a 7mm inner diameter, above which a mouse can be suspended by flexible straps

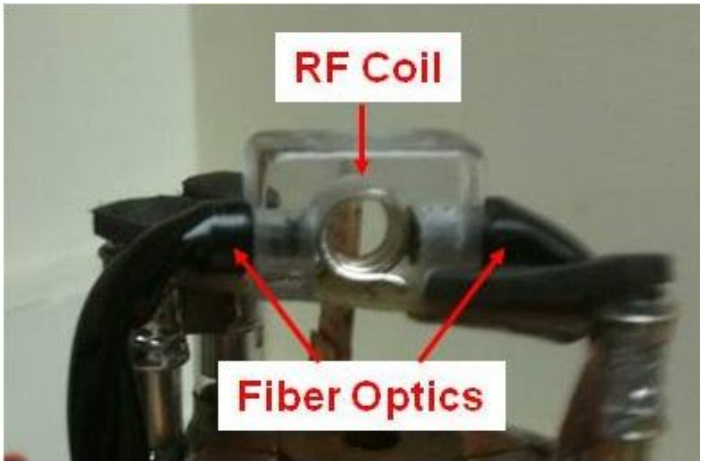

Figure 2.4. Photograph of combined MR-optics probe.

with its distal hindlimb fixed in place through the center of the coil. To acquire optical spectra from the same tissue volume being analyzed as MR, we positioned parallel optical fiber bundles on either side of the coil (i.e. perpendicular to the coil axis) so that light could be delivered to and collected from the sample within the coil. To meet the geometrical design constraints of the MR probe and the high magnetic field associated with MR spectroscopy, we used custom-built 10m long borosilicate fiber bundles with a 5mm diameter, 0.55 numerical aperture, and unreinforced polyvinyl chloride (PVC) sheathing (Fiber Optic Systems Inc., Simi Valley, CA). This design consists of entirely non-magnetic components, transmits NIR light with acceptable losses over the 10m length, is flexible enough to bend into position inside the MR probe, and was extremely inexpensive to build. Fiber bundles were press-fit into parallel holes in a polycarbonate block positioned around the RF coil to ensure good alignment and to preserve an MR-invisible volume in the immediate vicinity of the coil. A photograph of this arrangement is provided in Fig. 2.4.

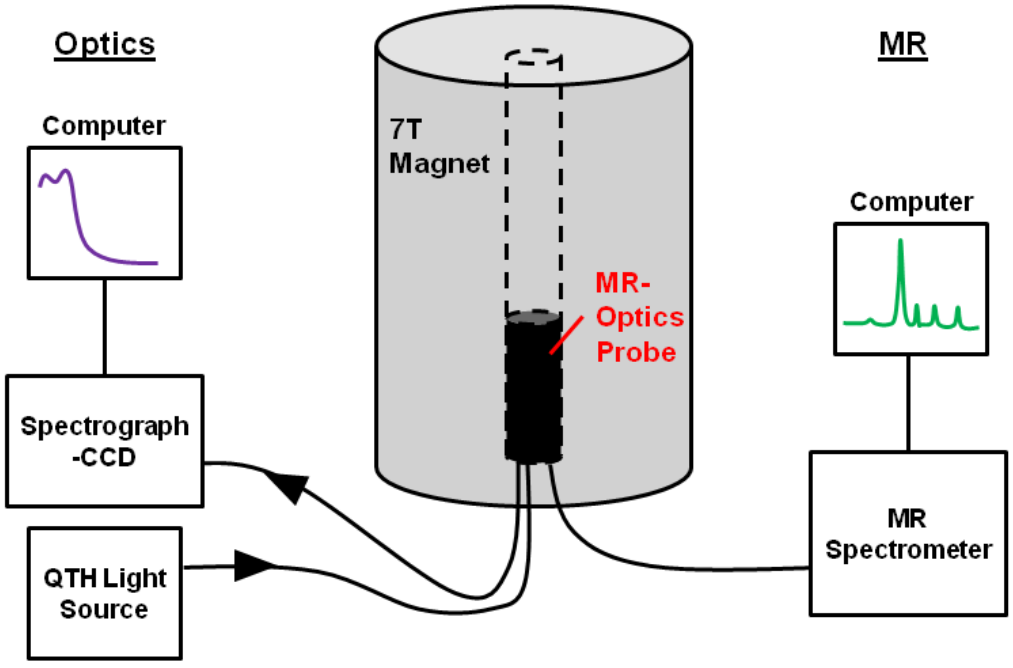

Figure 2.5. Schematic diagram of combined MR-optics hardware.

The distal end of one fiber optic bundle (delivery bundle) was coupled to a broadband Quartz-Tungsten Halogen (QTH) light source (#66052, Newport Corporation, Irvine, CA) and the other (collection bundle) was coupled to the entrance of a spectrograph (SP 2358, Princeton Instruments, Trenton, NJ) with a mounted 1340x400 pixel CCD camera (Pixis:400BR, Princeton Instruments) and a mechanically adjustable entrance slit set at 20μm. A 300 groove/mm diffraction grating blazed at 750nm was used to translate electromagnetic energy from intensity vs. wavelength into intensity vs. transverse position, thus spacing spectral information across CCD pixels. A schematic of the MR and optics hardware arrangement is presented in Fig. 2.5.

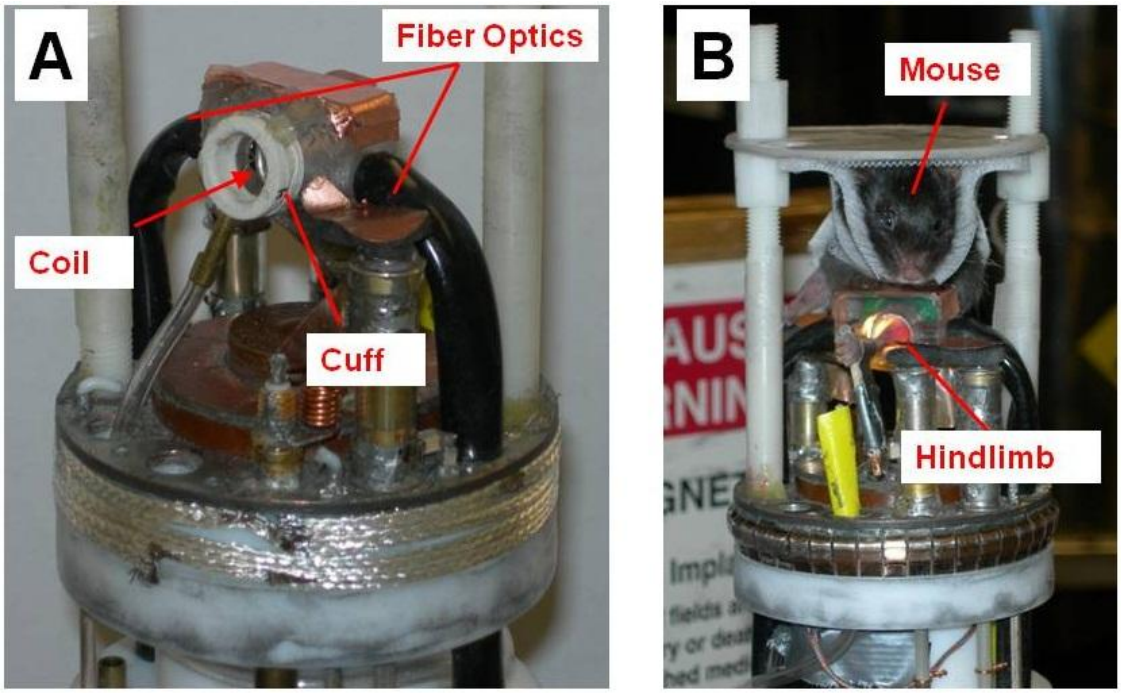

Figure 2.6. Photos of (A) combined MR-Optics system with ischemia cuff in place and (B) mouse in place, facing forward.

In Vivo Protocol

To acquire in vivo MR and optical spectra using the hardware described above, mice were positioned within the MR-optics probe as depicted in the photograph in Fig. 2.6B. A custom-built ischemia cuff was aligned parallel to the RF coil axis and fixed in place on the surface of the polycarbonate fiber optics-holder using hot glue (Fig. 2.6A). Ischemia cuffs were modeled on the inflatable cuff design used by Marcinek, et al. (106), and consisted of an approximately 5mm length of 12.7mm diameter PVC tubing enclosed in latex cut from a party balloon. A brass input valve delivered air to the latex-enclosed area from a sphygmomanometer located outside the magnet via approximately 30ft of vinyl tubing. By positioning the mouse hindlimb with the proximal portion of the hindlimb through the ischemia cuff and the distal portion of the hindlimb centered in the RF coil flanked by fiber optics, blood flow to skeletal muscle being measured by spectroscopy could be restricted by operators from outside the magnet.

After anesthetizing mice with 0.01ml/g of 2.5% tribromoethanol (Avertin, Sigma, St. Louis, MO), the distal hindlimb was shaved to clear mouse fur from the optical path. Mice were then suspended from flexible straps above the RF coil and the left hindlimb passed through the ischemia cuff and coil, and fixed with tape to a plastic post at the ankle joint. The tail and contralateral leg were fixed against Delrin posts, away from electrical components of the probe to minimize stray inductance, which was a common problem due to long exposed leads between the RF coil and accompanying resonant circuit capacitors. To minimize interference of light from the reflective inner surface of the probe shield, the volume surrounding the coil hardware and mouse were loosely enclosed by a piece of flexible black plastic. The mouse-containing probe was then inserted into the magnet bore with the coil positioned at the magnet's isocenter for the start of in vivo data acquisition. In vivo experiments consisted of a period of signal optimization which included shimming the ^{1}H peak of tissue water and calibrating the 90° time for ^{31}P

followed by rest-ischemia-recovery during which relevant in vivo MR and optical spectroscopy data were acquired. The steps involved in this process are described in Table 2.1.

Table 2.1. Summary of events during multi-modal in vivo spectroscopy.

Approx. Time (min)	**Event**	**Description**
1-10	Shimming	Probe is tuned and matched to ^{1}H signal and then the ^{1}H peak of tissue water is shimmed to optimize field homogeneity. Probe is then switched to ^{31}P resonance and tuned and matched at this frequency.
10-15	Calibrate Pulse Width	Pulse-width is varied while allowing full relaxation to maximize the signal-to-noise ratio of PCr (i.e. the 90° flip time for PCr is determined).
15-30	Fully Relaxed	High signal-to-noise ^{31}P spectrum is acquired under fully-relaxed conditions.
30-52	Dynamic	Continuous ^{31}P MR and NIR optical spectra are acquired during rest-ischemia-recovery. Typical dynamic experiment timing is summarized below. Time(min) — Event 0 — Start MR/Optics data acquisition 1 — Turn on flow of 100% O_2 2 — Induce ischemia ($P_{cuff} \geq 300$mmHg) 13 — Release ischemia 22 — Stop MR/Optics data acquisition

MR Data Acquisition and Analysis

MR spectra were acquired using VNMR software (Varian, Palo Alto, CA). Hard-pulse sequences at a power of 42dB were used to acquire all ^{31}P free-induction decays (FIDs) with a sweep width of 10kHz and 4096 complex points. Frequency spectra were generated in VNMR by exponentially multiplying (20Hz), Fourier transforming, and manually phase correcting raw FIDs. During rest, high signal-to-noise fully-relaxed ^{31}P spectra were acquired from 32 consecutive spectra with a 90° flip angle (typical pulse-width of 40-50μsec) and 25sec interpulse delay. During dynamic experiments, 200 consecutive spectra consisting of 4 consecutive transients were acquired with a 45° flip angle and 1.5sec interpulse delay for a time resolution of 6sec.

Processed MR spectra from VNMR were taken to custom-written software in MATLAB (Mathworks, Natick, MA) for analysis. From fully-relaxed spectra, relative peak areas for P_i, PCr, and the three peaks of ATP were calculated by numerical integration. To account for spectral drift, which was common in this system, this analysis was later updated to align fully-relaxed spectra according to PCr peak location prior to summing and numerical integration. For dynamic data, spectra were aligned according to PCr peak location, groups of three consecutive spectra were summed to improve signal-to-noise, and then relative changes in P_i and PCr peak magnitudes were calculated using the Fit-to-Standard algorithm (70). This algorithm uses the natural lineshape of an experimental peak (in this case the average of all spectra acquired during ischemia) as a reference against which the magnitude of other experimental peaks can be calculated. Briefly, the slope of the least-squares linear approximation between the amplitudes at each point of an experiment peak and the corresponding amplitudes from a reference peak is used to represent relative peak magnitude. To account for variable relaxation, the peak amplitudes for P_i and PCr during the resting period of dynamic acquisition were assumed to represent the P_i/ATP and PCr/ATP ratios measured from fully relax spectra. The γATP peak was then used as an internal reference (assuming an

ATP concentration of 9mM for validation experiments) to find P_i and PCr concentrations over time. According to the relationship described in Theory (Equation 2), the resting ATPase rate can be calculated simply as:

$$ATPase = \frac{\Delta PCr}{\Delta t} \quad (7)$$

using a least-squares linear approximation of PCr breakdown before the activation of glycolytic ATP synthesis, which causes reversal of the Lohmann reaction (Equation 2) (104).

Optics Data Acquisition and Analysis

Optical spectra were acquired using WinSpec software (Princeton Instruments) at a time resolution of 1sec (later updated to 0.5sec) by opening a mechanical shutter at the entrance to the spectrograph for a defined period of time while samples were continuously irradiated. This acquisition time was determined prior to the start of experiments by optimizing signal intensity without saturating any pixels of the CCD array, and typically fell between 20 and 50msec. Lamp power was set at 50W, center spectral wavelength at 680nm, and software binning was off.

Due to the large numerical aperture of the fiber bundles used on our 7T system, a high signal-to-noise (i.e. average of 50 consecutive acquisitions) spectrum was acquired prior to each experiment with the RF coil filled with a black cylinder, which was then subtracted from all subsequent spectra. This background correction minimized the influence of light reflected from the coil and other surfaces in the coil volume on data acquired from the mouse hindlimb. Also prior to experiments, a high signal-to-noise (average of 50 consecutive acquisitions), background-corrected spectrum from a 1% intralipid phantom positioned within the RF coil was acquired as a reference. One-percent intralipid was used to attenuate light

similarly to the scattering background of skeletal muscle (50). Both background and intralipid spectra were acquired with an acquisition time of 13msec. All in vivo intensity spectra were converted to optical density (OD) spectra in real-time by WinSpec using the following equation:

$$OD(\lambda) = -\log_{10}\left(\frac{I(\lambda)}{I_0(\lambda)}\right) \quad (8)$$

Where I is transmitted intensity, I_0 is the intensity from the 1% intralipid phantom reference, and λ is spectral wavelength.

Absorption spectra collected from the mouse hindlimb over the course of a dynamic rest-ischemia-recovery experiment were taken to custom-written software in MATLAB, converted to 2nd derivatives to minimize the influence of tissue scattering (12), and analyzed using a partial-least-squares (PLS) routine to determine relative oxygen saturations of Hb and Mb. PLS is a multivariate statistical method often employed in non-biological systems to measure chemical components in solution (59). This approach has previously been adapted for use with in vivo optical spectroscopy in muscle to separate the spectral contributions of Mb and Hb (12, 153). It has an advantage over other NIR spectroscopy approaches in that relative saturations of Hb and Mb can be determined independently, thus allowing quantification of TO_2 during ischemia according to Equation 4. Briefly, the PLS analysis routine weights in vivo spectra according to the wavelengths exhibiting greatest sensitivity to changes in oxygenation state of either Hb or Mb. It then performs a principal component analysis on weighted spectra and determines a dimension into which spectra can be translated to reflect changes in either Hb_{sat} or Mb_{sat}, independently. The result is a single value for each spectrum that represents a relative measure of Hb_{sat} or Mb_{sat}. To weight wavelengths according to either Hb_{sat} or Mb_{sat}, spectra are collected from phantoms of known protein concentrations and saturations (referred to as "calibration spectra" or a "calibration set") in advance. More detailed explanations of PLS can be found elsewhere (9, 59). After normalizing the relative oxygen

saturations yielded by PLS under conditions when oxygen saturation can be reasonably assumed (0% at the end of ischemia, and 100% during oxygen delivery at rest for Hb_{sat} and during recovery for Mb_{sat}; Fig. 2.8C and D), results can be used with Equation 4 to calculate mitochondrial oxygen consumption, according to:

$$O_2cons = \frac{\Delta TO2}{\Delta t} \quad (9)$$

For the purposes of the validation experiments presented here, skeletal muscle concentrations for Hb and Mb were assumed to be 0.04μmole/g and 0.03μmole/g, respectively.

Optical Calibration Spectra

A set of optical calibration spectra was generated for use with the PLS analysis of tissue chromophores as described previously (12, 103, 155). Phantoms were created using known concentrations of intralipid plus fully oxygenated or deoxygenated Hb, Mb, or (fully oxidized or reduced) cytochrome c while other chromophores were assume to exist in low enough concentration to be ignored (41). To account for differences in the light scattering properties of tissue, phantoms contained intralipid concentrations of 0.5%, 1%, and 2%. To account for variations in Hb concentration during rest, ischemia, and reactive hyperemia following cuff release, Hb concentrations were varied between 30μM and 90μM while 25μM Mb and 10μM cytochrome c were used in all cases. Hb was acquired from heparinized mouse blood combined at a 1:1 ratio with deionized water to lyse red blood cells, while Mb (M0630, Sigma) and cytochrome c (C7010, Sigma) were reconstituted in deionized water from lyophilized powder. Chromophore concentrations were verified by spetrophotometric analysis (UV1, Thermo Scientific, Waltham, MA). To minimize the spectral contribution of the non-oxygen binding, oxidized species metmyoglobin and methemoglobin, which are maintained at low concentration in vivo (178, 191), Hb and Mb solutions were fully reduced with an excess of sodium dithionite. They were then separated from this

reducing agent by running through a 20cm tall G-25 Sephadex (#G25150, Sigma) column with a 2.5cm diameter, maintained at 4°C in phosphate buffer with a pH of 7.4. Upon exiting the column, fully reduced Hb and Mb were briefly equilibrated with room air to achieve 100% oxygen saturation.

After acquiring reference background and 1% IL spectra, high signal to noise (average of 50 spectra) oxygenated and oxidized absorption spectra were acquired independently for each chromophore with varying intralipid concentrations. Sodium dithionite was then added to phantoms to fully deoxygenate or reduce proteins, and another batch of spectra was acquired. The resulting calibration set data were taken to MATLAB and compiled in a structure to be called upon during PLS analysis. During PLS, random groups of calibration spectra were linearly combined to build composite spectra of known concentration and saturation or oxidation state. The efficacy of calibration spectra was verified by running PLS on a concurrently generated set of composite spectra, and by using Mahalanobis distance analysis to confirm adequate similarity between calibration and test spectra, as described previously (12).

Results

Multi-Modal MR Spectroscopy

We first compared multi-modal MR spectroscopy and the results from Fit-to-Standard analysis over the course of in vivo rest-ischemia-recovery experiments with typical data from single-mode spectroscopy (from control mice presented in Chapter 3). As demonstrated in Fig. 2.7A and B, spectra from the two systems had similar features, with the most noticeable difference being a loss of signal-to-noise ratio (SNR) in multi-modal MR spectra (18.1±0.5dB vs. 27.1±0.1dB, averaged over the resting period of dynamic experiments). Summing 3 consecutive spectra improved SNR to 24.9±0.6dB for the multi-modal system and a least-squares linear approximation of ATPase could be made with similar accuracy in both systems (Fig. 2.7C and D).

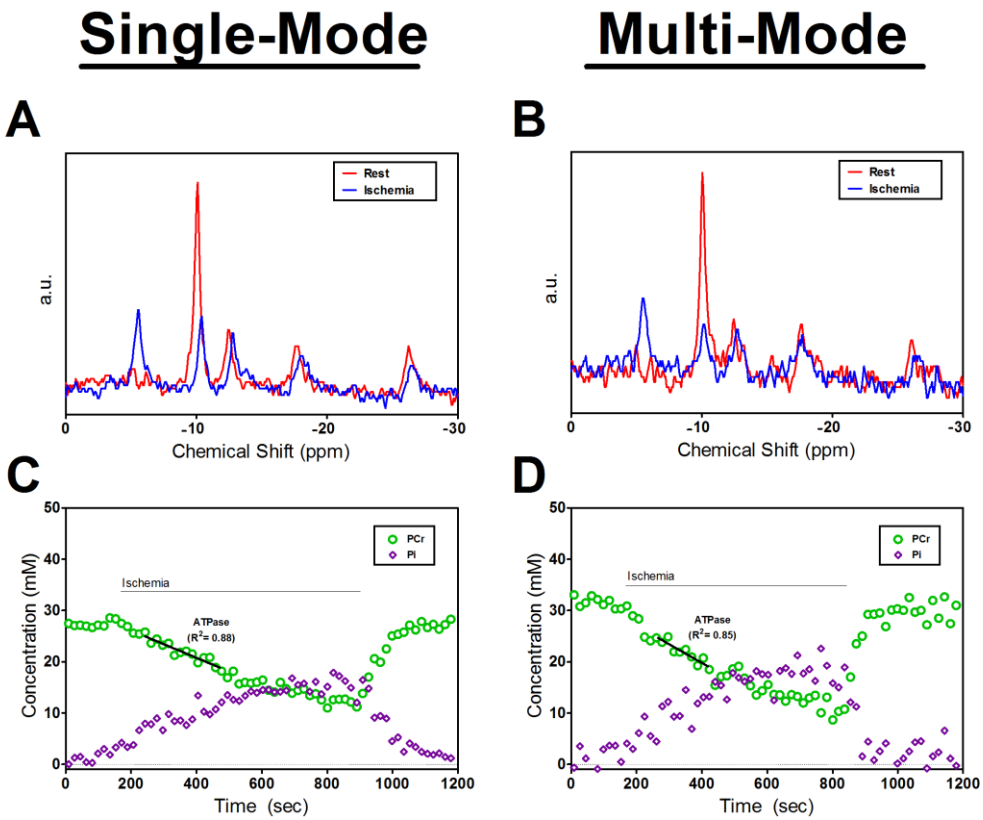

Figure 2.7. Multi-modal in vivo spectroscopy yielded MR spectra (A and B) and resulting peak analysis (C and D) similar to those typical of single-mode spectroscopy.

Multi-Modal Optical Spectroscopy

Next we compared multi-modal optical spectra and the results of PLS analysis over the course of in vivo rest-ischemia-recovery experiments with typical data generated using single-mode spectroscopy. As demonstrated in Fig. 2.8, results are similar using both approaches and, in fact, appear cleaner in the multi-modal system. Both analyses demonstrate distinct spectral characteristics during rest and ischemia and clear separation in the time-dependent changes in Hb_{sat} and Mb_{sat}. The recovery of Hb_{sat} beyond 100% oxygen saturation during recovery from ischemia is a result of an increase in the concentration of total Hb as a result of reactive hyperemia and can be disregarded.

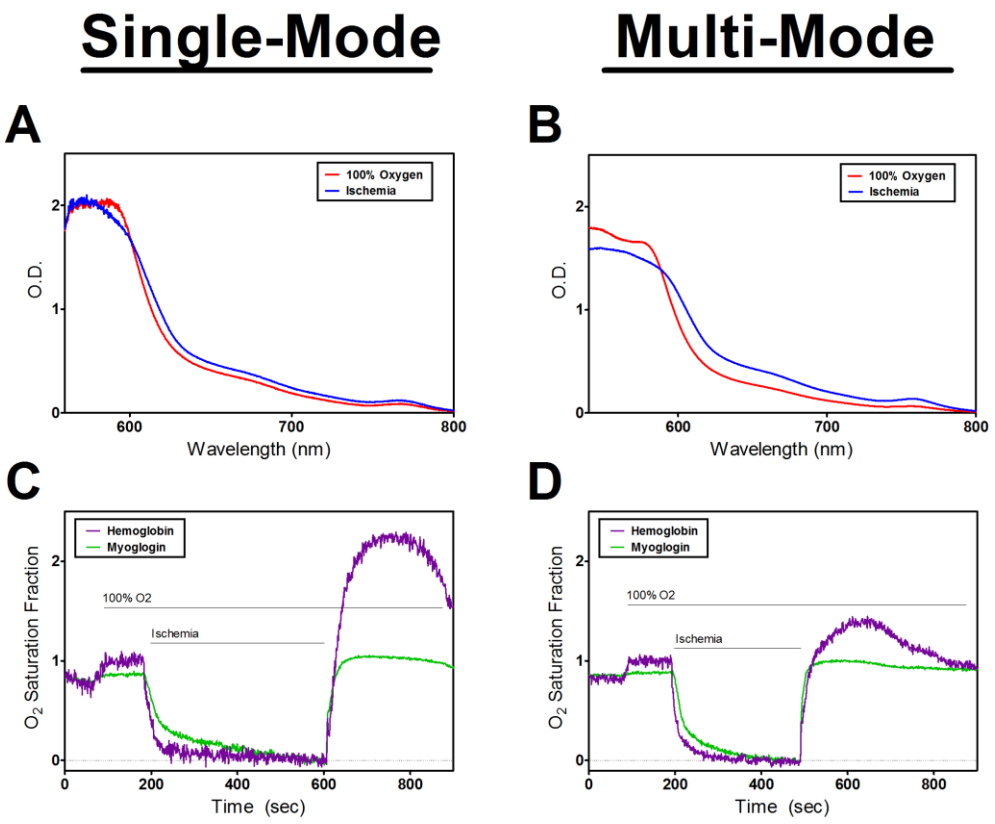

Figure 2.8. Multi-modal in vivo spectroscopy yielded optical spectra (A and B) and separation of Hb_{sat} and Mb_{sat} from PLS analysis (C and D) similar to those typical of single-mode spectroscopy.

In Vivo Analysis Validation

Results from in vivo validation experiments were in excellent agreement with published values (Fig. 2.9) (105, 106). ATPase rate (28.30±1.21nmole/g/sec vs. 26.13±1.22nmole/g/sec), O_2 consumption rate (6.16±0.24nmole/g/sec vs. 6.27±0.46nmole/g/sec), and the resulting P/O ratio (2.35±0.05 vs. 2.16±0.24) calculated as ½ (ATPase rate divided by O_2 consumption rate) for multi- vs. single-mode spectroscopy were all in strong agreement. Multi-modal measurement of the PCr/ATP ratio (the ratio between PCr and γATP peak areas from resting, fully-relaxed spectra) was in startlingly good agreement with published values (3.37±0.03 vs. 3.37±0.11, Fig. 2.9D), as was the monoexponential time-constant of PCr recovery after ischemia (46.8±5.0sec vs. 46.4±3.4sec for wild-type ATPmax data from Chapter 3, data not shown here).

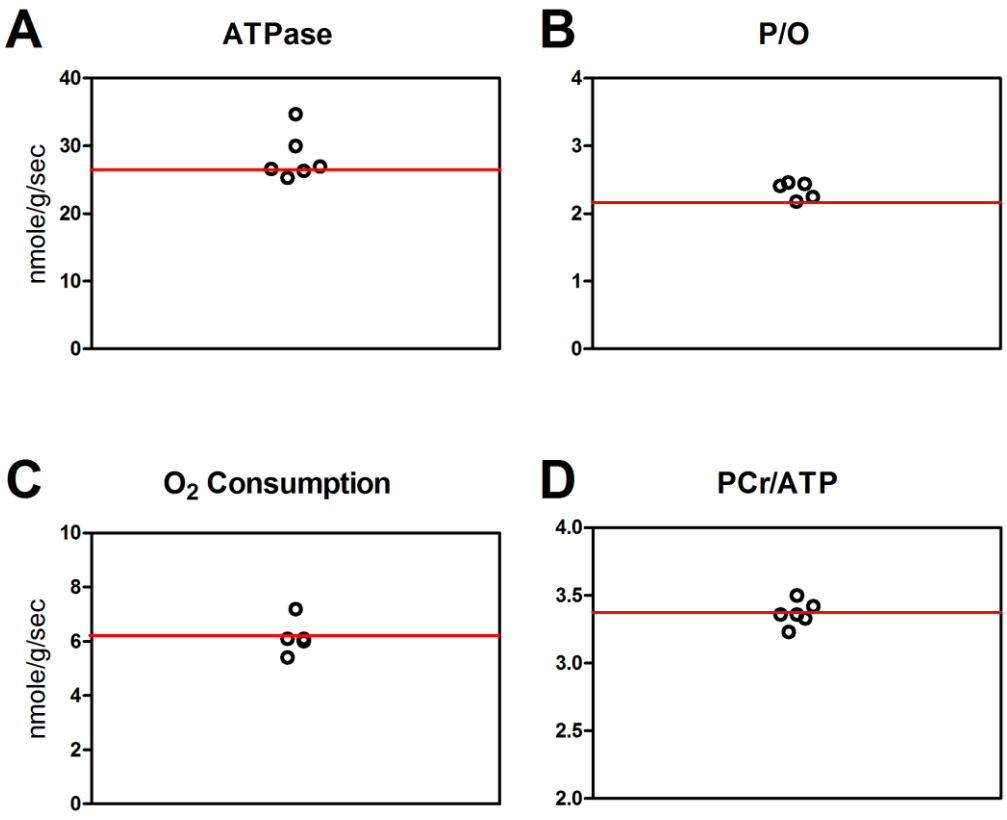

Figure 2.9. (A) ATPase rates, (B) P/O ratios, (C) O2 consumption rates, and (D) PCr/ATP ratios calculated using multi-modal spectroscopy were in excellent agreement with published averages acquired using single-mode spectroscopy. Open circles represent multi-mode validation data while solid red lines represent published averages using single-mode spectroscopy (105, 106).

Longitudinal Effects of Paraquat

To demonstrate the value of multi-modal spectroscopy, the time-course of the in vivo effects of paraquat on mitochondrial efficiency were assessed using a longitudinal study design. We injected a small number of female mice with a single bolus of 20mg/kg paraquat and measured mitochondrial energetics after 1 hour, 1 day, and 3 days. As illustrated in Fig. 2.10, P/O ratio declined significantly over time in both control and PQ-treated groups, while PCr/ATP ratio trended insignificantly downward over time in both groups. The significance of these findings is two-fold. First, the reliability of longitudinal data acquisition using multi-modal spectroscopy is supported by small group standard error, and distinct time-related trends. Second, the time-dependent decrease in P/O ratio of control mice is indicative of physiological perturbations induced by repeated bouts of anesthesia and ischemia. This demonstrates the need for strong controls and careful interpretation of in vivo data acquired using a single-mode approach that spans multiple days. In this case, an effect of paraquat is evident after 1 and 3 days, however this result is intertwined with the effects of repeated experimentation.

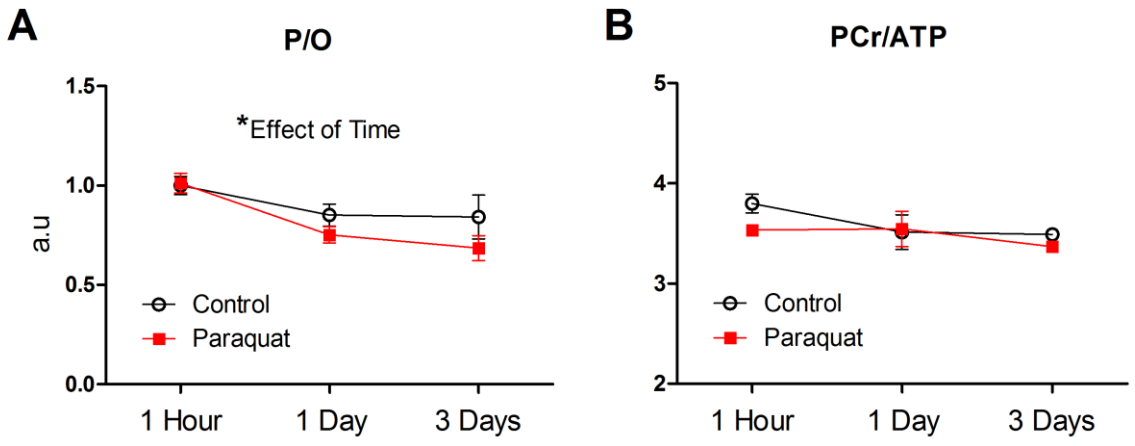

Figure 2.10. Longitudinal progression of PQ treatment. (A) P/O ratio underwent a time-dependent decline in both controls and PQ-treated mice. (B) No significant changes were observed in PCr/ATP. Data means±SEM, n=3, * $p < 0.05$ as measured by two-way ANOVA. All P/O values are presented as the fraction of control average after 1 hour.

Discussion

In this chapter we describe the development of a multi-modal in vivo spectroscopy system capable of acquiring simultaneous MR and optical spectra from the distal mouse hindlimb. This system represents the evolution of previous single-mode in vivo MR and optical spectroscopy systems that used separate experiment sessions to collect data from different modalities. We confirmed the reliability of data acquisition and analysis using this new technology and validated the physiological accuracy of in vivo mitochondrial energetics in live mice.

While this technology represents a significant advance in the ability to study in vivo mitochondrial function, it is not the first attempt at using spectroscopy to measure energetics and oxygenation simultaneously (89, 94). For example, Lanza et al. used an interleaved ^{1}H and ^{31}P MR spectroscopy approach for making in vivo measurements of the rate of oxygen desaturation from Mb and hydrolysis of PCr simultaneously during ischemia (94). However, the inability to measure oxygen changes in the vascular compartment precludes the use of this technology for measures of mitochondrial oxygen consumption as we have described here. This is also not the first system to integrate optical and MR spectroscopy or imaging hardware for simultaneous data acquisition. Such approaches have been taken to register tissue oxygenation with brain activity (195), characterize cell damage in perfused hearts (89), and improve molecular imaging of breast cancer (27). To the best of our knowledge, our system does represent the first of its kind to use simultaneous MR and optical spectroscopy to assess in vivo metabolism in mouse skeletal muscle using measures of energetics and oxygenation.

MR and optical spectroscopy have been used to measure in vivo metabolism in both humans and mice using single-mode approaches. Amara et al (4) and Marcinek et al (106), for instance, demonstrated differences in mitochondrial efficiency (i.e. P/O ratio) in old humans and mice, respectively. While the

value of such measurements cannot be understated when compared to ex vivo alternatives to understanding the physiology of aging, they are limited to the study of slowly changing physiological states. For example, when comparing an 80 year old human to a 20 year old human, the matter of a few hours or a few days separating experiment sessions for measuring energetics and oxygenation will have little effect on the conclusions to be drawn between young and old. However, if one were interested in studying the physiological response of a drug with a steadily changing concentration profile and which clears the body in a matter hours, then this approach would not suffice. Drug concentrations would be unavoidably different during separate experiment sessions and conclusions would be influenced by the manifestations of repeat drug exposure. With specific relevance for the work presented here, in vivo studies are limited by single-mode spectroscopy for three main reasons: *(1)* pharmacological intervention is a valuable tool in controlling the oxidative environment, as will be evident in Chapters 3-5, *(2)* levels of oxidative stress change on a short timescale due to short half-lives of ROS (138) and rapid downstream changes that these ROS induce (52, 194), and *(3)* repeated experimental sessions appear to induce energetic changes similar to treatment with the pro-oxidant paraquat (Fig. 2.10).

This approach overcomes these limitations by acquiring the suite of energetic and oxygenation measurements simultaneously, thereby keeping in vivo analysis on a timescale compatible with common physiological fluctuations and avoiding potentially confounding effects of adaptation or repeated experimentation. Furthermore, developing this technology for use in mice opens the door to a long list of available pharmacological and genetic interventions that will allow many relevant questions to be answered. In the future, the translation of a similar method for use in humans would bring value to both diagnosis and treatment.

The following chapters demonstrate the power of this new technology through a study of the effects of aging and acute fluctuations in the intracellular oxidative environment on mitochondrial energetics. After using single-mode spectroscopy to establish the relevance of pursuing such a study in Chapter 3, Chapters 4 and 5 use multi-modal spectroscopy to study the effects of short-term changes in the oxidative environment in young and old mice that would have been impossible using single-mode spectroscopy. The logistical consideration of acquiring accurate data sets simultaneously is not the only value of this approach, and additional benefits will become apparent in Chapter 4.

Chapter 3

Reduced Coupling of Oxidative Phosphorylation In vivo Precedes Electron Transport Chain Defects Due to Mild Oxidative Stress in Mice*

Abstract

Oxidative stress and mitochondrial function are at the core of many degenerative conditions. However, the interaction between oxidative stress and in vivo mitochondrial function is unclear. We used pharmacological (2 week paraquat (PQ) treatment) and transgenic (mice lacking Cu, Zn-superoxide dismutase ($SOD1^{-/-}$) and glutathione deficient ($GCL^{+/-}$)) mouse models to test the effect of oxidative stress on in vivo mitochondrial function in skeletal muscle. Single-mode magnetic resonance and optical spectroscopy were used to measure mitochondrial ATP and oxygen fluxes and cell energetic state. In all models of oxidative stress, coupling of oxidative phosphorylation was significantly lower (lower P/O) at rest in vivo in skeletal muscle and was dose-dependent in the PQ model. Despite this reduction in efficiency, in vivo mitochondrial phosphorylation capacity (ATPmax) was maintained in each model, and ex vivo mitochondrial respiration in permeabilized muscle fibers was unchanged following PQ treatment. In association with reduced P/O, PQ treatment led to a dose-dependent reduction in PCr/ATP ratio and increased phosphorylation of AMPK. These results indicate that oxidative stress uncouples oxidative phosphorylation in vivo and results in energetic stress in the absence of defects in the mitochondrial electron transport chain.

**A significant portion of this chapter is published in almost this exact form in PLoS ONE, November 2011; 6(11): e26963.*

Introduction

Oxidative stress and mitochondrial function are key elements of many pathological conditions, including high fat diet induced insulin resistance, neurodegenerative disease, disuse atrophy, and sarcopenia (5, 26, 29, 77, 117). The role of reactive oxygen species (ROS) in cellular function is most commonly associated with damage to DNA, proteins, and lipids. However, ROS are also involved in the regulation of several cellular processes including mitochondrial biogenesis (57, 140), increased activation of antioxidant defenses (52, 62, 166), exercise adaptation in skeletal muscle (57, 135, 144, 193) and cell death (28, 43). Mitochondrial function and energy homeostasis play a key role in many of these processes. Thus, interaction between mitochondrial function and oxidative stress appears to play an important role in controlling cell health and disease (28, 37, 38, 72). However, the control of in vivo mitochondrial function and cell energetics by oxidative stress remains unclear.

In skeletal muscle, ROS are produced by the mitochondrial electron transport chain as a by-product of oxygen consumption (175) and by cytosolic sources such as NAD(P)H oxidase during contraction(135). ROS or oxidative by-products modulate mitochondrial metabolism *in vitro* beyond the mitochondrial dysfunction that results from oxidative damage. Addition of oxidants or lipid peroxides to isolated mitochondria results in an increased proton leak from the inner membrane space into the matrix thereby partially uncoupling mitochondrial ATP production from oxygen consumption (46, 47). Rather than being caused by damage to mitochondrial proteins or lipids, this reduced coupling is the result of activated proton leak proposed to be mediated by uncoupling protein 3 (UCP3) and adenine nucleotide translocase (ANT) (125). However, activated leak through UCP3 and ANT is enhanced in the presence of fatty acids and is inhibited by physiological concentrations of GDP and other purine nucleotides in vitro (6, 125). Thus, it is not clear to what extent this oxidative stress-activated leak occurs in vivo and, if present, what effect it has on cell energetics.

In this study we use metabolic spectroscopy to test the control of in vivo mitochondrial coupling by oxidative stress. We use magnetic resonance (MR) spectroscopy and optical spectroscopy (105) to determine the coupling of oxidative phosphorylation (P/O), maximal mitochondrial ATP production (ATPmax), and cell energy state in mice treated with the pro-oxidant paraquat (PQ), mice lacking the antioxidant enzyme Cu-Zn-superoxide dismutase ($SOD1^{-/-}$), and mice missing one allele for the rate-limiting enzyme necessary for glutathione synthesis (glutamate-cysteine ligase modifier subunit, $GCL^{+/-}$) leading to a deficiency in the molecular antioxidant glutathione. The mechanisms underlying these pro-oxidant strategies are summarized in Table 3.1. We find that mild oxidative stress results in reduced P/O and energy stress in vivo in mouse skeletal muscle before the development of intrinsic mitochondrial defects.

Table 3.1. Mechanisms for pro-oxidant strategies. Reactive oxygen species are denoted in red.

Compound	Structure	Action
Paraquat (PQ)	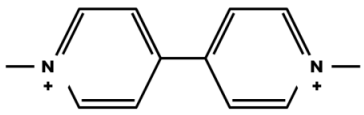	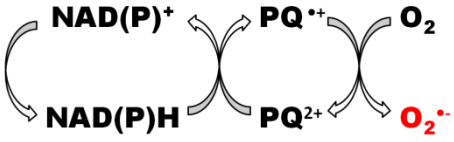
Cu-Zn Superoxide Dismutase (SOD1)	Homodimer Molecular Weight of 32.5kDa	
Glutathione (Reduced: GSH; Oxidized: GSSG)	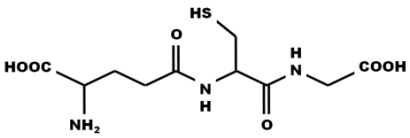	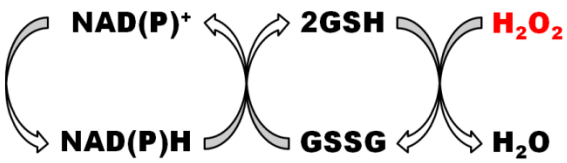

Methods

Animals

This study was approved by the Institutional Animal Care and Use Committee of the University of Washington. Male and female wild-type and $SOD1^{-/-}$ (117) C57BL/6J mice between the ages of 4 and 8 months and female $GCL^{+/+}$ and $GCL^{+/-}$ (108) C57BL/6 mice between 3 and 4 months of age were housed in an environment with a fixed temperature, exposed to a 12 hour light/dark cycle, and allowed free access to standard mouse chow until immediately prior to experimentation. Mice were anesthetized using 2.5% (w/v) tribromoethanol ("Avertin", Sigma, St. Louis, MO) in saline at a dose of 0.01mL/gram of body weight. Body temperature was maintained at 35°C +/- 1°C using heated air, and mice breathed 100% oxygen throughout in vivo experiments.

Paraquat Treatment

Paraquat (Item 36541, Sigma) was dissolved in saline and administered via intraperitoneal injections at a dose of 10 mg/kg of body weight. Mice received four injections over the span of 14 days (on days 1, 5, 8, and 12) for doses of 20mg/kg/week (PQ2), 10mg/kg/week (PQ1), or 0mg/kg/week (C). Group PQ2 received 10 mg/kg paraquat on all four injection days. Group PQ1 received volume-matched doses of saline on days 1 and 8 and 10 mg/kg paraquat on days 5 and 12. Group C received volume-matched saline on all four injection days. In vivo spectroscopy commenced two days after the final injection in all cases.

MR Spectroscopy

Single-mode MR spectroscopy was conducted following the methods described by Marcinek et al. (105). Anesthetized mice were secured horizontally in a vertical bore magnet (7 Tesla, Oxford Instruments, Oxford, UK) using flexible straps. The distal hindlimb was positioned within a three-turn solenoid RF coil tuned to ^{31}P (121.65 MHz), with a custom-built ischemia cuff positioned proximal to the coil. After shimming the proton peak using tissue water, a high signal to noise ^{31}P spectrum was acquired under fully relaxed conditions (32 acquisitions with a 25sec interpulse delay) to calculate the peak areas of inorganic phosphate (P_i), PCr, and ATP. We then collected 200 dynamic spectra (4 acquisitions per spectrum with a 1.5sec interpulse delay and a 45° flip angle for a time resolution of 6sec) during 2min of rest, 11min of ischemia, and 7min of recovery to monitor the change in PCr peak area over time. Fully relaxed peak areas were calculated by integration of processed spectra using VNMR software on a Varian Inova console. For dynamic spectra, two consecutive spectra were summed to increase signal-to-noise (reducing time resolution to 12sec) and peak areas relative to a standard spectrum were determined using the Fit to Standard algorithm (70).

Optical Spectroscopy

Single-mode optical spectroscopy was conducted following the methods described by Marcinek et al. (105). After MR spectroscopy, mice were allowed to recover for 24h and then re-anesthetized with Avertin. Hindlimbs were shaved using standard hair clippers and mice were positioned on a flat horizontal surface with the distal portion of their hindlimbs oriented between two fiber optic bundles just downstream of an ischemia cuff. One bundle directed light from a quartz-tungsten halogen light source (Newport/Spectra-Physics, Santa Clara, CA) onto the hindlimb. Light transmitted through the hindlimb was acquired by the second bundle and delivered to a spectrograph (InSpectrum, Acton, Acton, MA). Optical spectra were acquired at 1s intervals during 3min of rest, 7min of ischemia, and 10min of

recovery. Intensity spectra were converted to optical densities (OD) using a 1% intralipid reference. The second derivatives of OD spectra were analyzed using a partial least-squares (PLS) algorithm (Chapter 2, (154)) to isolate the contributions to absorbance of oxymyoglobin, myoglobin, oxyhemoglobin, and hemoglobin.

Ex vivo Mitochondrial Respiration

Respiratory complex activities were measured by monitoring the rate of oxygen consumption in the presence of complex-specific substrates and inhibitors. Complex activity was measured when ATP production was coupled through a functional respiratory chain with oxygen as the final electron acceptor and also measured in the presence of the proton ionophore carbonylcyanide m-chlorophenylhydrazone (CCCP), providing rates of maximal electron flux independent of the phosphorylation systems. Freshly dissected, gently separated and permeabilized (50μg/ml saponin, 4°C, 40min) EDL muscle fibers were stirred at 25°C in a 2ml vessel of an oxygen monitoring apparatus (O2k system, Oroboros Instruments, Austria) and provided with substrates in this order: for measuring proton leak (10mM glutamate/5mM pyruvate/2mM malate, without ADP), state 3 with complex I substrate (previous conditions with 2.5mM ADP), state 3 with complex I and II substrate (previous conditions with 10mM succinate), uncoupled (previous conditions with 2.5μM CCCP to measure maximal flux), uncoupled with complex I inhibition (i.e. complex II only; previous conditions with 0.5μM rotenone), finally 2.5μM antimycin A was added to measure the contribution of non-mitochondrial oxygen consumption followed by measurement of complex IV (0.5mM N,N,N',N'-tetramethyl-ρ-phenylenediamine (TMPD), 2mM ascorbate). Potassium cyanide (1mM) was used to confirm complex IV-specific activity. The amount of oxygen consumed was calculated by assuming the oxygen solubility factor of the media to be 0.920 and by calibrating initial oxygen concentration in the buffer for each experiment and correcting for pressure, temperature, and instrumental oxygen consumption as described by Gnaiger et al. (54).

Tissue Preparation

Muscles from the distal hindlimb (gastrocnemius, soleus, EDL, tibialis anterior) were dissected and flash-frozen in liquid nitrogen prior to death. These frozen muscles were pulverized over liquid nitrogen and mixed well to form a homogenous powder for F_2-isoprostane, metabolite, hemoglobin, and myoglobin analysis. The gastrocnemius from the contralateral leg was dissected, frozen, and pulverized in liquid nitrogen for other biochemical analyses.

Metabolite Concentration

Tissue concentrations of ATP and total creatine (i.e. PCr plus creatine) were measured in mixed muscle preparations including gastrocnemius and tibialis muscle following previously published protocols (83, 189). Muscle powder was thawed directly into 0.6M perchlorate, 5mM EDTA and centrifuged for 15 minutes at 13,000 RPM at 4°C. Supernatants were aspirated and neutralized using 0.6M potassium hydroxide, 40mM TES, 0.3M potassium chloride before being centrifuged a second time for 10 minutes at 5,000 RPM. Final supernatants were analyzed using HPLC (Waters, Milford, MA). PCr and ATP were separated using a gradient injection through a general purpose column (Supelcosil LC-18, #58298C40, Sigma-Aldrich, St. Louis, MO) with 90% 14.7mM KH_2PO_4, 1.15mM TBAHS (pH 5.3) plus 10% 215mM KH_2PO_4, 2.3mM TBAHS, 3% acetonitrile (pH 6.5) followed by 100% 215mM KH_2PO_4, 2.3mM TBAHS, 3% acetonitrile (pH 6.5) mobile phase buffers. Creatine was separated using isocratic injection through a strong cation-exchange column (#80002, Waters) with 25mM NaH_2PO_4 (pH 7.8) mobile phase buffer. Absorbance at 210nm (for PCr and creatine) and 254nm (for ATP) were detected and peaks were integrated using Breeze HPLC software (Waters). Peak areas were calibrated using standard solutions with known concentrations.

Protein Content

Ten to 20mg of pulverized muscle (whole leg or gastrocnemius) was homogenized in Cellytic MT (Item C3228, Sigma) with 0.015% (v/v) protease inhibitor (P8340, Sigma) and 1% (v/v) phosphatase inhibitor (Item #78420, Thermo Scientific, Waltham, MA) at a ratio of 1:25 (w/v). Homogenates were combined at a 1:1 (v/v) ratio with Laemmli sample buffer (#161-0737, Bio-Rad, Hercules, CA) with 350mM DTT, brought to 95° for 8min, and then centrifuged at 13,000 RPM for 10min. Supernatants were used for the following analyses. Hemoglobin and Myoglobin: Proteins were separated from mixed muscle homogenates using SDS-PAGE, stained with Coomasie Brilliant Blue (Bio-Rad), and imaged using a ChemiDoc imaging system (Bio-Rad). Hemoglobin and myoglobin band densities were measured using ImageJ and calibrated using hemoglobin and myoglobin standards that were run simultaneously. Western Blots: Proteins were separated from gastrocnemius samples using SDS-PAGE and transferred to nitrocellulose membranes before blocking and immunoblotting for selected proteins. For complex I subunit NDUFB8 (MS105, Mitosciences, Eugene, OR), complex II subunit 30 kDa (MS203/C1217, Mitosciences), complex IV subunit IV (MS407, Mitosciences) and ANT1 (#9299, Santa Cruz Biotechnology, Santa Cruz, CA), membranes were blocked overnight at 4°C in 5% NFDM, primary antibodies were diluted 1:1000 in 1% NFDM, and HRP-conjugated secondary antibodies (#7072, Cell Signaling, Danvers, MA) were diluted 1:20000 in 1% NFDM. Actin (AB14128, Abcam, Cambridge, MA) was probed simultaneously as an internal loading control. For UCP3 (AB3477, Abcam), AMPK (#2532, Cell Signaling), and phospho-AMPK (#2535, Cell Signaling), membranes were blocked for 1 hour at room temperature in 3% BSA, primary antibodies were diluted 1:1000 in 1% BSA, and HRP-conjugated secondary antibodies (#7074, Cell Signaling) were diluted 1:2500 in 1% BSA. α-Tubulin (#2125, Cell Signaling) was probed simultaneously as an internal loading control.

RT-PCR

RNA was extracted from liquid nitrogen pulverized gastrocnemius using the RNeasy Mini Kit (Qiagen, Valencia, CA) and cDNA libraries were created using the Omniscript RT Kit (Qiagen). Real time PCR was carried out using a Rotor-Gene 6000 (Corbett Research, Cambridge, UK). Primers were furnished by Dr. Rong Tian (UW Mitochondria and Metabolism Center, Seattle, WA) and analyses were performed using Rotor-Gene 6000 Series Software.

F_2-Isoprostanes

F_2-isoprostanes were determined through a collaboration with Dr. Holly van Remmen at the University of Texas Health Sciences Center, San Antonio using a stable isotope dilution method with detection by gas chromatography/negative-ion chemical ionization/mass spectrometry (GC-NICI-MS) as previously described (115). Briefly, 100-200mg of mixed muscle powder was homogenized in ice-cold Folch solution (chloroform/methanol 2:1) containing 5 mg/100ml butylatedhydroxytoluene. Lipids were then extracted and chemically hydrolyzed with 15% KOH. After acidification with HCl, a stable isotope, 8-*iso*-prostaglandin $F_{2\alpha}$-d_4 internal standard was added. Following extraction using C-18 and silica Sep-Pac cartridges, the eluted compounds were dried under nitrogen then converted to pentafluororobenzyl esters and purified by thin-layer chromatography. The purified F_2-isoprostanes were derivatized to trimethysilyl ether derivatives then dissolved in undecane for quantification by GC/MS. Negative ion chemical ionization MS was performed by Agilent 6890 GC and Model 5975 MSD instruments with selected ions monitored for [$^2H_4$]15-$F_{2\alpha}$-IsoP internal standard (*m*/*z* 573) and F_2-IsoPs (*m*/*z* 569).

Calculations

A more detailed description of our calculations is available in Chapter 2. A brief overview is presented below. MR Spectroscopy: PCr/ATP ratios from fully relaxed spectra were multiplied by ATP concentrations from HPLC to find resting in vivo PCr concentration. Using this as a reference, the slope from Fit-to-Standard was converted to an absolute PCr concentration for each spectrum. PCr breakdown over time was fit using a least-squares linear approximation, and PCr recovery after cuff release was fit using a least-squares monoexponential approximation. These fits were used to calculate the resting ATP synthesis rate and maximum ATP synthesis rate (16), respectively. Intracellular pH and AMP concentrations were calculated using the chemical shift between P_i and PCr and the known kinetics of the creatine kinase and adenylate kinase reactions assuming equilibrium conditions, as described in more detail elsewhere (56, 174). Optical Spectroscopy: The oxygen saturation of myoglobin from PLS was multiplied by absolute myoglobin concentration to find moles of oxygen bound to myoglobin and used to calculate total dissolved oxygen in the intracellular compartment using known oxygen-myoglobin binding kinetics at 37°C (152). An analogous approach was used to calculate moles of oxygen bound to hemoglobin and vascular dissolved oxygen using the oxygen saturation of hemoglobin from PLS. Oxygen consumption during ischemia was found using a least-squares linear approximation of change in total tissue oxygen content over time (105). All measures of oxygen consumption were made before oxygen became limiting to respiration as previously described (103).

Pulse Oximetry

Resting heart rate and arterial oxygen saturation were measured longitudinally in anesthetized mice using the MouseOx® pulse oximeter (Braintree Scientific, Inc., Braintree, MA) 0, 7, and 14 days into PQ treatment. Mice were anesthetized using a gas mixture of 2% isoflurane, 98% oxygen, hair was removed from a small area of the chest and neck using over-the-counter hair removal cream (Nair, Church &

Dwight Co., Princeton, NJ), and an infrared sensor was clipped to the skin over the carotid artery to make measurements.

Statistics

Statistical analyses were performed using Prism v5 (GraphPad, La Jolla, CA). In cases where three groups were compared (i.e. C, PQ1, and PQ2), one-way ANOVA was used to determine significance and Dunnett's post hoc test was used to determine significance of individual treatment groups vs. control. In cases where two groups were compared (e.g. PQ2 vs. C or $SOD1^{-/-}$ vs. WT), two-tailed Student's t-tests were conducted. Two-way ANOVA was used to determine the effect of SOD1 knock-out on multiple electron transport chain complexes.

Results

PQ treatment leads to oxidative stress in skeletal muscle

We used MR and optical spectroscopy to measure the effect of increased oxidative stress on in vivo mitochondrial function in skeletal muscle. Representative ^{31}P MR and optical spectra of the mouse hindlimb during rest and at the end of ischemia are illustrated in Fig. 3.1. MR spectra of skeletal muscle reveal the decrease in phosphocreatine (PCr) during ischemia while ATP levels remain constant (Fig. 3.1A). Optical spectra become broader with a more pronounced peak at 760nm as hemoglobin and myoglobin transition from their oxygenated to deoxygenated states during ischemia (Fig. 3.1B). Table 1 lists resting levels for key metabolites used to determine in vivo mitochondrial fluxes.

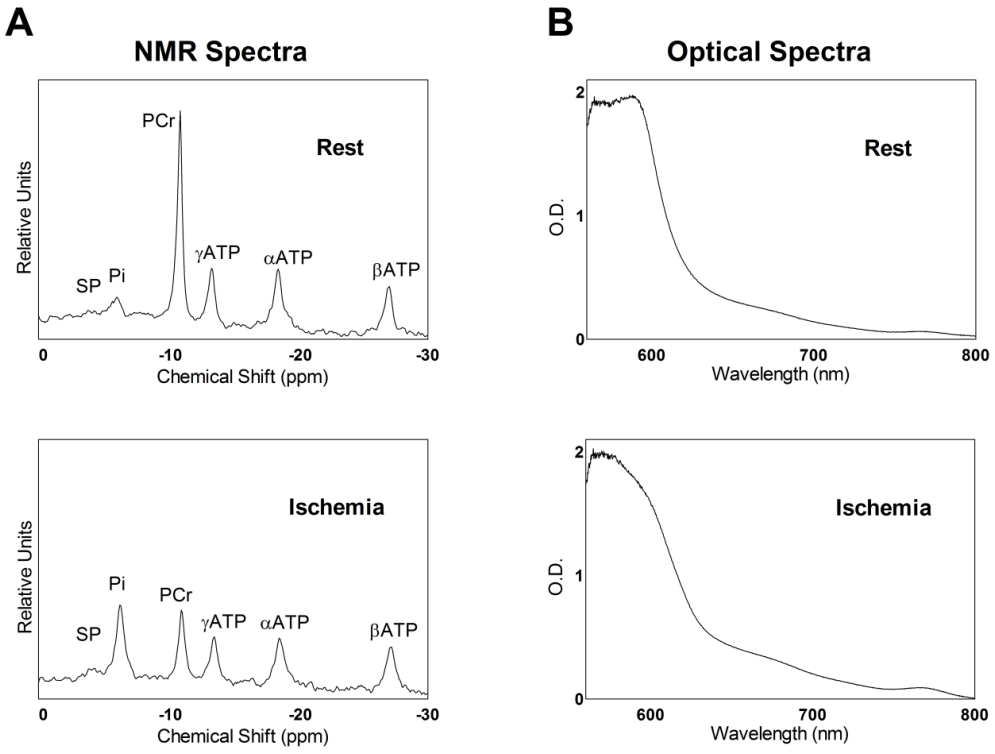

Figure 3.1. In vivo spectra exhibit distinct differences under resting and ischemic conditions. (A) MR spectra collected during rest (top) and after 10min of ischemia (bottom). (B) Optical spectra collected at rest (top) and after 6min of ischemia (bottom).

To better understand the effect of short term oxidative stress we treated wild-type C57Bl/6J mice with low doses of PQ to induce a mild oxidative stress. Mice were injected either once (PQ1) or twice (PQ2) a week for two weeks with 10mg PQ/kg body weight, while controls (C) received volume-matched doses of saline. We measured F_2-isoprostanes in skeletal muscle of the hindlimb as a marker of oxidative stress. Fig. 3.2 shows that PQ treatment induced a significant, dose-dependent oxidative stress in skeletal muscle. We also observed significant differences in body weight in both PQ1 (0.3%±1.2% decrease, $p < 0.05$) and PQ2 (2.9%±1.2% decrease, $p < 0.01$) over the course of treatment relative to controls (5.8%±2.6% increase). To ensure that our measurements of in vivo mitochondrial function were not affected by systemic effects of PQ treatment on the cardiovascular system we measured resting heart rate and arterial oxygen saturation in anesthetized mice and found no effect of PQ treatment on these parameters (Fig. 3.3).

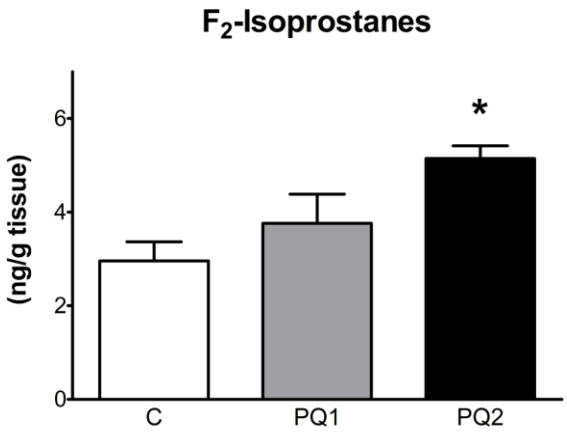

Figure 3.2. PQ-treatment caused a dose-dependent increase in F_2-isoprostanes in mouse skeletal muscle. Data are expressed as means ± SEM with n=4-5 per group. (* $p < 0.05$ relative to control)

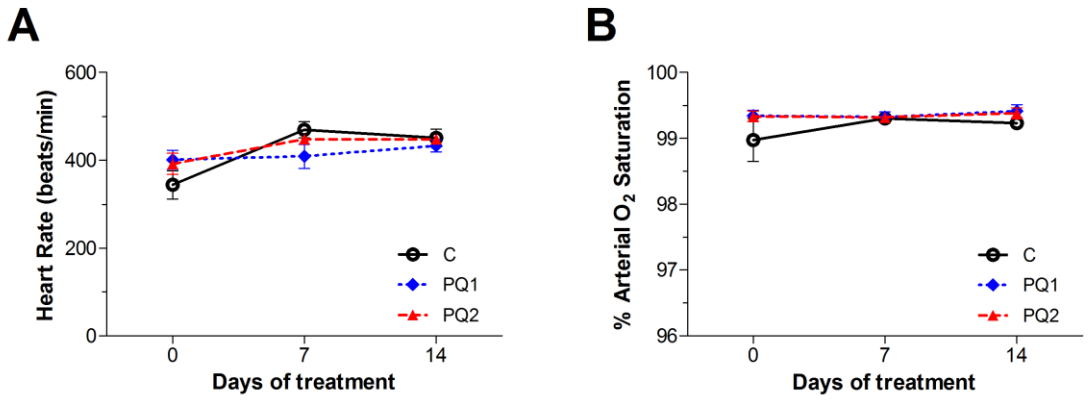

Figure 3.3. (A) Heart rate and (B) arterial hemoglobin oxygen saturation were measured before (0 days), after 7 days and following 14 days of PQ treatment. There was no significant effect of PQ treatment on either variable at any time point. Data are expressed as means ± SEM, n=5.

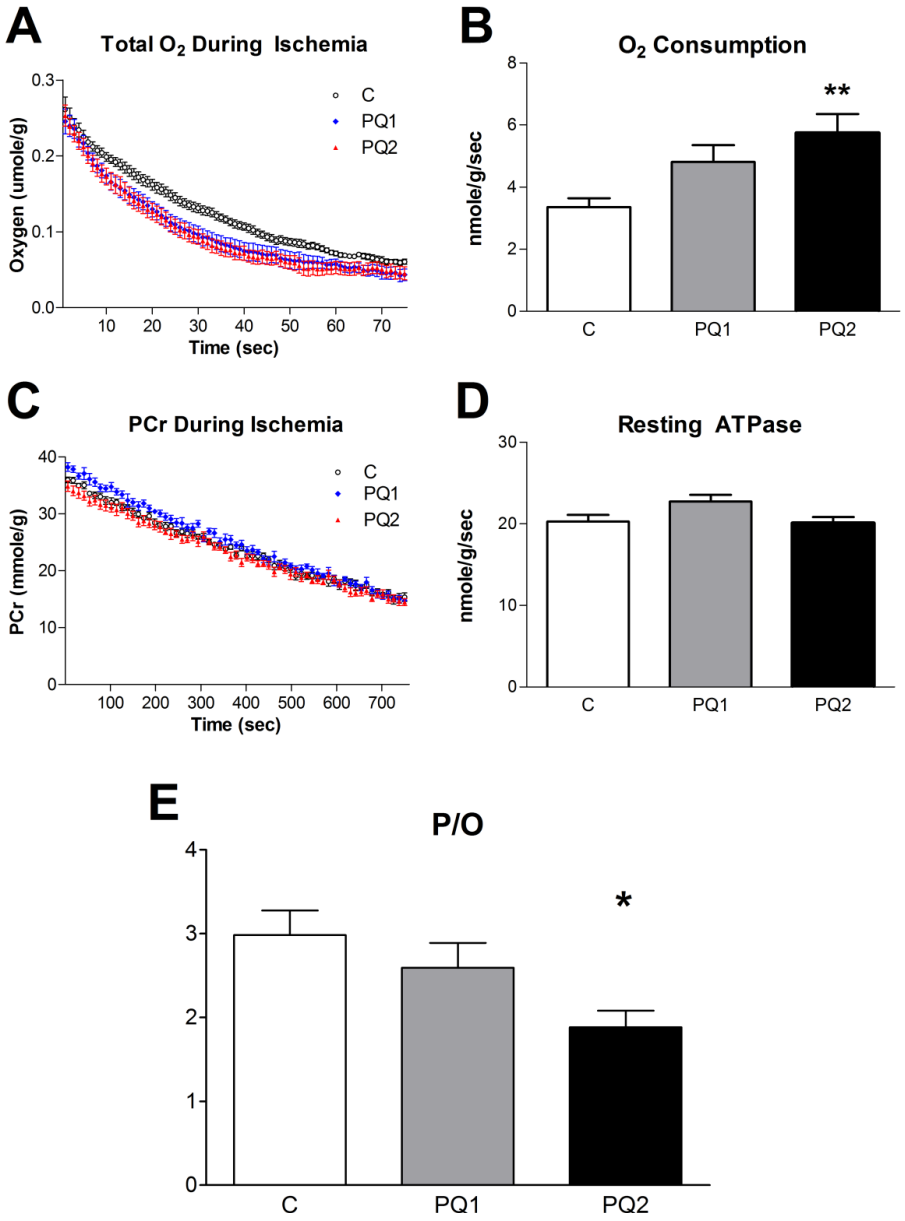

Figure 3.4. PQ led to a significant, dose-dependent increase in oxygen consumption (A and B; pre-oxygen limited slope of A used to calculate values represented in B) but had only a minor effect on resting ATP production (ATPase) rate (C and D; slope of C used to calculate values represented in D). The ratio of ATP produced per O_2 consumed (P/O ratio) is significantly decreased in a dose-dependent manner with PQ treatment (E). Data are expressed as means ± SEM with n=8-9 per group. (* $p < 0.05$, ** $p < 0.01$ relative to control).

Reduced P/O and energy stress with PQ treatment

Resting in vivo mitochondrial oxygen consumption in the hindlimb skeletal muscle of young female mice increased significantly with PQ treatment (Fig. 3.4A and 3.4B). In addition, resting in vivo myoglobin saturation was negatively correlated with oxygen consumption due to the increased oxygen demand of the muscle (Fig. 3.5). However, the resting rate of mitochondrial ATP production was unchanged (Fig. 3.4C and 3.4D). This resulted in a dose-dependent decrease in P/O ratio (ATP production/O_2 consumption divided by 2) with PQ treatment (Figs. 3.4E).

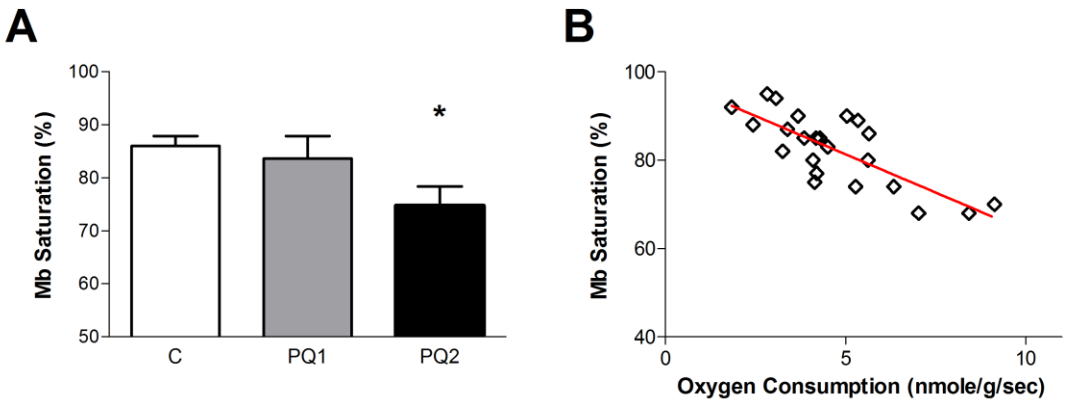

Figure 3.5. (A) A significant decrease in resting myoglobin (Mb) saturation with PQ treatment indicates an increased mitochondrial demand on oxygen delivery systems with uncoupling. n =8-9, * $p < 0.05$. (B) There is a significant negative correlation between resting myoglobin saturation and in vivo mitochondrial oxygen consumption in PQ mice ($p < 0.0001$).

To measure the effect of increased oxidative stress on the functional capacity of mitochondria we determined in vivo ATPmax by measuring the rate of recovery of PCr from ischemia in the mouse hindlimb (16). Despite the reduction in P/O ratio, ATPmax was not different between groups (Fig. 3.6).

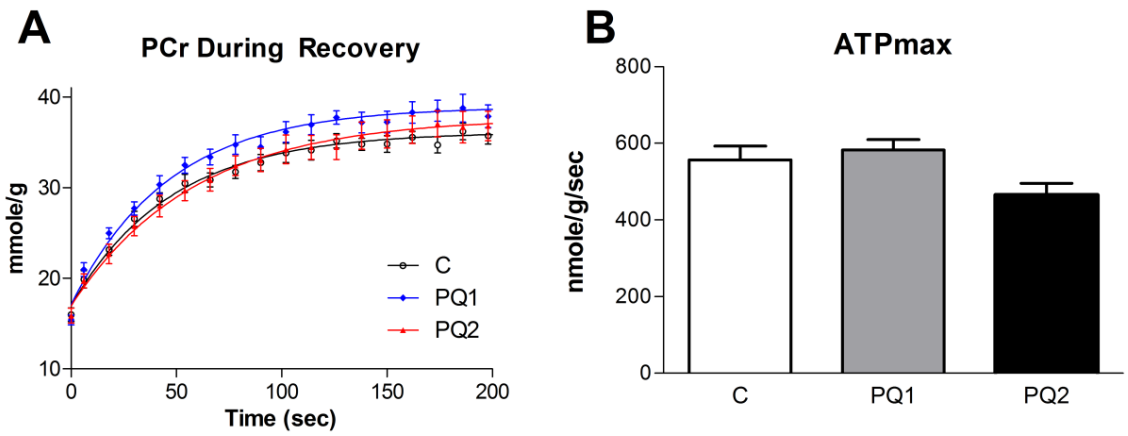

Figure 3.6. Mild oxidative stress does not affect in vivo ATPmax. Neither PCr recovery (A) nor ATPmax (B) changed significantly with either dose of PQ, although the decrease in ATPmax of group PQ2 trended down ($p < 0.1$). Data are expressed as means ± SEM with n=8-9 per group. (* $p < 0.05$ relative to control)

Biochemical and molecular evidence indicates that PQ treatment disrupted energy homeostasis in vivo in skeletal muscle. The PCr/ATP ratio in resting skeletal muscle declined in a dose-dependent manner with increasing PQ treatment (Fig. 3.7A). This decrease in PCr/ATP led to a trend toward elevated AMP concentrations in both treated groups (C: 104.4nM ± 16.1nM, PQ1: 156.7nM ± 48.0nM, PQ2: 174.5nM ± 38.3nM). Further evidence that PQ treatment led to a disruption in energy homeostasis comes from increased phosphorylation of the cell energy sensing protein, 5' AMP-activated protein kinase (AMPK) in the PQ2 group relative to controls (Fig. 3.7B).

To ensure that the differences in P/O and PCr/ATP were not gender-specific we measured in vivo parameters in a small cohort of male mice. As illustrated in Fig. 3.8, P/O and PCr/ATP both decreased in response to PQ treatment.

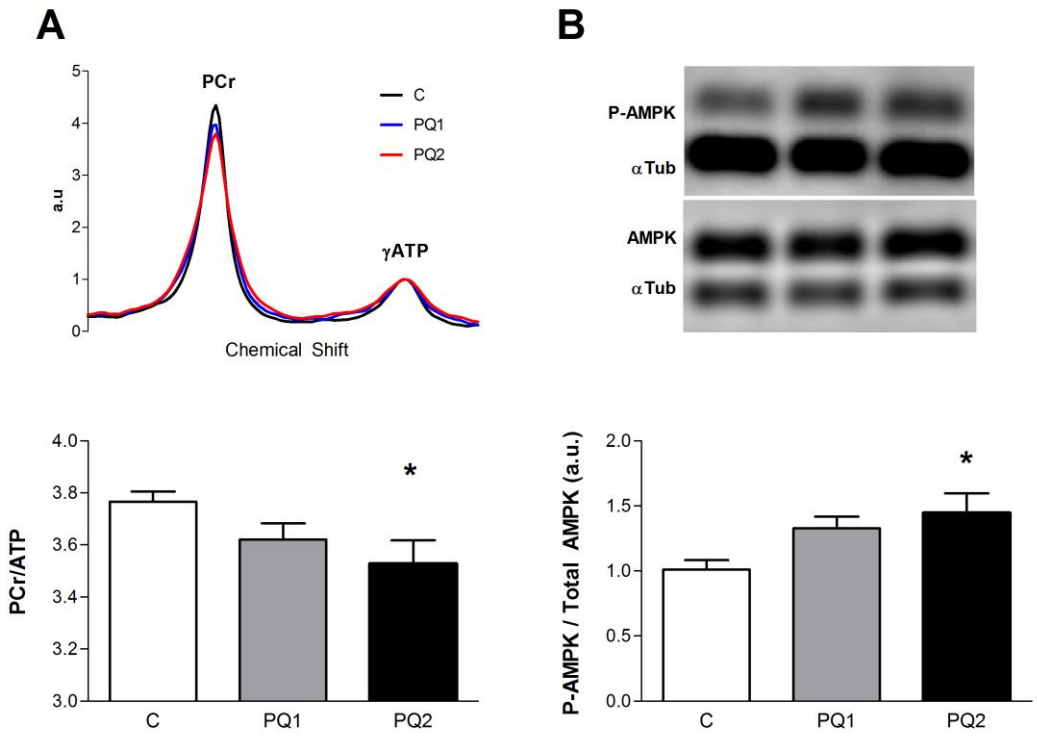

Figure 3.7. PQ-treatment causes energy stress in vivo and activates energy sensing pathways. PCr/ATP ratio decreases with PQ treatment (A, with representative MR spectra above) and the ratio of phosphorylated AMPK to total AMPK increased (B, with representative western blot above). Data are expressed as means ± SEM with n=5-9 per group. AMPK data are normalized to control average. (* $p < 0.05$ relative to control)

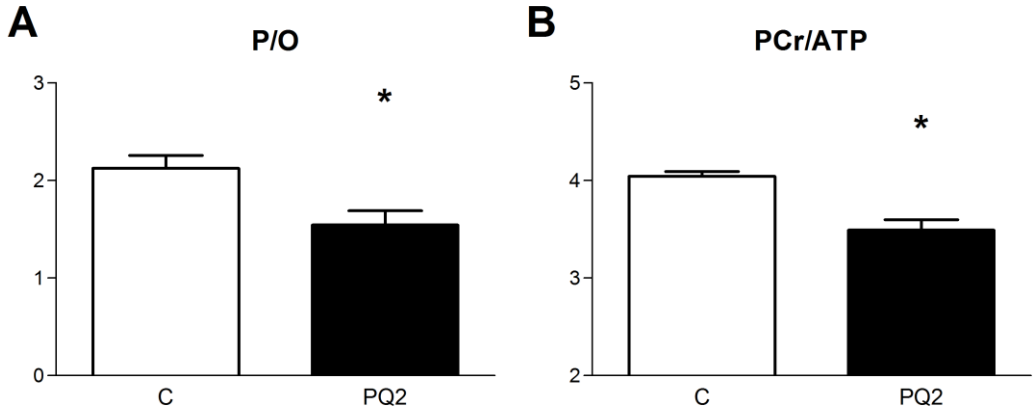

Figure 3.8. Treatment with 20mg/kg PQ per week for two weeks leads to (A) decreased coupling of oxidative phosphorylation as measured by P/O ratio and (B) increased energy stress as measured by PCr/ATP ratio in male mice. Data are expressed as means±SEM, n=3, * $p < 0.05$.

Mild PQ treatment does not affect intrinsic mitochondrial function

To determine whether the reduction in in vivo P/O with PQ treatment was due to changes intrinsic to the mitochondria or due to interactions between mitochondria and the cellular environment (e.g. ROS) we measured mitochondrial respiration in permeabilized muscle fibers. We found no effect 2 week treatment with 20mg/kg/week PQ ("PQ2") on proton leak driven respiration, maximal ADP stimulated respiration with complex I substrate (state 3, complex I), maximal ADP stimulated respiration with complex I and II substrates (state 3, complex I & II), uncoupled respiration, uncoupled respiration with complex I inhibition (i.e. complex II only), or complex IV respiration (Figs. 3.9A and 3.9B). These results indicate that mitochondrial electron transport chain function was not affected by this mild oxidative stress.

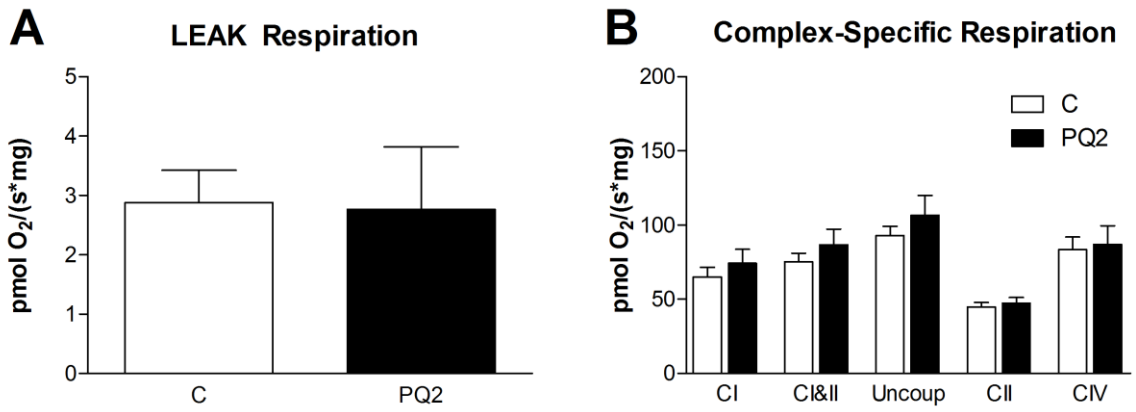

Figure 3.9. PQ-treatment had no effect on ex vivo respiration of permeabilized EDL. (A) We detected no difference in leak driven respiration between control and PQ2 in the permeabilized EDL. (B) State 3 with complex I substrate ("CI"), state 3 with complex I and II substrates ("CI&II"), uncoupled ("Uncoup"), uncoupled with complex I inhibition ("CII"), and complex IV ("CIV") respiration were also unchanged in group PQ2. Data are expressed as means ± SEM with n=5 per group.

We next looked for changes in expression of genes and proteins relevant to mitochondrial content and function in mixed gastrocnemius to account for loss of in vivo P/O and maintenance of mitochondrial capacity. We found no effect of 2 week treatment with 20mg/kg/week PQ ("PQ2") on gene expression of peroxisome proliferator-activated receptor gamma coactivator 1- α (PGC1α), mitochondrial transcription factor A (TFAM), the D-loop control region of mitochondrial DNA (DCR), UCP3, or ANT1 (Fig. 3.10A). There was also no difference in the content of the mitochondrial proteins NDUFB8 of complex I, 30 kDa subunit of complex II, subunit IV of cytochrome oxidase, UCP3, or ANT1 (Fig. 3.10B).

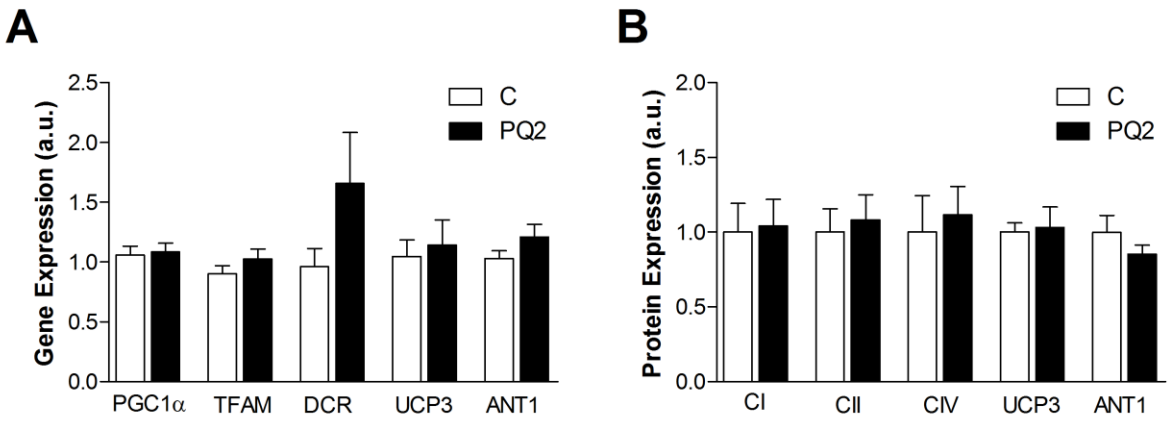

Figure 3.10. PQ treatment did not alter mitochondrial content or composition. (A) We detected no differences between control and PQ2 in gene expression of mitochondrial regulators PGC1α and TFAM, the d-loop control region of mitochondrial DNA (DCR), UCP3, or ANT1. (B) We also did not detect changes in protein expression of complexes I, II, or IV, UCP3, or ANT1 in PQ2 animals. Data are expressed as means ± SEM, normalized to control averages. n=5 per group.

Oxidative stress leads to in vivo mitochondrial uncoupling in GCL$^{+/-}$ mice

We measured in vivo mitochondrial energetics in GCL$^{+/-}$ mice and GCL$^{+/+}$ littermates following the same 2 week treatment with either PQ (i.e. "PQ2") or saline (i.e. "C") that we presented in wild-type mice above. GCL$^{+/-}$ mice are deficient in the molecular antioxidant glutathione due to reduced levels of the rate limiting enzyme in glutathione synthesis, glutamate-cysteine ligase (GCL). As a result, GCL$^{+/-}$ mice have been documented to have increased susceptibility to oxidative stress-related disease (186).

Associated with this expected increase in oxidative stress, P/O ratio was significantly lower in untreated $GCL^{+/-}$ mice, relative to $GCL^{+/+}$ littermates. Similar to wild-type mice from the first portion of this study, littermate $GCL^{+/+}$ control mice responded to 2 weeks of PQ treatment with a reduction in P/O. This downward trend was observed with 2 weeks of PQ treatment in $GCL^{+/-}$ mice, though no significant difference was observed (Fig. 3.11). Neither PCr/ATP ratio (Table 3.2) nor ATPmax (data not shown) were different between any groups in this portion of the study

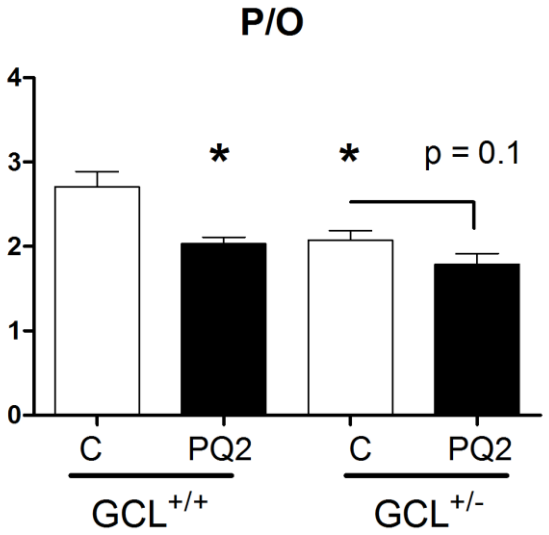

Figure 3.11. . P/O ratios were lower in untreated $GCL^{+/-}$ mice than in littermate controls. Two-weeks of PQ-treatment led to a decrease in P/O in $GCL^{+/+}$ mice, and a subtle downward trend in P/O in $GCL^{+/-}$ mice. Data expressed as means±SEM, n=3-4. *p<0.05 relative to $GCL^{+/+}$ controls.

Oxidative stress leads to in vivo mitochondrial uncoupling in $SOD1^{-/-}$ mice

As reported previously, the absence of SOD1 leads to increased oxidative stress in mice (117). We confirmed this finding as an increase in F_2-isoprostanes in gastrocnemius of $SOD1^{-/-}$ mice (Fig. 3.12). While neither ATP production nor oxygen consumption was different in $SOD1^{-/-}$ mice (data not shown), P/O ratio was significantly reduced (Fig. 3.13A). ATP and creatine were also lower in $SOD1^{-/-}$ mice vs. wild-type (WT) littermates (Table 3.2).

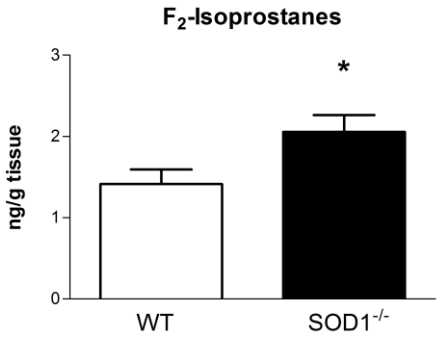

Figure 3.12. The absence of SOD1 leads to an increase in F_2-Isoprostanes in muscle of female $SOD1^{-/-}$ mice. Data means±SEM, n=4, * p < 0.05

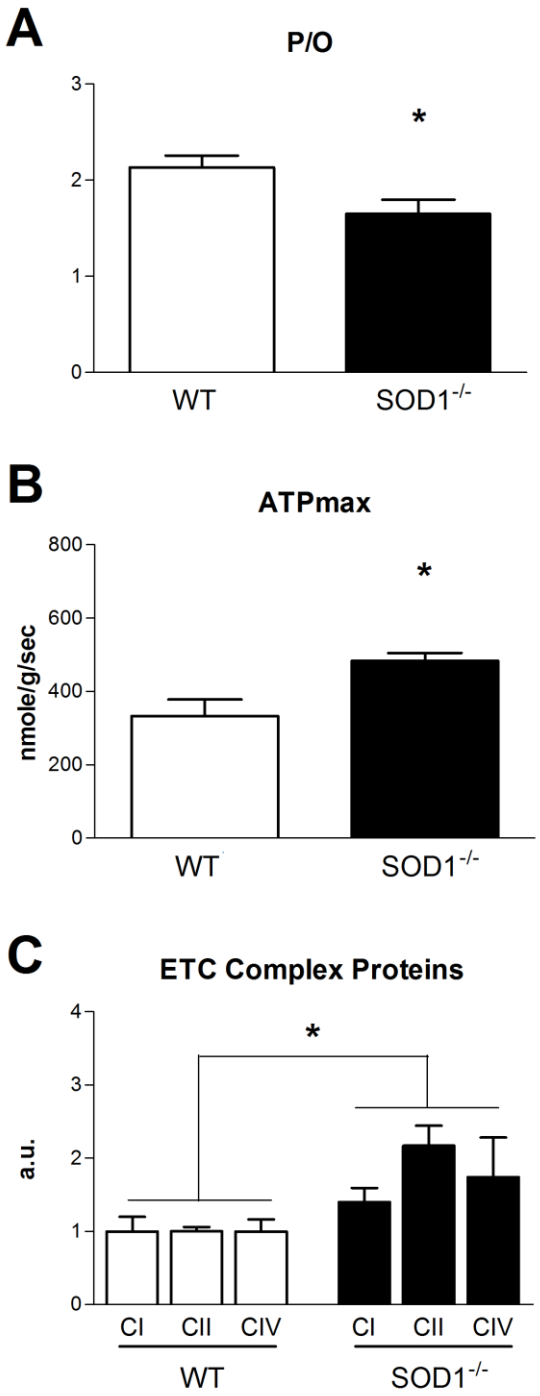

Figure 3.13. (A) Coupling of oxidative phosphorylation was lower in $SOD1^{-/-}$ mice, as reflected by a significant decrease in P/O. (B) Despite this loss of efficiency, ATPmax was higher in $SOD1^{-/-}$ mice. (C) Protein expression of complexes I, II, and IV was also significantly higher in $SOD1^{-/-}$ mice. Data are expressed as means ± SEM with n=4-5 per group. In C, data are normalized to control averages. Significant effect of genotype determined by two-way ANOVA. (* $p < 0.05$)

Increased phosphorylation capacity in SOD1$^{-/-}$ skeletal muscle

We found that ATPmax was significantly higher in mice lacking SOD1 (Fig. 3.13B). This increase in ATPmax contrasts with the effect of short term oxidative stress in PQ-treated mice and suggests a compensatory increase in mitochondrial content with chronic oxidative stress in SOD1$^{-/-}$ mice. Elevation of electron transport chain complexes I, II, and IV in the mixed gastrocnemius of SOD1$^{-/-}$ mice (Fig. 3.13C) was associated with increased ATPmax.

Table 3.2. Metabolite concentrations in muscles of the mouse hindlimb. ATP and total creatine (Cr) were determined using HPLC, and other values were calculated using MR spectra with ATP as an internal standard (Cr was not measured for GCL mice). All data are expressed as mean ± SEM. n = 8-9 for PQ, n=4-5 for SOD1, and n = 4 for GCL. * $p < 0.05$ relative to control.

Study	Group	PCr/ATP	ATP(mM)	Cr (mM)	PCr (mM)	P_i (mM)	pH_{rest}
PQ	C	3.77±0.04	9.52±0.41	49.2±1.5	35.77±0.36	2.52±0.23	7.11±0.03
	PQ1	3.62±0.06	10.46±0.28	51.9±2.3	38.02±0.65*	2.99±0.31	7.07±0.02
	PQ2	3.53±0.09*	9.82±0.20	49.3±1.4	34.56±0.88	3.04±0.23	7.13±0.02
SOD1	WT	3.61±0.16	8.00±0.92	41.1±2.6	28.90±2.56	3.11±0.17	7.08±0.02
	SOD1$^{-/-}$	3.84±0.13	6.48±0.80*	30.0±3.6*	25.50±1.61*	3.77±0.34	7.14±0.03
GCL$^{+/+}$	C	3.53±0.15	9.90±0.31	x	34.99±2.26	2.73±0.14	7.12±0.01
	PQ2	3.16±0.18	10.20±0.48	x	31.47±1.19	2.71±1.02	7.06±0.01
GCL$^{+/-}$	C	3.51±0.10	9.90±0.34	x	34.73±1.38	2.97±0.47	7.18±0.05
	PQ2	3.44±0.16	9.69±0.71	x	33.30±2.21	2.83±0.33	7.12±0.04

Discussion

We demonstrate that mild oxidative stress induced by either PQ treatment or genetic antioxidant deficiencies ($SOD1^{-/-}$ or $GCL^{+/-}$) reduces the coupling of oxidative phosphorylation in vivo and disrupts skeletal muscle energetics. These results provide an in vivo test of the "uncoupling to survive" hypothesis, which proposes that oxidative stress activates mitochondrial proton leak and reduces the coupling of oxidative phosphorylation (20). Production of both ATP and ROS are linked to the inner mitochondrial membrane potential ($\Delta\psi$), which is generated as protons are pumped from the matrix to the inner membrane space by the oxygen-consuming redox reactions of the electron transport chain (88, 113). The "uncoupling to survive" hypothesis suggests that oxidative stress leads to an increase in mitochondrial proton leak, and therefore a reduction of $\Delta\psi$, as a negative-feedback mechanism that mitigates further production of mitochondrial ROS (175). As a result of this proton leak, the F_1F_0ATPsynthase is bypassed and the net result is a reduction in the ATP produced per oxygen consumed (lower P/O).

In vivo P/O values were significantly reduced in both short-term (2 week PQ treatment) and chronic ($GCL^{+/-}$ and $SOD1^{-/-}$) models. The 10mg/kg of PQ administered once or twice per week in this study was sufficient to induce an increase in markers of oxidative stress, but this PQ dose is well below the LD50 of 70 mg/kg reported for mice when PQ is dissolved in saline and administered intraperitoneally (42). Thus the absence of an acute effect on oxygen delivery to skeletal muscle or severe mitochondrial dysfunction is not surprising. Instead we observed a significant control of mitochondrial metabolism and energetics. Resting mitochondrial ATP production rate fluctuated less than 15% with PQ treatment indicating that this level of oxidative stress did not greatly alter resting ATP demand of skeletal muscle. However, oxygen consumption increased by 43% in PQ1 and 71% in PQ2 to meet this unchanged ATP demand as a result of the reduced coupling of oxidation to phosphorylation. These results are similar to those from

isolated mitochondria and cells, where increased proton leak can be induced by adding exogenous oxidants to the assay (47, 48).

We used permeabilized muscle fibers to test whether the in vivo effects on mitochondrial function were due to changes intrinsic to the mitochondria or were the result of the interaction between the mitochondria and the cellular environment. No difference in mitochondrial respiration in permeabilized EDL between the PQ-treated and control groups, including proton leak driven respiration, indicates that the decreased coupling observed in vivo was not due to oxidative damage or a change in the composition of the mitochondria. These changes would be intrinsic to the mitochondria and persist after the fibers were permeabilized and the cell environment was replaced by respiration buffer. Further, analysis of gene and protein expression in mixed gastrocnemius revealed no differences in regulators of mitochondrial biogenesis (PGC1α and TFAM), mitochondrial content (DCR and complexes I, II, and IV), or mitochondrial uncouplers (UCP3 and ANT1) in PQ-treated mice. Therefore, we conclude that the reduced in vivo P/O is due to direct control of mitochondrial function by ROS or a related by-product.

Reduced in vivo coupling with PQ was not due to an upregulation of UCP3 or ANT1 expression in the muscle. The difference between our results and previous reports indicating that UCP3 and ANT1 are upregulated in response to oxidative stress may be due to differences in the magnitude of the oxidative stress or the short duration of the treatment. The previous studies in cell culture measured expression levels hours following an acute, high dose oxidative stress (166), while the PQ treatment employed in this study involved a relatively low level of stress induced over a period of two weeks. The lack of difference in expression levels of UCP3 and ANT1 does not preclude a role for these proteins in the reduced mitochondrial P/O in vivo. Activation of UCP3 or ANT1 mediated proton leak by oxidative stress or lipid peroxides (46, 47, 119) in vivo provides a potential mechanism to explain the difference between our

in vivo and permeabilized fiber results. Exchange of the cell environment and loss of potential activators of UCP3 or ANT1 during the permeabilization process would reverse the increased proton leak measured in vivo with PQ treatment.

Chronic oxidative stress due to the absence of SOD1 also reduced the efficiency of oxidative phosphorylation. In previous studies, respiratory control ratios (state 3/state 4 respiration) in isolated mitochondria were significantly reduced in 20 month old $SOD1^{-/-}$ mice, associated with decreased mitochondrial ATP production, loss of skeletal muscle mass, and increased mitochondrial H_2O_2 production (77, 117). In this study, the elevated ATPmax and increased expression of mitochondrial proteins and transcripts in $SOD1^{-/-}$ mice suggests that oxidative stress and uncoupling in young adult $SOD1^{-/-}$ mice induce a compensatory increase in mitochondrial capacity. The more severe effects on mitochondrial dysfunction reported in $SOD1^{-/-}$ mice at older ages are likely due to accumulation of oxidative damage to mitochondria and decline in ATP produced per mitochondria (77). The increase in mitochondrial proteins in $SOD1^{-/-}$ mice is supported by the growing evidence that ROS are important regulators of mitochondrial biogenesis. Treatment of renal proximal tubular cells and neural cells with H_2O_2 in culture induces mitochondrial biogenesis and upregulation of mitochondrial antioxidants (140, 166). The absence of an effect of PQ treatment on mitochondrial biogenesis in this study may be due low level or short duration of the stress.

Glutathione deficient $GCL^{+/-}$ mice exhibited a reduction in P/O similar to that of $SOD1^{-/-}$ mice, and responded to 2 weeks of PQ treatment similar to WT mice. An interesting body of literature has developed since conducting these studies, suggesting that post-translational glutathionylation of UCP3 acts as a regulatory switch over uncoupling activity (99-101). This work suggests that UCP3-mediated proton leak is inhibited by glutathionylation of one of a few possible cysteine residues within the protein.

Under conditions of oxidative stress, glutathione is required for the decomposition of hydrogen peroxide catalyzed by glutathione peroxidase (Table 3.1), resulting in the deglutathionylation of a greater fraction of the latent UCP3 protein population. As a result, the inhibition is removed and UCP3 mediated proton leak is allowed to take place. Our results are consistent with this hypothesis, as the decreased P/O in $GCL^{+/-}$ mice may be a result of a greater fraction of deglutathionylated UCP3 resulting from glutathione deficiency. This conclusion is speculative and should be addressed by research efforts in the future.

Reduced P/O is associated with disruption of energy homeostasis as indicated by the lower PCr/ATP ratios in PQ treated mice. The mitochondrial membrane potential provides a mechanistic link between cell energy state and the coupling of oxidative phosphorylation and imposes a thermodynamic limit on the ATP/ADP ratio that can be maintained (121). Therefore, as resting membrane potential decreases due to the increased proton leak across the inner mitochondrial membrane, the resting ATP/ADP ratio also decreases leading to a lower PCr/ATP and elevated AMP levels through the creatine kinase and adenylate kinase reactions (90). Thus we find that mild oxidative stress is associated with increased energy stress and elevated resting oxygen consumption in resting skeletal muscle.

Although PCr/ATP ratio was maintained in $SOD1^{-/-}$ mice, the significant decrease in ATP concentration provides evidence of energy stress in the case of chronic oxidative stress. We have previously reported a loss of resting ATP levels in vivo associated with reduced P/O in aged skeletal muscle from both mouse (106) and humans (4). However, we cannot rule out the possibility that lower ATP concentrations are due to heterogeneity of cell health and ATP concentration within the skeletal muscle of the hindlimb. Our in vivo MR and HPLC measurements of ATP are taken over the entire distal hindlimb, so we cannot account for local differences or loss of ATP in severely damaged fibers. These types of variation may reduce the

volume averaged resting ATP levels and provide an alternative explanation for the lower ATP in SOD1$^{-/-}$ mice.

Maintenance of cell energy homeostasis is an important determinant of cell health and survival (160). Thus energy stress is a key adaptive signal that modifies gene and protein expression through multiple energy sensing signaling molecules such as AMPK and related kinases (87). AMPK phosphorylation is sensitive to the cell ATP/AMP ratio (176), which is biochemically linked to the PCr/ATP ratio through the creatine kinase and adenylate kinase reactions (44, 49). Activation of AMPK through increased phosphorylation controls downstream pathways to reduce energy use (17) and increase energy production to restore energy homeostasis (176, 197). However, increased activation of AMPK has also been shown to contribute to increases in cell death and muscle atrophy (30, 146, 182). Therefore, an initial adaptive response by the cell to restore energy homeostasis may ultimately have pathological outcomes in the presence of a chronic energy or oxidative stress.

In conclusion, we demonstrate that mild oxidative stress leads to reduced mitochondrial coupling and cell energy stress in vivo. Thus reduced in vivo P/O may provide a mechanism that links mild oxidative stress to the activation of energy sensitive signaling processes. We demonstrate that this mitochondrial uncoupling and energy stress precedes severe defects in mitochondrial function or impaired ATP production and may serve as an early biomarker for disruption of normal mitochondrial function by oxidative stress.

Chapter 4

Impaired Adaptability of In Vivo Mitochondrial Energetics to Acute Oxidative Insult in Aged Skeletal Muscle*

Abstract

Periods of elevated reactive oxygen species (ROS) production are a normal part of mitochondrial physiology. Despite this, little is known about age-related changes in the functional response of mitochondria to periods of elevated ROS in vivo. Significantly, ROS-induced uncoupling of oxidative phosphorylation has received much attention as an important negative feedback mechanism to mitigate mitochondrial ROS production. Here we use a novel multi-modal in vivo spectroscopy system to test the hypothesis that ROS-induced uncoupling is diminished in aged mitochondria. This multi-modal system simultaneously acquires ^{31}P magnetic resonance (MR) spectra and near-infrared optical spectra to non-invasively measure phosphometabolite and oxygen concentrations in mouse skeletal muscle. Using low dose paraquat (PQ) injections to elevate intracellular ROS we use this approach to assess changes in in vivo mitochondrial function in young, middle aged, and old mice. Oxidative phosphorylation was uncoupled (decreased P/O) to the same degree in response to ROS at each age, but this decrease in P/O was associated with a loss of phosphorylation capacity and decreased ATP content in old mice only. Using mice lacking UCP3 we demonstrate that ROS-induced uncoupling in vivo is not entirely dependent upon this putative uncoupler of skeletal muscle mitochondria. These data indicate that ROS-induced uncoupling is maintained throughout life, but that acute periods of elevated ROS lead to mitochondrial deficits and loss of ATP in aged organisms that may contribute to impaired function and degeneration.

**A significant portion of this chapter is under review in almost this exact form, May, 2012.*

Introduction

Mitochondrial dysfunction is implicated in many age-related disorders, including loss of muscle mass and function (sarcopenia) (107), exercise intolerance (34), and neurodegeneration (53). In humans, these effects are associated with diminished mobility, lost quality of life, and stress on health care systems in countries with aging populations (92).

The accumulation of oxidative damage resulting from increased oxidative stress contributes to mitochondrial dysfunction in aging and disease (65, 68, 77). Mitochondria generate reactive oxygen species (ROS) in the form of superoxide anion at complexes I and III of the electron transport chain (ETC) as a normal byproduct of aerobic metabolism (76, 165). As a result of their proximity to the ETC, mitochondrial proteins, lipids, and DNA incur significant oxidative damage. In skeletal muscle, evidence suggests that oxidative damage to mitochondria is linked to reduced oxidative phosphorylation capacity (124), degeneration of neuromuscular junctions (77), and apoptosis (133).

Periods of elevated oxidative stress are a normal part of physiological processes. For example, mitochondrial ROS production is elevated following exercise (6) and during high fat feeding (5). Consequently, mitochondria have evolved intrinsic antioxidant defense mechanisms. One such proposed mechanism is ROS-induced uncoupling of oxidative phosphorylation, in which oxidative stress activates pathway(s) which dissipate the inner mitochondrial membrane (IMM) potential without generating ATP (20, 47, 159). Because ROS production by the ETC is driven by a high IMM potential (88), the capacity for ROS generation is diminished at the cost of reduced efficiency of oxidative phosphorylation. This type of feedback mechanism is important for maintaining redox homeostasis during transient increases in mitochondrial ROS production (6, 101). Evidence for this hypothesis comes from recent work demonstrating that increases in oxidative stress result in reduced in vivo P/O in skeletal muscle (Chapter 3, (158)) and studies that suggest that lower P/O ratios are protective against age-related dysfunction (4, 164).

Despite the importance of ROS-induced uncoupling in reducing mitochondrial ROS production and maintaining redox homeostasis, little is known about the effect of aging on ROS-induced uncoupling. Age-related decreases in mitochondrial efficiency and phosphorylation capacity (4, 34, 106) suggest that the flexibility of mitochondria to mildly uncouple in response to changing intracellular environments may be compromised. The diminishing utility of this mechanism with age would represent a loss of an antioxidant defense and may contribute to the age-related buildup of oxidative damage despite inconsistent changes in molecular antioxidant systems (162). Furthermore, the link between ROS-induced uncoupling and cellular energetics may present a unique challenge to old organisms that are already struggling to maintain energy balance (4, 106, 188).

Here we test the hypothesis that age-related deficiencies in mitochondrial function disrupt the ROS-induced uncoupling mechanism, rendering old cells more susceptible to the development of oxidative damage and supporting a critical role of mitochondria in the aging process. To address this hypothesis we use a multi-modal in vivo spectroscopy system capable of acquiring simultaneous magnetic resonance (MR) spectra and near infrared (NIR) optical spectra from skeletal muscle in the fully intact mouse hindlimb. We use a mild paraquat (PQ) treatment to induce an acute oxidative insult in mice at young, middle, and old ages to measure the effect of age on the ability of skeletal muscle mitochondria to adapt to this insult in vivo. In an effort to understand the mechanistic basis for our results we go on to use uncoupling protein 3 (UCP3) knock-out mice to determine whether the activation of UCP3 mediated proton leak is responsible for ROS-induced uncoupling in vivo.

Methods

Animals

This study was approved by the Institutional Animal Care and Use Committee of the University of Washington. For aging studies, female C57BL/6 mice were purchased from the aged mouse colony maintained by NIA at Charles River Laboratories (Wilmington, MA). Female UCP3$^{-/-}$ mice on a C57BL/6J background were studied between 4 and 7 months of age (58). All mice were kept on a 12 hour light/dark cycle at 22°C and 20% humidity with free access to water and standard mouse chow until immediately prior to experimentation. Mouse body temperatures were maintained by forced air at 36°C ± 1°C throughout in vivo experiments.

Paraquat

Paraquat (Item 36541, Sigma, St. Louis, MO) was dissolved in 0.9% filtered saline at a concentration of 1mg/mL and administered by intraperitoneal injection. Mice received either 20mg PQ per kg of body weight or volume matched saline on the evening prior to in vivo experiments.

Multi-Modal Spectroscopy

Mice were anesthetized by intraperitoneal injection of 0.01ml/g of 2.5% tribromoethanol ("Avertin", Sigma) and the left distal hindlimb shaved using veterinary hair clippers. As illustrated in Fig. 4.1, mice were then suspended using Velcro straps in a custom built MR/optics probe. We developed custom probes for use with either 7T (Oxford Instruments, Oxford, UK) or 14T (Bruker, Billerica, MA) vertical bore magnets. Both probes employed the same general design: the distal hindlimb is centered within a horizontal, solenoid MR coil tunable to both ^{1}H and ^{31}P with the foot fixed against a plastic post. Aligned fiber optic bundles are positioned on either side of the coil (perpendicular to the coil axis), to deliver light from a QTH source (Newport Corp, Irvine, CA) to the lateral surface of the hindlimb, collect light transmitted through the hindlimb, and deliver this transmitted light to a spectrograph coupled to a CCD camera (Princeton Instruments, Trenton, NJ).

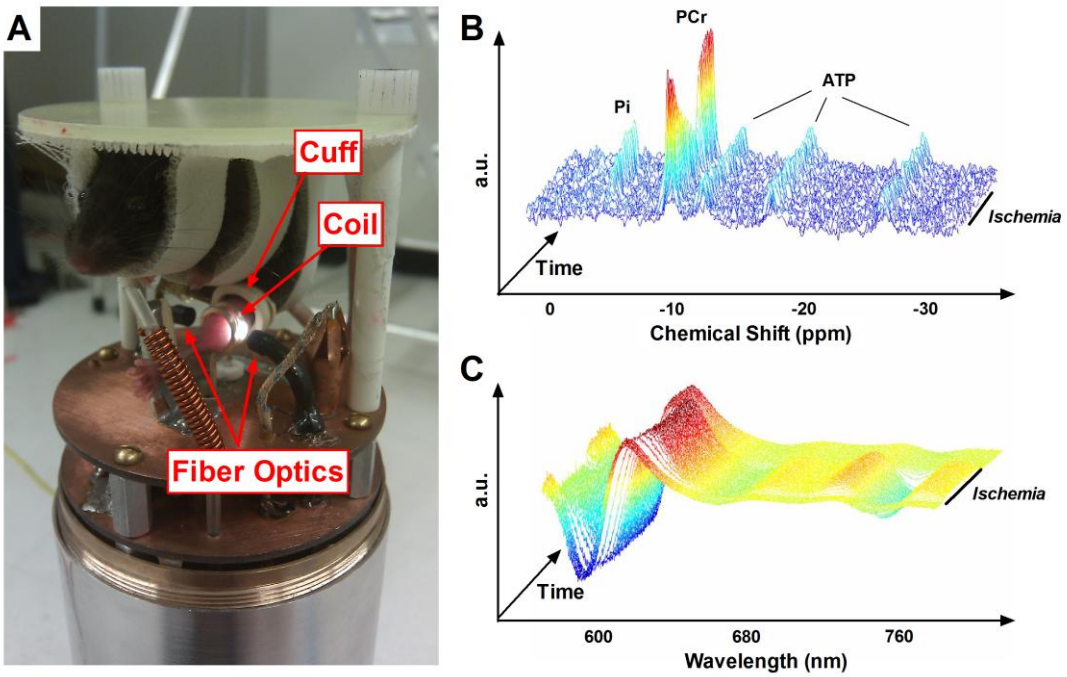

Figure 4.1. (A) Photograph of the combined MR and optical spectroscopy probe for use with the Bruker 14T spectrometer. An anesthetized mouse is suspended above spectroscopy hardware, with its shaved distal hindlimb positioned in the center of an MR coil tunable to both ^{1}H and ^{31}P, flanked on either side by fiber optic bundles. An inflatable ischemia cuff surrounds the hindlimb proximal to the MR coil. Unlabeled components visible in the picture include a 100% oxygen delivery line, thermocouple, and warm air delivery port. (B) Representative ^{31}P MR spectra (after exponential multiplication, Fourier transformation, and summing 5 consecutive spectra), stacked through the course of a dynamic in vivo experiment. During ischemia, PCr is broken down to maintain constant ATP as the resting energy demands of the cell are met and P_i undergoes a stoichiometric increase. (C) Representative optical spectra (after taking second-derivative) during a dynamic in vivo experiment. As Hb and Mb deoxygenate during ischemia, a pronounced rightward shift is evident between ~580 and 660nm and a dramatic sinusoidal feature becomes prominent at ~760nm.

After positioning the mouse, MR signal was optimized by shimming the ^{1}H peak using tissue water and optical signal was optimized by adjusting acquisition time (typically 30-60msec). A high signal to noise ^{31}P spectrum was acquired under fully relaxed conditions (32 transients, 4096 complex points,10kHz sweep width, 25sec interpulse delay at 7T; 80 transients, 8192 complex points, 20kHz sweep width, 10s interpulse delay at 14T). Dynamic optical (0.5sec delay) and MR spectra (45° flip angle, 4 transients , 4096 complex points, 10kHz sweep width, 1.5sec interpulse delay, at 7T; 45° flip angle, 4 transients, 4096 complex points, 20kHz sweep width, 0.6sec interpulse delay at 14T) were acquired continuously through periods of rest (2min), ischemia (11min), and recovery (7min). After the first minute of rest mice breathed 100% oxygen for the remainder of each experiment. Experiment timing is summarized in Fig. 4.2. Flux rates and metabolite concentrations acquired on 7T and 14T systems were not different.

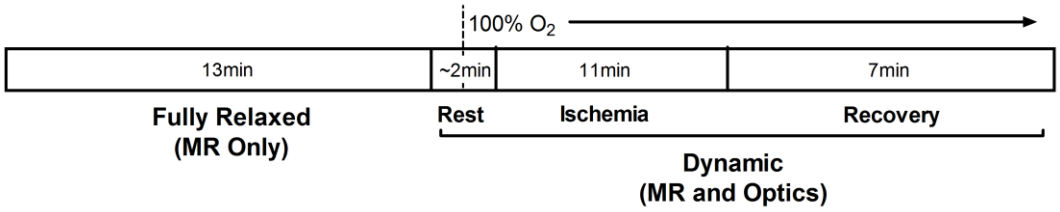

Figure 4.2. Rest-ischemia-recovery protocol, corresponding with description in *Methods*.

Tissue Preparation

Immediately following in vivo spectroscopy, mice were injected with a supplemental, non-lethal dose of Avertin and the skeletal muscles of the distal hindlimb were dissected and flash-frozen in liquid nitrogen. From the left leg, extensor digitorum longus, gastrocnemius, soleus, and tibialis anterior muscles were pooled and pulverized over liquid nitrogen for measurement of mixed muscle metabolite, hemoglobin (Hb), and myoglobin (Mb) concentrations. From the right leg, gastrocnemius was pulverized over liquid nitrogen and prepared for western blotting. All muscle samples were stored at -80^{o} until the day of assay.

Metabolite Concentrations

Tissue concentrations of ATP, phosphocreatine (PCr), and creatine were determined in mixed muscle by HPLC (Waters, Milford, MA) using the protocol described in detail in Chapter 3.

Protein Content

Absolute Hb and Mb concentrations were determined using Coomassie-staining with in-gel standards of known concentration. Aliquots of pulverized mixed muscle were combined 1:25 with Cellytic MT lysis buffer (Sigma #C3228) containing 0.1% protease inhibitor (Sigma #P8340), and homogenized at 4°C using a Bullet Blender 24 (Next Advance, Averill Park, NY). The resulting lysate was combined 1:1 with tricine sample buffer (Bio-Rad #161-0739) containing 350mM DTT and brought to 95°C for 8 minutes. Proteins were separated on 10-20% gradient gels at 150V for 2.5 hours and then stained overnight in Coomassie Brilliant Blue stain (Bio-Rad). After destaining, gels were imaged using the Bio-Rad ChemiDoc imaging system and band intensities were analyzed using QuantityOne software (Bio-Rad).

All other protein analyses were accomplished using western blotting. Aliquots of pulverized gastrocnemius were combined 1:25 with lysis buffer containing 0.1% protease inhibitor (same as above) plus 1% phosphatase inhibitor (Thermo Scientific #78420), and homogenized at 4°C using a Bullet Blender 24. The resulting lysate was combined 1:1 with Laemmli sample buffer (Bio-Rad #161-0737) containing 350mM DTT and proteins were separated on 4-20% gradient gels at 200V for 65-75 minutes. Proteins were transferred to nitrocellulose membranes, Ponceau stained to ensure uniform transfer and loading, and then immunoblotted as follows (block, primary, secondary): UCP3 (3%BSA 1hr at RT, 1:1K Abcam #3477 overnight at 4°C, 1:10K Cell Signaling #7074 2hr at RT), ANT1 (5%BSA overnight at 4°C, 1:1K Sigma #SAB2105530 2hr at RT, 1:5K Cell Signaling #7074 2hr at RT), phospho-AMPK (3%BSA 1hr at RT, 1:1K Cell Signaling #2535 overnight at 4°C, 1:10K Cell Signaling #7074 2hr at RT), AMPK (3%BSA 1hr at RT, 1:1K Cell Signaling #2532 overnight at 4°C, 1:10K Cell Signaling #7074 2hr at RT), ETC complexes I-V (3%BSA 1hr at RT, 1:1K MitoSciences #604 overnight at 4°C, 1:10K Cell

Signaling #7076), HNE (5%NFDM 1hr at RT, 1:1K Alpha Diagnostics #HNE12s, 1:2K Alpha Diagnostics #30220). All antibodies were diluted in 1%BSA, except HNE for which 1%NFDM was used, and all solutions were made in 0.1% TTBS. When possible, α-tubulin (1:1K Cell Signaling #2125) was probed simultaneously as a loading control. When α-tubulin could not be probed reliably, Bradford assays were used to determine volume of total loaded protein. Membranes were developed using Immun-Star Western C Chemiluminescence Kits (Bio-Rad), imaged using a ChemiDoc imaging system, and band densities measured using QuantiyOne.

Multi-Modal Spectroscopy Data Analysis

^{31}P MR spectra were exponentially multiplied (20Hz at 7T, 40Hz at 14T), Fourier transformed, and manually phase corrected using Varian VNMR (7T) or Bruker TopSpin (14T) software. The resulting spectra were taken to custom written MATLAB software (Mathworks, Natick, MA) for the remainder of analysis. Raw optical spectra files collected using WinSpec (Princeton Instruments) were taken directly to custom written MATLAB software for analysis.

The method used for analyzing MR spectra is described in detail elsewhere (105). Relative peak integrals from fully relaxed ^{31}P MR spectra were used to calculate the resting inorganic phosphate (P_i) /ATP and PCr/ATP ratios. After summing 3 consecutive dynamic spectra to improve signal-to-noise ratio, we used the Fit-to-Standard algorithm (70) to determine PCr and P_i peak magnitudes throughout dynamic acquisition, relative to rest. Then, after correcting for variable relaxation, the ATP concentration from HPLC analysis of mixed muscle was used as an internal reference to calculate absolute PCr and P_i concentrations over time. pH was determined using the chemical shift between P_i and PCr peaks, and ADP and AMP concentrations were calculated using the known kinetics of the creatine kinase and adenylate kinase reactions, assuming equilibrium conditions and a Mg^{2+} concentration of 0.6mM (56, 91, 174).

The method used for analyzing optical spectra has been described in detail previously (105). After taking the second-derivative of optical spectra to minimize the influence of tissue scattering, we used a partial-least squares routine to determine the oxygen saturations of Hb and Mb throughout dynamic spectral acquisition (10). The concentrations and known oxygen binding kinetics of Hb and Mb were then used to calculate net oxygen flux in the closed system of the ischemic hindlimb.

The resting rates of mitochondrial ATP production (ATPase) and oxygen consumption were calculated during ischemia from least-squares linear approximations of the decline in PCr and oxygen, respectively, during the initial phase of ischemia. Using the initial phase of ischemia allows the ATPase and oxygen consumption rates to be determined before the onset a significant glycolytic contribution to PCr synthesis and before oxygen tension became rate-limiting to oxidative phosphorylation, respectively. The maximum rate of oxidative phosphorylation (ATPmax) was calculated using a least-squares monoexponential approximation of PCr recovery during recovery from ischemia (16), beginning from the time at which a least-squares hyperbolic fit of Mb oxygen saturation had recovered to 50%.

T2 Imaging

Mice were anesthetized by IP injection of Avertin and then placed in the prone position within a custom-built imaging probe with both distal hindlimbs extended backward and positioned within a 25mm ^{1}H volume coil (Litzcage 25mm ID, Doty Scientific, Columbia, SC). An inflatable ischemia cuff was positioned around the right hindlimb, proximal to the volume coil. The probe was then positioned within a 30cm horizontal-bore 4.7T magnet (Bruker) with a Varian console, equipped with a 100mT/m imaging gradient (BGA-20-S2, Bruker). After shimming to optimize signal quality, ischemia was induced in the right hindlimb, and T2 was mapped across both hindlimbs simultaneously using a 2mm thick, 30mmx30mm cross-section and a standard spin echo sequence with TEs of 14.2, 27.6, 41.4, 54.5, and 67.5msec. Mouse body temperatures were maintained using a custom-integrated heating system that

passed 42°C water through the imaging probe. Average T2 values across the each hindlimb were calculated in ImageJ using the MRIAnalysisPak plug-in.

Statistics

Statistical analysis was carried out using Prism 5 software (GraphPad, La Jolla, CA). Based on a priori hypotheses for measurements of energetic parameters, one-tailed student's t-tests were used to compare PQ-treatment vs. control at every age and middle aged and old controls vs. young controls. Two-tailed student's t-tests were used for analyses of protein expression data. t-tests were chosen over analysis of all age groups with linear regression because it makes fewer assumptions and provides unambiguous comparisons. The boundary for statistical significance was set at $p = 0.05$.

Results

Multi-modal spectroscopy is a novel method for measuring in vivo energetics

To measure in vivo mitochondrial metabolism in mouse skeletal muscle during a single experiment we used a novel combined MR and optical spectroscopy system. As illustrated in Fig. 4.1A, the distal hindlimb of an anesthetized mouse is passed through an inflatable ischemia cuff and positioned in the center of a horizontal MR coil, which is flanked on either side by fiber optic bundles. We use this setup to simultaneously collect NIR optical spectra and ^{31}P-MR spectra during periods of rest, a brief bout of ischemia, and recovery (Fig. 4.2). The changes in MR and optical spectra during this protocol are illustrated in Figs. 4.1B and 4.1C, respectively. As described previously, optical spectra can be used to measure the rate at which oxygen is consumed as the terminal electron acceptor of oxidative phosphorylation (105), and ^{31}P-MR spectra can be used to quantify the rate of mitochondrial ATP production (16).

By acquiring MR and optical spectra simultaneously we are able to measure acute metabolic changes in vivo and to make time-resolved comparisons between the oxygen saturations of Hb and Mb, phosphometabolite concentrations, and pH (illustrated and discussed in Fig. 4.3).

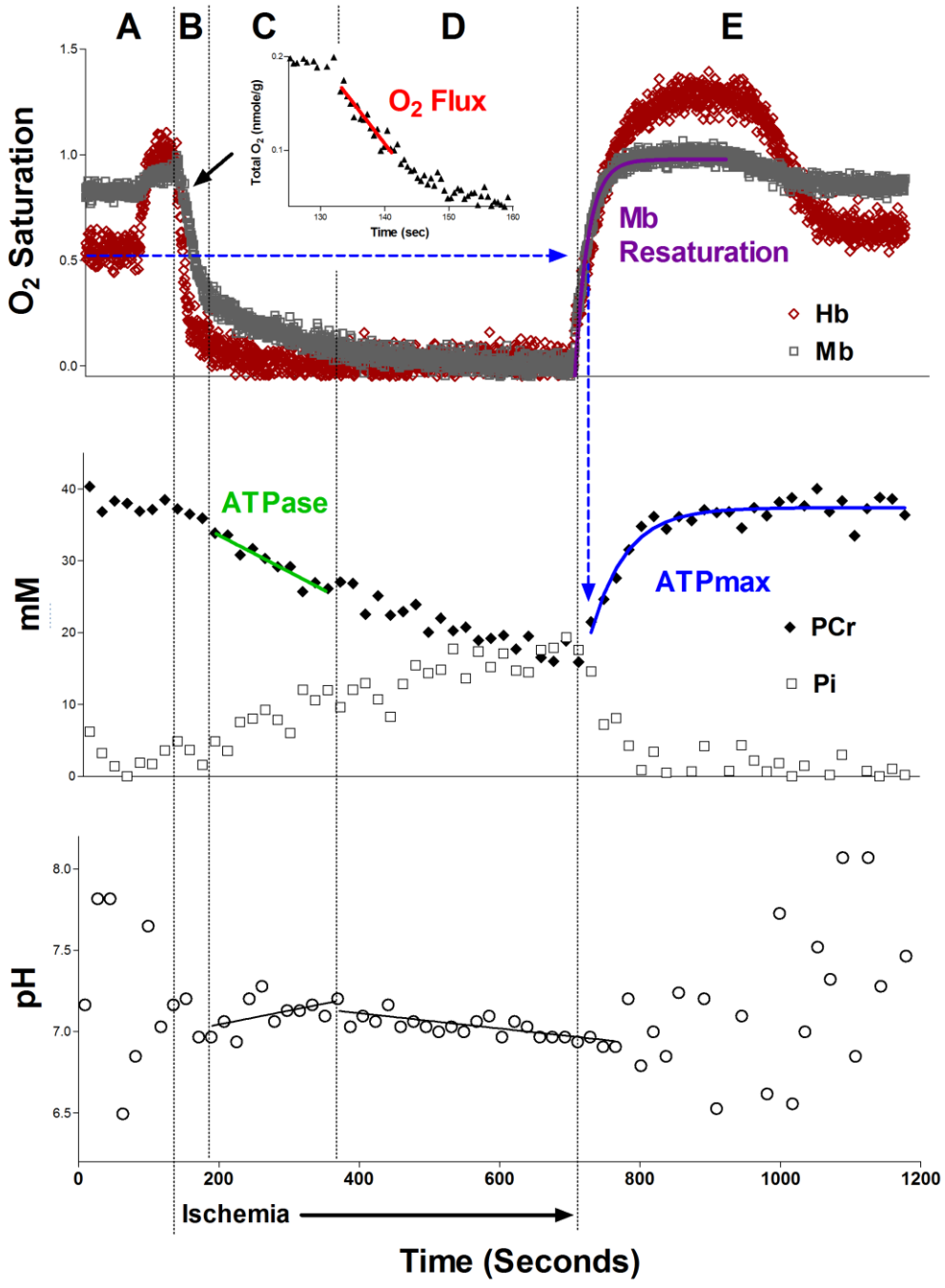

Figure 4.3 (caption on next page)

Figure 4.3. Representative time-course of Hb and Mb saturations (top), PCr and P_i concentrations (middle), and pH (bottom) following analysis of in vivo spectroscopy data. Distinct time-separated regions are identified by letters at the top and summarized as follows: (A) During an initial period of rest, delivery of 100% O_2 induces distinct increases in the O_2 saturations of Mb and Hb as both proteins reach nearly complete saturation. During rest, PCr remains constant while oxidative phosphorylation meets ATP demand, and P_i is generally too low to overcome signal-to-noise limitations in mouse skeletal muscle. As a result pH measurements are not reliable during this time. (B) After inflating the ischemia cuff, O_2 that is bound to Hb and Mb in the now-closed system of the distal hindlimb is used to fuel oxidative phosphorylation for a short period of time. Thus, the rate of mitochondrial O_2 consumption ("O_2 Flux" in graph inset) can be measured using the rates of Hb and Mb desaturation. PCr and P_i remain constant during this time and pH measurements remain somewhat unreliable. (C) When intracellular O_2 tension becomes low enough to limit the rate of oxidative phosphorylation, PCr is broken down to meet resting ATP demand ("ATPase"). This is evident as linear changes in PCr (decrease) and P_i (increase), and a period of alkalinization accounted for by the proton stoichiometry of PCr hydrolysis (104). (D) As ischemia continues for up to 11 minutes, Hb and Mb become entirely deoxygenated. The rates of change of PCr and P_i slow down due to activation of glycolysis, which contributes to PCr synthesis. Due to this glycolytic activity, acidification is clear in a plot of pH vs. time. (E) Upon deflation of the ischemia cuff, muscle is reperfused leading to rapid recoveries of Hb and Mb saturations. PLS analysis of Mb saturation remains reliable during recovery, however measurement of Hb saturation become unreliable at this point due to simultaneous changes in both Hb saturation and concentration. The rate of Mb resaturation can thus be used as a measure of the relative rate of muscle reperfusion. By measuring the monoexponential time constant of PCr recovery from the time at which Mb has recovered to 50%, illustrated by blue dashed arrows, the maximal rate oxidative phosphorylation (ATPmax) is measured. P_i decreases back to resting levels and pH is no longer reliable.

Aged mitochondria uncouple in response to oxidative insult despite pre-existing inefficiency.

We used in vivo spectroscopy to measure the efficiency of mitochondrial oxidative phosphorylation (ATP produced per oxygen atom consumed; P/O ratio) in young (5-7 months), middle aged (21-22 months), and old (27-28 months) C57BL/6 mice with a published median lifespan of 26 months (177). To test the hypothesis that ROS-induced uncoupling is diminished with age, mice received IP injections of either 20mg/kg PQ or volume-matched saline (C) one day prior to in vivo spectroscopy. PQ is a redox-cycling agent that increases both mitochondrial and cytosolic superoxide production (32). This low dose of PQ was chosen well below the LD50 of 70mg/kg to induce an acute period of mildly elevated ROS production (42). The mild nature of the PQ-induced oxidative insult was confirmed as an age, but not PQ, related increase of 4-hydroxynonenal (HNE) protein adducts in gastrocnemius muscle (Fig. 4.4).

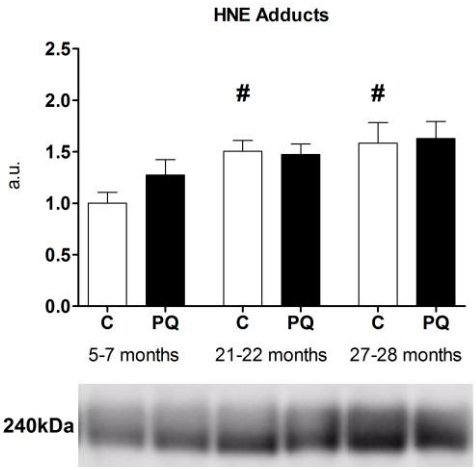

Figure 4.4. HNE adducts on high molecular weight proteins increased with age but were unaffected by PQ-treatment. Band densities normalized to total loaded protein and presented relative to young control average. Data presented as mean±SEM, n = 4, #p < 0.05 relative to young control.

Consistent with previous reports in mice and humans (4, 106), P/O ratio declined with age. Despite this age-related loss of mitochondrial efficiency, P/O decreased in response to PQ treatment at all 3 ages (Fig. 4.5A). In all cases, a significant decrease in ATPase rate (i.e. resting ATP demand) with insignificant trends toward faster oxygen consumption (Figs. 4.5B and 4.5C) was responsible for decreases in P/O. The relative magnitude of ROS-induced uncoupling was not lost with age (34% for young, 22% for middle aged, and 34% for old), despite the significantly lower resting P/O in aged mice. As a result the P/O ratio in old PQ-treated mice was 50% lower than that of young controls.

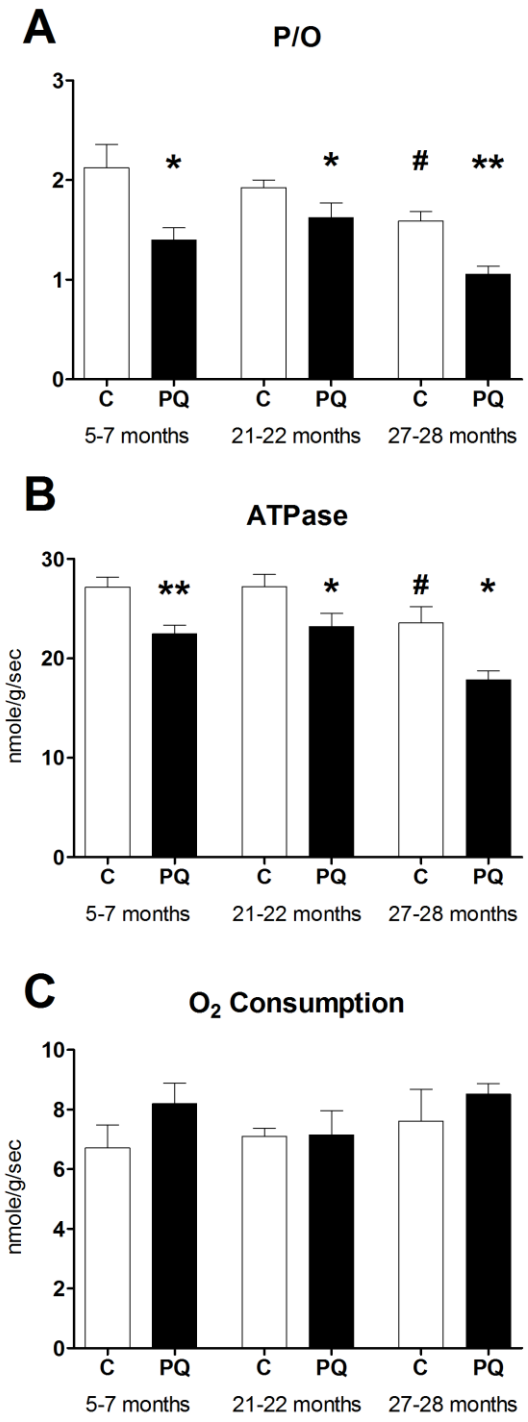

Figure 4.5. (A) In vivo P/O ratio decreases following acute PQ-treatment in young, middle-age, and old mice. Reduced P/O is associated with reduced resting ATPase rate (B) without significant changes in mitochondrial O_2 consumption following PQ treatment (C). The same trend led to a significant decrease in P/O of old relative to young control mice. Data presented as mean ± SEM, n = 4-8, * $p < 0.05$, **$p<0.01$ relative to age-matched control, #$p<0.05$ relative to young control.

ROS-induced uncoupling is independent of UCP3 in vivo

To test the hypothesis that activation of proton leak through UCP3 was responsible for the decreases in P/O ratio that we observed, we first measured UCP3 protein content in gastrocnemius from mice in all six age/treatment groups. Confirming previous results, UCP3 protein expression decreased significantly with age (86) and was unaffected by PQ treatment (158) (Fig. 4.6A), suggesting that the magnitude of uncoupling was unaffected by UCP3 protein levels. Protein expression of another putative uncoupler of oxidative phosphorylation in skeletal muscle, ANT1, was not different with age or PQ-treatment (Fig. 4.6B).

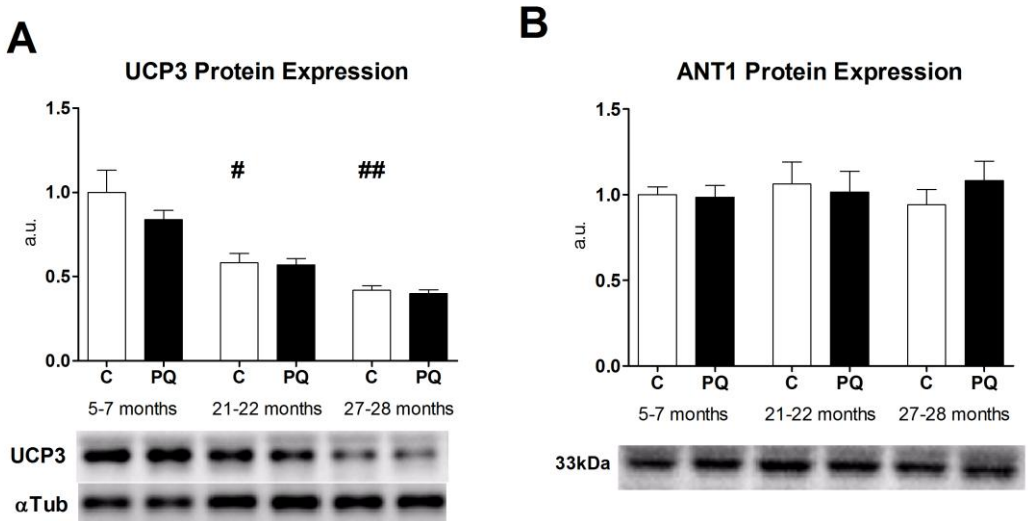

Figure 4.6. (A)UCP3 protein expression decreases with age, but is unaltered with PQ-treatment, in mixed gastrocnemius. (B) ANT1 protein expression was unaffected by either age or PQ-treatment. UCP3 band densities were normalized to α-tubulin and ANT1 normalized to total loaded protein. All values presented relative to young control average as mean ± SEM, n = 4, #p<0.05, ##p<0.01 relative to young control.

To further test the role of UCP3 in ROS-induced uncoupling, we measured the effects of PQ treatment on in vivo P/O ratio in young UCP3$^{-/-}$ mice. PQ-treatment induced a significant drop in P/O ratio in UCP3$^{-/-}$ mice of the same magnitude observed in wild-type mice used for the aging experiments (mean difference of 29%, Fig. 4.7). The absence of UCP3 protein was verified in mixed skeletal muscle of UCP3$^{-/-}$ mice by western blot (Fig. 4.8).

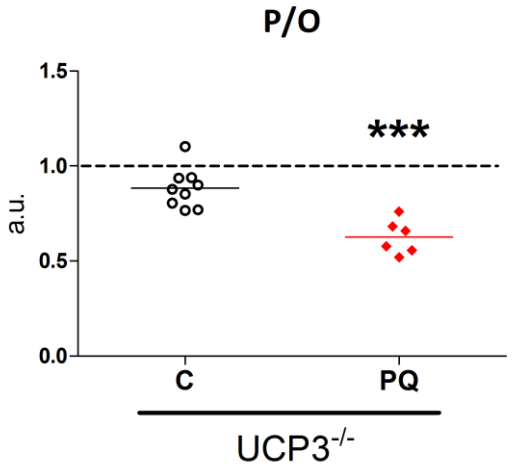

Figure 4.7. PQ-treatment leads to reduced coupling of oxidative phosphorylation (decreased P/O) in young adult $UCP3^{-/-}$ mice. Values presented as fraction of P/O ratio in untreated $UCP^{+/+}$ littermates. Lines represent means. n = 6-9, *** $p < 0.001$. Dashed line represents average P/O for untreated $UCP3^{+/+}$ littermates.

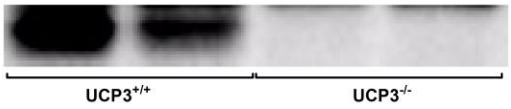

Figure 4.8. Western analysis to verify the presence or absence of UCP3 protein in mixed skeletal muscle of $UCP3^{+/+}$ or $UCP3^{-/-}$ mice, respectively. UCP3 is located at approximately 34kDa, just below a commonly observed nonspecific band at ~37kDa.

Old mice respond to acute oxidative insult with unique changes in phosphorylation capacity

The rate of recovery of PCr from ischemia provides a measure of the maximum rate of oxidative phosphorylation (ATPmax, Fig. 4.3) (16). Using the monoexponential time constant of PCr recovery from the time at which a hyperbolic fit of Mb saturation recovered to 50% we eliminated a significant dependence of PCr recovery kinetics upon the rate of muscle reperfusion (Fig. 4.9).

In old mice, ATPmax was approximately 30% lower than young controls and declined even further with PQ treatment (Fig. 4.10A). In contrast, ATPmax was not affected by age or PQ treatment in young and middle aged mice.

Using western blot analysis of mixed gastrocnemius, we tested the hypothesis that the decreases in ATPmax were due to reduced expression of ETC proteins. Protein expression of ETC complexes I-V increased significantly with age and we observed no significant effect of PQ (Fig. 4.11).

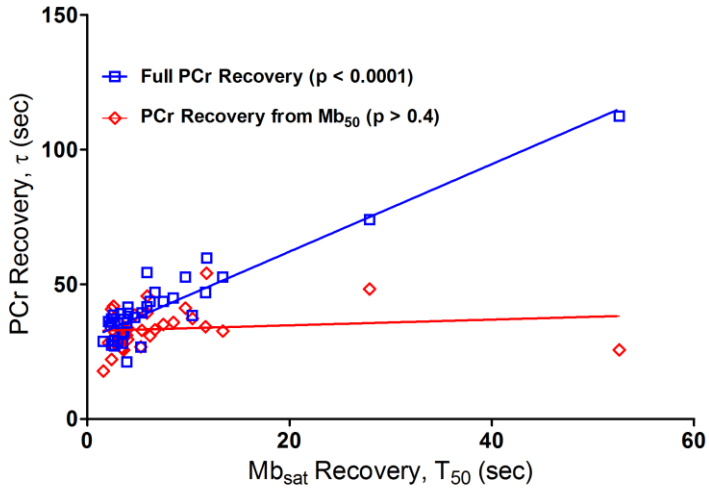

Figure 4.9. The dependence of PCr recovery (monoexponential time constant, τ) upon the rate of muscle reperfusion as measured by the rate of Mb resaturation (hyperbolic T_{50}) was eliminated by measuring PCr recovery from the time at which Mb has resaturated to 50%. Data points pooled from all age/treatment groups and p-values represent the results of linear regression analysis.

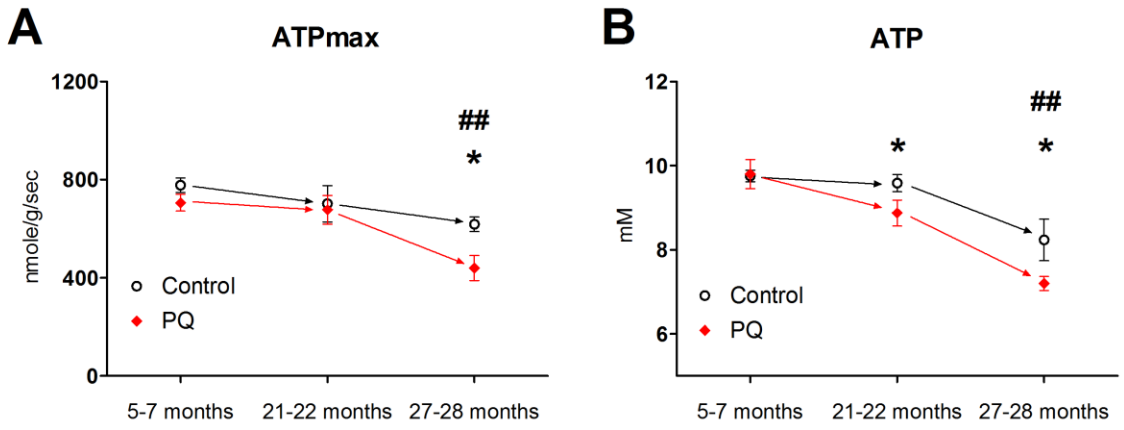

Figure 4.10. (A) ATPmax was significantly lower in old controls and PQ treatment led to a significant decline in ATPmax in old mice only. (B) ATP concentration in skeletal muscle decreased significantly in old compared to young controls, and PQ treatment led to significant decreases in ATP in both middle aged and old mice. Data presented as mean ± SEM, n = 4-8, *p<0.05 PQ-treatment vs. age-matched control, ## p<0.01 aged control vs. young control.

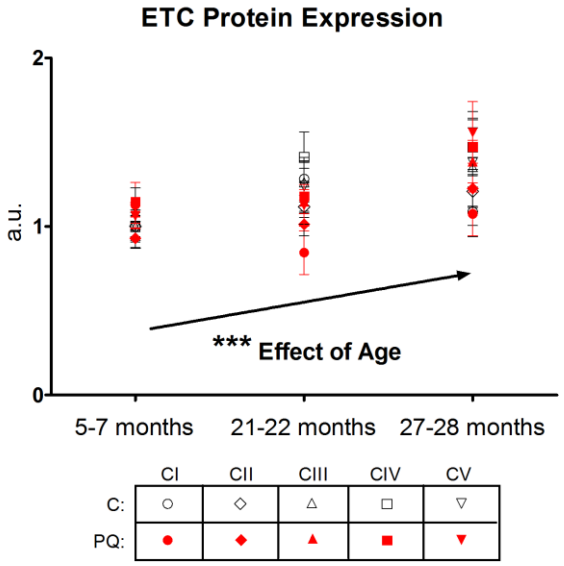

Figure 4.11. Protein expression of complexes I-V of the ETC increased significantly with age in mixed gastrocnemius but was unaffected by PQ-treatment. Band densities are normalized to total loaded protein and presented relative to young control average for each complex separately. Data presented as mean ± SEM, n = 4, ***p< 0.001 as measured using two-way ANOVA across all complexes.

Acute oxidative insult disrupts energy homeostasis in aged mice

We measured metabolite concentrations in resting skeletal muscle to determine the effects of changes in mitochondrial function on muscle energetics in vivo (Table 4.1). As depicted in Fig. 4.10B, ATP concentration was unaffected by PQ-treatment in young mice and was maintained in middle aged controls. However, ATP was significantly lower in old mice and decreased in response to PQ treatment in both middle aged and old mice.

Additional unique energetics changes were detected with age and PQ-treatment. In PQ-treated young and middle-age mice PCr/ATP ratio decreased and AMP/ATP increased, indicative of energetic stress associated with decreased P/O. In old mice, however, PCr/ATP and AMP/ATP ratios were insensitive to PQ treatment (Table 4.1). Using western blot analysis we detected increased phosphorylation of AMPK in gastrocnemius of young PQ-treated mice, but this response was absent at other ages (Fig. 4.12).

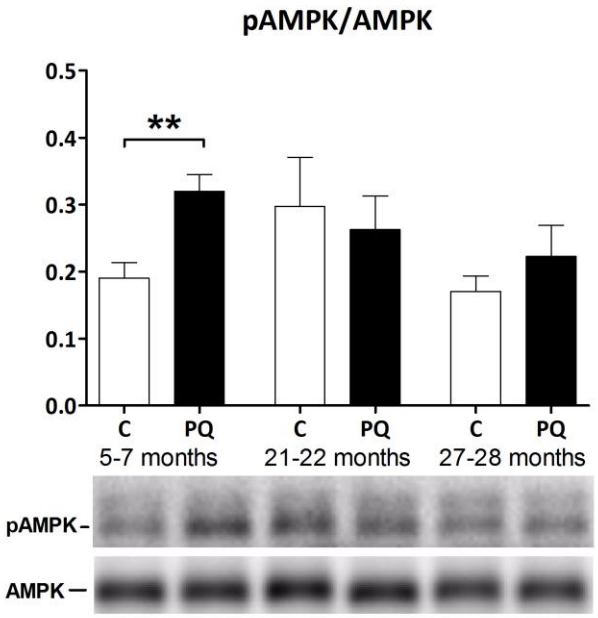

Figure 4.12. Phosphorylation ratio of the energy sensitive kinase AMPK increased with PQ-treatment in gastrocnemius of young but not old mice. Band densities were normalized to α-tubulin loading control and ratios are presented relative to young control average. Representative images are taken from separate portions of the same membrane. Data presented as mean ± SEM, n = 4, ** $p < 0.01$ relative to age-matched control.

The role of oxidative stress in the energetic consequences of ROS-induced uncoupling

To test whether the energetic differences that we observed with ROS-induced uncoupling in aged mice were due to compounded oxidative stress typical of old skeletal muscle (96), we varied the PQ dose in young mice between 0 and 30mg/kg per single IP injection and measured in vivo energetics one day later. We hypothesized that, if oxidative stress were the cause of energetic inflexibility in old mice, then a high enough PQ dose in a young mouse would mimic the entire suite of energetic and downstream signaling changes that we observed with age. Confirmation of this hypothesis would suggest that interference of oxidative stress (or oxidative byproducts) with components of the energetic cascade (i.e. coupling of oxidative phosphorylation → energy state → signaling to maintain energy homeostasis) is the mechanism responsible for the loss of energetic plasticity during ROS-induced uncoupling in aged mice. Results from this portion of the study are summarized in Fig. 4.13.

As illustrated by differences in P/O ratio in Fig. 4.13A, a similar degree of ROS-induced uncoupling occurred in mice regardless of PQ dose. PCr/ATP ratio decreased and AMP/ATP ratio increased in

association with these changes in P/O up to a dose of 20mg/kg PQ, but the trend was discontinued at 30mg/kg. At this dose, PCr/ATP and AMP/ATP ratios trended back towards values measured in untreated mice (Fig. 4.13B and 4.13C).

In line with these changes in phosphometabolite concentrations, the phosphorylation ratio of AMPK increased in a dose-dependent manner up to a dose of 20mg/kg PQ, at which point an apparent plateau was reached and no further activation of this energy sensing kinase was observed at 30mg/kg (Fig 4.13D). ATPmax was maintained at PQ doses of 10 and 20mg/kg but decreased significantly at a dose of 30mg/kg, while total ATP concentrations were the same regardless of PQ dose (Figs. 4.13E and 4.13F, respectively).

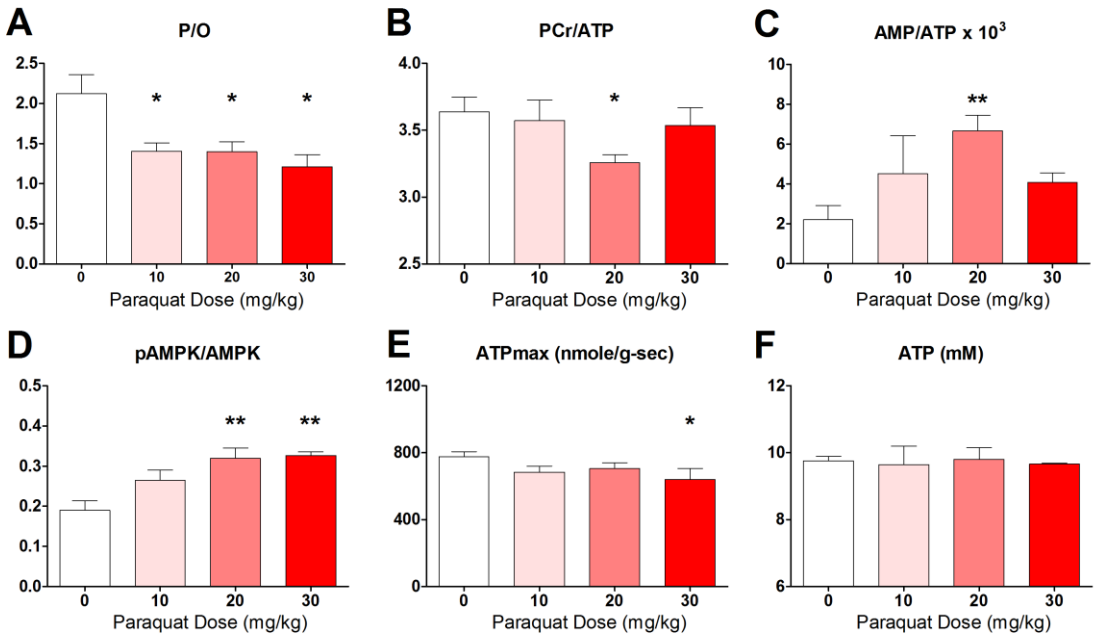

Figure 4.13. (A) In vivo P/O ratio declined to a similar degree in young mice, regardless of dose response, however (B) PCr/ATP ratio decreased and (C) AMP/ATP ratio increased in association with changes in P/O only up to a dose of 20mg/kg PQ. (D) Phosphorylation ratio of AMPK increased with PQ dose but appeared to level off at a dose of 20mg/kg PQ. (E) ATPmax was only lower in mice that received 30mg/kg PQ and (F) ATP concentrations were unaffected by PQ. Data presented as mean ± SEM, n = 3-5, *p<0.05, ** p< 0.01 relative to 0mg/kg PQ dose.

Changes in metabolite concentration are not due to differences in fluid distribution

Due to our biochemical approach for measuring ATP and other metabolites in a mixed muscle sample taken after in vivo spectroscopy, an assumption must be made regarding the intracellular water volume when calculating intracellular metabolite concentration. Therefore, to address the concern that variation in intracellular water fraction may be the source of our calculated differences in ATP concentration, we measured T2 relaxation times in the distal hindlimbs of young and old mice under resting and ischemic conditions. Representative T2-weighted images (Fig. 4.14) illustrate similar levels of homogeneity within skeletal muscle of young and old mice.

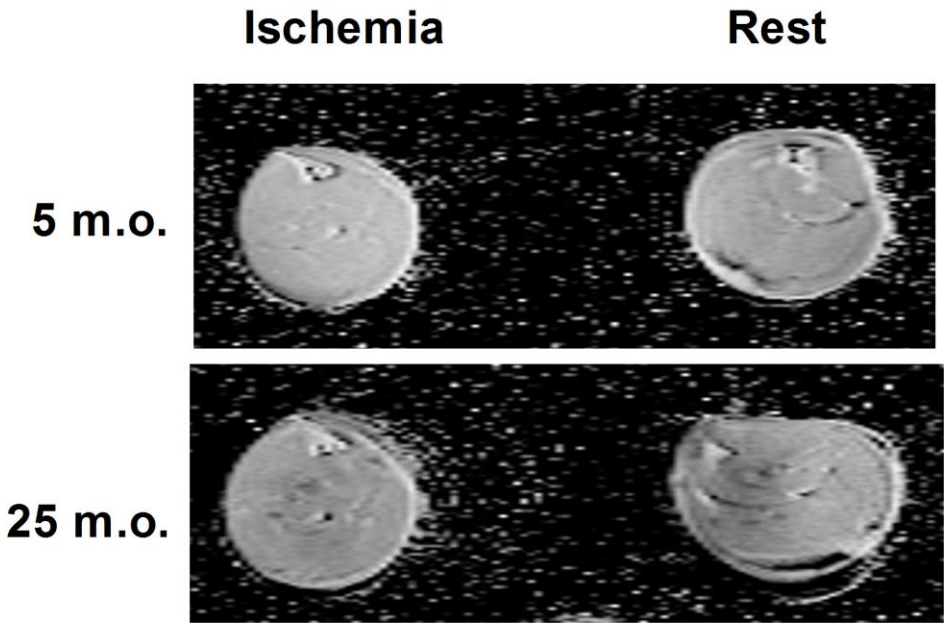

Figure 4.14. Representative T2-weighted images collected from the distal hindlimbs of young (5m.o.) and old (25m.o.) mice. A cuff was used to induce ischemia in the right leg (images on the left) while images were acquired from both legs simultaneously.

At rest, average T2 relaxation times for the cross-section of the distal hindlimb were not significantly different between young and old mice, though values in the young tended to be slightly slower (i.e. higher T2, Fig. 4.15A). Under ischemic conditions, T2 relaxation times were in better agreement between young and old (Fig. 4.15B).

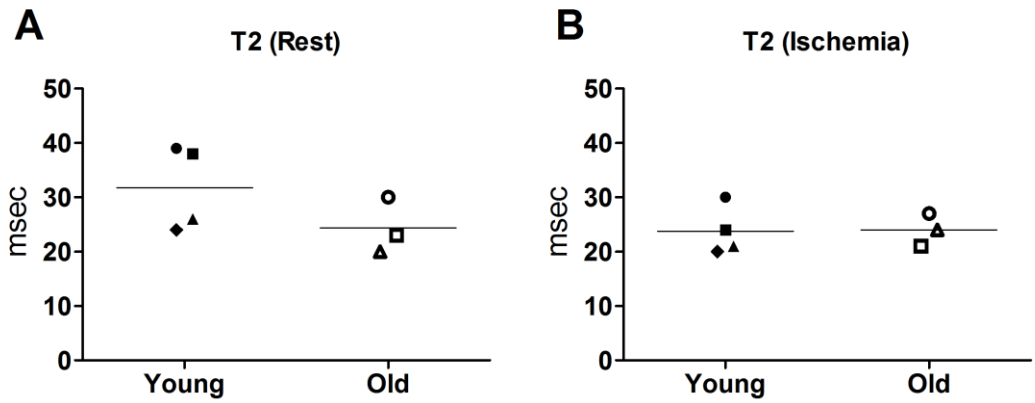

Figure 4.15. (A) Under resting conditions, average T2 values were not significantly different, however, T2 tended to relax more slowly in young skeletal muscle. (B) Under ischemic conditions there was no difference between young and old T2 relaxation. Symbol shapes in A and B align data collected from opposite legs of the same mouse. Lines represent group means.

Table 4.1. Table of relevant in vivo metabolite concentrations in mixed skeletal muscle. ATP and total creatine (Cr) were determined using HPLC and the remaining values were calculated using in vivo MR spectra. Data presented as mean ± SEM, n = 4-8, *p < 0.05, **p<0.01 relative to age-matched control. #p < 0.05, ##p<0.01, ###p<0.001 relative to young control.

	5-7 Months		21-22 Months		27-28 Months		UCP3$^{-/-}$	
	C	**PQ**	**C**	**PQ**	**C**	**PQ**	**C**	**PQ**
ATP(mM)	9.76±0.14	9.81±0.35	9.59±0.20	8.87±0.31*	8.23±0.50##	7.20±0.17*	9.67±0.29	9.28±0.37
PCr(mM)	35.48±1.05	31.97±1.48*	33.86±1.10	27.70±0.95**	29.26±0.76###	24.93±1.13**	33.61±1.29	30.67±2.09
Total Cr(mM)	42.3±0.45	43.01±1.11	43.45±1.44	40.39±1.54	39.33±1.25#	37.28±0.84	40.69±0.81	40.28±0.62
PCr/ATP	3.64±0.11	3.26±0.06*	3.53±0.08	3.13±0.09**	3.57±0.09	3.46±0.13	3.48±0.09	3.29±0.13
ADP(μM)	14.4±2.6	26.4±1.1**	23.7±3.8	38.9±4.5*	31.4±4.0##	27.1±5.8	17.1±2.9	26.0±6.1
AMP(μM)	21.6±6.7	64.8±6.0**	62.8±20.9	161.7±30.5**	110.5±21.3**	105.7±41.4	34.2±11.2	92.2±41.8
AMP/ATP x10^3	2.21±0.70	6.67±0.77**	6.59±2.2	18.1±3.3**	13.1±1.9###	14.9±6.0	3.6±1.2	11.0±5.6
pH$_{Rest}$	7.02±0.01	7.04±0.03	7.09±0.02	7.12±0.02	7.11±0.03#	6.97±0.02**	7.06±0.02	7.08±0.03
pH$_{Ischemia}$	6.94±0.01	6.92±0.02	6.95±0.01	6.92±0.01*	6.97±0.01#	6.93±0.01	6.96±0.03	6.93±0.04

Discussion

This study tests whether the ability of mitochondria to functionally adapt to an acute oxidative insult is affected by age. Contrary to our initial hypothesis, ROS-induced uncoupling persisted between the ages of 5 and 28 months in mouse skeletal muscle. Interestingly, this insult resulted in deficits in mitochondrial ATPmax and ATP concentration in old mice only. These results provide novel insight into the effects of acute oxidative insult on metabolic function throughout life and reveal reduced adaptability of aged mitochondria to mild physiological stress. Furthermore, we provide in vivo evidence that this ROS-induced uncoupling is a UCP3-independent mechanism.

Methodology

MR (51, 79, 85, 94) and optical (10, 118, 153) spectroscopy are powerful methods for measuring tissue energetics and oxygenation state. Due to the interaction between tissue oxygenation state and mitochondrial energetics it is important to measure both parameters to understand the effects of a perturbation on skeletal muscle metabolism. Lanza, et al., for example, used dynamic, interleaved acquisition of ^{1}H and ^{31}P MR spectra to simultaneously measure Mb saturation and phosphometabolite flux in human tibialis anterior muscle to determine the oxygen tension at which ATP synthesis during contraction was limited by oxygen availability (94). Previously published work has also demonstrated the viability of using separately acquired MR and optical spectra during bouts of rest, ischemia, and recovery to measure skeletal muscle energetics in humans (3) and mice (105). In the current study we present the extension of this methodology to an integrated MR and optical spectroscopy system for use with mouse models of disease (Fig. 4.1). This advance allows us to make simultaneous time-resolved measurements of both energetics and oxygenation. Here we demonstrate the power of this approach through a study of the effects of age on the metabolic response to acute oxidative insult in vivo.

In vivo measurements of mitochondrial coupling efficiency (P/O) and phosphorylation capacity (ATPmax) are both improved by simultaneous acquisition of MR and optical spectra. First, by performing a single experiment lasting less than one hour, we are able to measure mitochondria responding to acute changes in the intracellular environment. This approach provides a new window into in vivo metabolism compared to ex vivo approaches that remove mitochondria from the intracellular environment or in vivo approaches that measure ATP and oxygen separately. Second, by aligning measurements of PCr concentration and pH with measurements of oxygen saturations of Hb and Mb we are able to identify the time boundaries between which glycolysis and intracellular oxygen tension do not affect the rates of PCr hydrolysis or PCr synthesis (Fig. 4.3). These boundaries are critical when using PCr concentrations to calculate resting ATPase rate and mitochondrial ATPmax. The benefit of this ability is illustrated in Fig. 4.9, as calculating ATPmax from the point at which muscle reperfusion has elevated Mb saturation to 50% eliminates a significant association between Mb saturation and PCr recovery kinetics.

ROS-induced uncoupling in vivo

We have previously shown that an oxidative insult to mouse skeletal muscle results in ROS-induced uncoupling, independent of inherent mitochondrial defects (Chapter 3, (158)). This reduced coupling indicates an increase in proton leak that would lead to a reduction in mitochondrial membrane potential and a decrease in mitochondrial ROS production (20, 47, 159). The current study demonstrates that this antioxidant response of skeletal muscle mitochondria to acute oxidative insult persists even into old age, when mitochondrial function is already impaired (Fig. 4.5A). This result suggests that other mechanisms are responsible for tipping the balance in favor of a pro-oxidizing environment during the aging process. Coupled with existing data indicating that many antioxidant enzymes are maintained or upregulated in response to oxidative stress (62) and aging (73) these data support the hypothesis that increased ROS generation in aged mitochondria is the primary mechanism responsible for age-related oxidative stress

(131, 163). Interestingly, the relative decrease in P/O ratio was maintained regardless of preexisting inefficiency with age. As a result, downstream energetic consequences of dramatically decreased P/O (approximately 50% decrease in old PQ-treated mice relative to young controls) indicate a greater disruption of cell metabolism due to acute mild oxidative insult in aged mice.

In vivo P/O declines with advancing age in both mice (106) and humans (4). Similar to the age-related changes demonstrated here, we have previously reported a reduction in P/O ratio in 30 month old C57BL/6 mice and an associated decrease in ATP (106). Amara et al. also detected a loss of P/O ratio in vivo in the largely glycolytic first dorsal interosseous (FDI) muscle in aged humans. In the present study, the mouse hindlimb (also largely glycolytic (184)) mirrored the effect observed in the FDI. The study reported here expands upon these previous results by illustrating that, despite age related declines in P/O, aged muscle maintains the capacity to uncouple in response to an oxidative stimulus. It remains to be determined if the mechanisms underlying the reduced P/O in response to PQ differ in old and young skeletal muscle.

UCP3

The role of UCP3 in regulating ROS-induced proton leak in vivo in skeletal muscle remains controversial. Uncoupling proteins can be activated by ROS or by-products of lipid peroxidation to increase proton leak across the IMM in vitro (45). Mailloux, et al. recently demonstrated that UCP3 mediated proton leak in situ was acutely controlled by the glutathionylation of UCP3, which was sensitive to the redox state of the mitochondria (101). However, the role of UCP3 in ROS-induced uncoupling in vivo has yet to be directly tested. Therefore, we tested UCP3 activation as a potential mechanism to explain the ROS-induced uncoupling that we observed in vivo one day after PQ treatment. UCP3 protein expression decreased significantly with age and was unaffected by PQ-treatment suggesting that an alternative mechanism is a major contributor to ROS-induced uncoupling in mouse skeletal muscle.

However, this result does not rule out the possibility that existing UCP3 protein contributes to ROS-induced uncoupling as a result of post-translational modification (84, 101, 120).

Using UCP3$^{-/-}$ mice we conducted a more direct test of the role of UCP3 in ROS-induced uncoupling in vivo. Despite lacking UCP3, skeletal muscle mitochondria in young adult UCP3$^{-/-}$ mice exhibited decreased P/O one day after PQ treatment. The magnitude of this uncoupling was similar to the magnitude of uncoupling observed in our aging study indicating that the mechanisms responsible for our in vivo observations one day after PQ-treatment are independent of UCP3. In fact, we observed a non-significant trend toward a lower P/O value in untreated UCP3$^{-/-}$ mice relative to WT littermate controls (Fig. 4.7, WT data not shown). We speculate that one potential explanation for this may come from recent data indicating that UCP3 possesses antioxidant capacity independent of UCP3 mediated proton leak (175). Thus the absence of UCP3 in knockout mice may lead to higher oxidative stress and result in a trend toward mild ROS-induced uncoupling. Recent data suggest a model where UCPs are activated and deactivated by fluctuations in ROS on the order of one or two minutes, but longer increases in oxidative stress would deactivate UCP3 to preserve mitochondrial membrane potential (100, 175). Since our measurements were made one day after PQ treatment our results in the UCP3$^{-/-}$ mice do not preclude a role for UCP3 in ROS-induced uncoupling on this shorter time scale.

The other putative uncoupler in skeletal muscle mitochondria, ANT1, represents a possible alternative conduit for ROS-induced uncoupling (15). The quantity of ANT1 is expected to be more than 500-fold greater than that of UCP3 (22, 66) and we detected constant levels of ANT1 regardless of age or PQ-treatment (Fig. 4.6B). As a result, ANT1 mediated proton leak remains a potential mechanism to explain the reduced P/O with PQ treatment in skeletal muscle in vivo.

Effects of ROS-induced uncoupling on downstream energetics

Mitochondrial phosphorylation capacity (ATPmax) represents the capacity for oxidative phosphorylation to meet increases in cellular ATP demand beyond the resting rate (ATPase). In mice values for ATPmax are approximately 30 times greater than resting ATPase rate in vivo (158) indicating that the capacity for ATP synthesis far exceeds the ATP demand under resting conditions. However, under non-resting conditions (like contraction in the case of skeletal muscle), the rate of cellular ATP demand can increase several fold and exceed the mitochondrial phosphorylation capacity. Thus, reductions in ATPmax can lead to decreased fatigue resistance and impaired function. ATPmax was significantly lower in the oldest mice, despite a gradual increase in ETC complex protein expression with advancing age. This reduced capacity/content is consistent with previous reports in vivo in humans (34) and ex vivo in rodents (131) and could be due to decreased mitochondrial quality control and accumulation of oxidative damage to mitochondrial DNA and protein (35, 96).

Interestingly, PQ-treatment resulted in a significant decrease in ATPmax in old mice only. The relative change in ATPmax is in almost perfect agreement with the drop in P/O ratio in both old control (25% ΔP/O, 28% ΔATPmax) and old PQ-treated (50% ΔP/O, 49% ΔATPmax) mice relative to young controls, suggesting that ROS-induced uncoupling is responsible for the loss of capacity in both instances. This is contrary to results in young and middle aged mice in which changes in efficiency are insignificant at maximal rates of flux thus preserving the capacity for mitochondrial ATP production at higher flux rates. However, this loss of capacity represents a unique deficiency in old mice that indicates old mitochondria exist at the edge of an energetic threshold beyond which normal physiological fluctuations have significant consequences on reserve capacity for ATP production.

Intracellular ATP concentration is another measure of the ability of skeletal muscle mitochondria to maintain energy homeostasis. PQ-treatment led to drops in ATP content in middle aged and old, but not

young, mice (Fig. 4.10B). Under normal conditions, ATP is buffered by the activities of the creatine kinase and adenylate kinase reactions in skeletal muscle (90). As a result, mismatches between ATP production and ATP demand manifest as decreases in PCr/ATP and increases in AMP/ATP ratios while ATP remains constant. Net loss of ATP only occurs under conditions of severe energy stress when a chronically elevated AMP/ATP ratio leads to net loss of adenosine via enzymatic purine catabolism (169). Our results indicate that young mice are able to maintain energy homeostasis during ROS-induced uncoupling, while older mice enter a chronic state of energy stress that results in net loss of ATP.

We used T2-weighted MR imaging to rule out age-associated variations in tissue composition and/or fluid distribution as potential sources of error in our ATP concentration measurements. T2 relaxation times can be used as a relative measure of fluid distribution in tissue, with longer T2 relaxation times generally being associated with higher extracellular fluid fractions due to the contribution of this fluid compartment to the longest exponential decay component of T2 relaxation (1, 137, 147). No significant morphological (Fig. 4.14) or T2 relaxation time (Fig. 4.15) differences were detected between young and old mice under either resting or ischemic conditions, indicating that fluid distribution did not influence our conclusion that ATP is lower in old mice. Contrary to the results of a study illustrating longer T2 relaxation times in gastrocnemius in aging humans (69), we observed an insignificant trend towards a shorter T2 relaxation time in old vs. young, which suggests the extracellular fluid fraction in old mice was smaller than that in young. If this trend were to represent the norm, we would actually be overestimating the ATP concentration in old mice due to a larger volume of intracellular water diluting total metabolite volumes measured using HPLC. As a result, we have confidence that the relationships between age and energy state presented in this chapter are sound.

The energy sensitive kinase AMPK represents a safety valve on the way to the loss of ATP described above. Increases in the AMP/ATP ratio facilitate phosphorylation of AMPK, leading to activation of

numerous ATP-conserving mechanisms including increased glucose uptake, decreased protein synthesis, and stimulation of mitochondrial biogenesis (81). By decreasing ATP demand and increasing mitochondrial capacity, cells are given a chance to restore energy homeostasis. In line with changes in the AMP/ATP ratio, we detected increased phosphorylation of AMPK (Fig. 4.12) and decreased resting ATP demand (↓ATPase, Fig. 4.5B) in young PQ-treated mice. However, neither old control nor old PQ-treated mice exhibited increased phosphorylation of AMPK despite significantly elevated AMP/ATP ratios (Table 1). Interestingly, resting ATPase rate was lower in both treated and untreated old mice (Fig. 4.5B) suggesting that alternate mechanisms are responsible for decreasing ATP demand in old tissue. Age-related desensitization of the AMPK stress response has been described previously in response to exercise, AICAR treatment, βGPA feeding (143), and in situ muscle stimulation (97). In this case, insensitivity of the AMPK stress response represents another aspect of impaired mitochondrial adaptation with age that may amplify the energetic consequences of ROS-induced uncoupling and leads to a net loss of ATP.

Oxidative stress partially explains energetic inflexibility of old mice

As discussed previously, the buildup of oxidative stress is implicated as a cause of age-related degeneration. Therefore, in an effort to elucidate the mechanistic basis for the energetic inflexibility that we observed in old mice, we sought to recreate these effects by increasing the oxidative stimulus delivered to young mice.

We measured in vivo energetics and downstream signaling in young mice one day after administering doses of 0, 10, 20, or 30mg/kg PQ and found evidence that oxidative stress is a factor in the inability of old mice to maintain energy homeostasis during ROS-induced uncoupling. In agreement with the aging study, P/O ratio decreased by approximately 30% in response to PQ treatment, regardless of dose. This suggests that the activation threshold for ROS-induced uncoupling is met by low level ROS (or oxidative

byproducts) and that additional oxidative stimuli do not induce further uncoupling. The benefits of such a scenario are evident as mild uncoupling is expected to exert antioxidant benefits (159) while extreme uncoupling is associated with energy stress and apoptosis (121).

Despite the consistency of ROS-induced uncoupling, unique energetic changes resulted from increasing doses of PQ. PCr/ATP and AMP/ATP ratios exhibited distinct biphasic responses to increasing PQ dose (Fig. 4.13B and 4.13C), with dose-dependent signs of energy stress (i.e. ↓PCr/ATP and ↑AMP/ATP) persisting up to 20mg/kg followed by a return toward untreated levels at 30mg/kg. This degradation of typical fluctuation in phosphometabolite concentration is similar to the effect observed in old mice, in which PCr/ATP and AMP/ATP did not change in response to PQ-treatment (Table 4.1). These results suggest that, beyond a certain threshold of oxidative stress, typical changes in phosphometabolite concentrations associated with activity of the creatine kinase and adenylate kinase reactions fail to occur. These studies were not designed to elucidate the mechanism underlying this phenomenon, but it appears to occur regardless of whether the threshold is met by chronic (i.e. aging) or acute (i.e. PQ) changes in the oxidative environment. Associated with the dependence of AMPK phosphorylation on the AMP/ATP ratio and, less significantly, the PCr/ATP ratio (81, 134), there was a leveling-off of the dose-dependent increase in AMPK phosphorylation between 20 and 30mg/kg PQ. These results suggest that disruption of the relationship between P/O ratio and the PCr/ATP and AMP/ATP ratios is a possible link between oxidative stress and age-related insensitivity of AMPK-dependent energy signaling observed by us (Fig. 4.12) and others (143).

Much like the effect observed in old mice, ATPmax was significantly lower in young mice after a PQ dose of 30mg/kg. Sensitivity of ATPmax to ROS-induced uncoupling may be explained by the effects of oxidative stress on mitochondrial machinery, making mitochondria more susceptible to mild uncoupling at maximum flux. It is also possible, though unlikely, that the reduction in ATPmax is a measurement

artifact resulting from decreased activity of creatine kinase limiting the rate of PCr replenishment during recovery from ischemia (16, 123). Interestingly, unlike changes observed in old mice, ATP concentration was unaffected regardless of PQ dose in young mice. Despite the leveling effect discussed above, activation of AMPK (Fig. 4.13D) may contribute to this maintenance of energy homeostasis during ROS-induced uncoupling.

Significance and Conclusions

We demonstrate qualitative differences in the effect of acute oxidative insult on in vivo energetics in young and old skeletal muscle. Using multi-modal in vivo spectroscopy we provide evidence for the persistence of ROS-induced uncoupling of oxidative phosphorylation throughout life. This reduced coupling appears to be independent of UCP3 and is maintained despite downstream energetic consequences. These consequences result from concurrent decreases in coupling efficiency (P/O), oxidative phosphorylation capacity (ATPmax), and desensitization of AMPK phosphorylation, which results in a net loss of ATP in old age. As a result, aged mitochondria maintain the capacity to respond to acute changes in the oxidative environment but lack the plasticity to maintain energy homeostasis in face of the induced changes to mitochondrial energetics.

Chapter 5

Rapid Reversal of Mitochondrial Dysfunction by a Mitochondrial Targeted Peptide Improves Skeletal Muscle Performance in Aged Mice

Abstract

Oxidative stress resulting from mitochondrially-generated reactive oxygen species (ROS) is considered a key element in the debilitating degeneration of aged skeletal muscle function. Here we test whether acute treatment with the mitochondrial targeted peptide SS31 is able to rescue in vivo mitochondrial energetics by reducing the oxidative potential of the intracellular environment. Using our unique, multi-modal magnetic resonance (MR) and optical spectroscopy system we assess in vivo mitochondrial energetics in skeletal muscle of old mice one hour after IP injection with SS31. Following SS31 treatment the intracellular environment was significantly reduced (higher reduced:oxidized ratio of glutathione, GSH/GSSG), and mitochondrial coupling efficiency (P/O ratio) and phosphorylation capacity (ATPmax) were elevated to levels measured in young mice. These results reveal a hidden functional capacity of aged mitochondria and support the hypothesis that depressed mitochondrial energetics with age result from reversible interaction with an oxidative environment rather than permanent oxidative damage. To examine the relevance of this energetic recovery at the whole-organism level, we went on to study live muscle fatigue and whole body endurance following SS31 treatment in old mice. In situ muscle fatigue resistance, time to exhaustion during forced treadmill running, and latency time to falling from a rotating spindle (Rotarod) were all significantly improved with SS31. This indicates that improved mitochondrial energetics resulting from SS31 treatment translates directly to improved exercise capacity in live organisms, and suggests a promising therapeutic application of SS31 in aging humans.

Introduction

Muscle function declines with age, resulting in weakness and fatigability which limit quality of life and contribute to growing health care burden of the aging population (13, 180). While a suite of etiologies are likely to contribute to this decline, depression of mitochondrial function remains a focal point in the study of age-related skeletal muscle degeneration and disease (34, 77, 121).

Oxidative damage to proteins, lipids, and mtDNA resulting from exposure to increasing levels of reactive oxygen species (ROS) during life is often considered the cause for age-related mitochondrial dysfunction (65, 68, 77). However, a growing body of evidence indicates that the age-related changes in mitochondrial function may be a result of the more subtle influence of a shifting intracellular redox environment (101, 109, 162). As a result, dysfunction may not be dysfunction, per se, but rather the physiological response of functional mitochondria to a more oxidative environment in aged cells. Supporting this hypothesis, we have demonstrated the influence of oxidative stress over coupling of oxidative phosphorylation and energy state in vivo in the absence of intrinsic mitochondrial changes (Chapter 3) and in aged mice (Chapter 4).

The notion that reversible functional regulation by an oxidative environment is responsible for age-related mitochondrial "dysfunction" suggests that the energetic consequences of age can, in fact, be rescued by a net reductive shift of the oxidative environment. Researchers have tested the role of oxidative stress on age-related dysfunction and lifespan (116, 128) with some of the most promising results have been realized using mitochondrially-targeted antioxidant approaches (181). Schriner et al., for example, extended mean lifespan of mice by more than 4 months by transgenically targeting the antioxidant enzyme catalase to the mitochondrial matrix (157). While such studies show significant promise, they are unable to delineate the roles of oxidative damage and oxidative regulation due to long periods of time during which mitochondria can adapt (or fail to adapt) to environmental changes (25, 57, 144, 194).

Schiller-Szeto (SS) peptides are a novel class of therapeutic tetrapeptides that rapidly localize to the inner mitochondrial membrane (IMM) (170, 196). In particular, SS31 (Fig. 5.1), brings with it therapeutic benefits which include decreased rates of mitochondrial ROS production in skeletal muscle (5, 196). While not fully understood, this antioxidant activity is suspected to arise from activity of the dimethyltyrosine residue at the second position of the amino acid chain (172). SS peptides have been demonstrated to improve the outcome in numerous disease states in which oxidative stress is implicated, including ischemia-reperfusion injury (173), neurodegeneration (171), insulin resistance (5), and skeletal muscle disuse atrophy (112, 136).

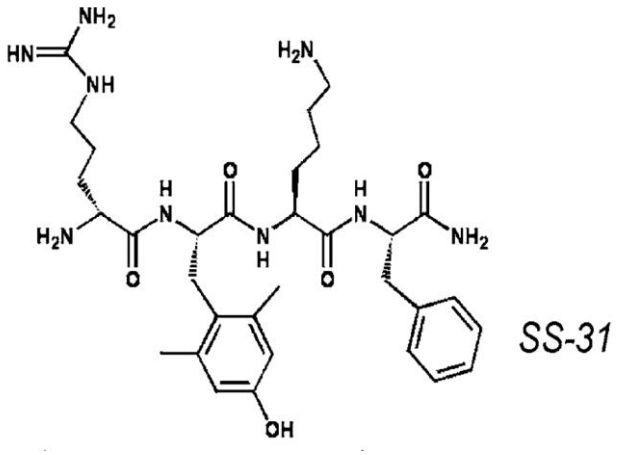

Figure 5.1. Chemical structure of SS31 adapted from (172).

In this chapter we test the hypothesis that SS31 treatment in old mice will rapidly rescue in vivo mitochondrial energetics towards the young phenotype due to recovery of the intracellular oxidative environment. To address this hypothesis we use multi-modal in vivo spectroscopy to measure mitochondrial energetics in mouse skeletal muscle at a single, early time-point following treatment with SS31. We go on to characterize the effects of SS31 on the intrinsic properties of aged mitochondria in permeabilized muscle, and to measure the effects on live muscle function and animal endurance. Our results describe a potential therapeutic benefit of SS31 in the future and provide evidence supporting regulation of mitochondrial function by an oxidative environment in aged organisms.

Methods

Animals

This study was approved by the Institutional Animal Care and Use Committee of the University of Washington. Female C57BL/6 mice were purchased from the NIA aged mouse colony. Mice between 5 and 11 months old were considered young while mice between 27 and 29 months old were considered old. All mice were exposed to a 12 hour light/dark cycle in a fixed-temperature environment with free access to water and standard mouse chow until immediately prior to experimentation. Mouse body temperatures were maintained at 36°C ± 1°C throughout in vivo and in situ experiments.

SS31Treatment

SS31 dissolved in isotonic saline at a concentration of 100mg/mL was obtained from Dr. Hazel Szeto at Weill Cornell Medical College and then diluted to 0.3mg/mL to make injectable SS31 stock. For the treatment dose of 3mg/kg, mice received IP injections of 0.01mL of injectable stock per gram of body weight.

SS31 Tissue Distribution

The time-course of distribution of ^{125}I-SS-31 to different tissues was determined elsewhere through a collaboration with Dr. Hazel Szeto. After subcutaneous administration of ^{125}I-SS-31 (0.126 mg, 605.89 kBq) in 12 mice, three animals were sacrificed at each time point (0.5, 2, 6 and 16 hours after dosing). The gamma radioactivity of each sample was determined and the results presented as radioactivity per gram tissue.

Multi-Modal Spectroscopy

Refer to Chapters 2 and 4 methods for detailed methods on multi-modal in vivo spectroscopy and the subsequent methods used to analyze data. In this chapter, all in vivo spectroscopy was carried out using the 7T system at the University of Washington Medical Center.

Muscle Metabolites, Hemoglobin, and Myoglobin

Methods used to measure metabolite concentrations are the same as those presented in Chapter 3. Methods used to measure Hb and Mb concentrations are the same as those presented in Chapters 4.

Mitochondrial Protein Content

Protein expression analysis of mitochondrial ETC complexes was accomplished using western blotting. Aliquots of pulverized gastrocnemius were combined 1:25 with lysis buffer containing 0.1% protease inhibitor (Sigma #P8340) and homogenized at 4°C using a Bullet Blender 24 (Next Advance, Averill Park, NY). The resulting lysate was combined 1:1 with Laemmli sample buffer (#161-0737, Bio-Rad, Hercules, CA) containing 350mM DTT and proteins separated on 4-20% gradient gels at 200V for 75 minutes. Proteins were transferred to nitrocellulose membranes, Ponceau stained to ensure uniform transfer and loading, and then immunoblotted as follows: After blocking in 3% BSA for 1hr at RT, membranes were incubated in primary (1:1K MitoSciences #604, overnight at 4°C) and then secondary (1:10K Cell Signaling #7076, 2hr at RT) antibodies. Antibodies were diluted in 1%BSA in 0.1% TTBS. Membranes were developed using Immun-Star Western C Chemiluminescence Kits (Bio-Rad), imaged using a ChemiDoc imaging system, and band densities measured using QuantiyOne. ETC complex band intensities were normalized to lane intensity of Ponceau stain to account for variations in loading volume.

GSH/GSSG Ratio

The ratio of reduced to oxidized glutathione was determined in gastrocnemius using a modified version of the fluorescent HPLC method described in detail by White, et al. (187). One hour after injection with either 3mg/kg SS31 or volume-matched saline, muscle was dissected from live, Avertin-anesthetized mice, weighed quickly, submerged in 0.5mL of cold 5% salicylic acid (SSA), and manually homogenized over ice using a glass tissue grinder. After incubating on ice for 15min to allow proteins to precipitate, homogenates were centrifuged at 4°C for 15min at 13,000 RPM, and the resulting supernatant taken for analysis. For GSSG, 100µL of sample was combined with 400µL phosphate buffered saline (pH 7.4), 50µL of 10% triethanolamine, and 4 µL of 2-vinylpyridine (to derivatize GSH). This mixture was vortexed for 30 minutes, then combined with 500 µL chloroform and vortexed for an additional 15 minutes to phase-separate excess 2-vinylpyridine and GSH-2-vinylpyridine conjugate from GSSG. The resulting mixture was centrifuged at 13,000 RPM for 2 minutes, and then 100 µL of the top, aqueous phase was combined with 200 µL 100mM NaH_2PO_4, 1mM EDTA and 10 µL TCEP to reduce GSSG in solution. After incubating for 20min at RT, 20 µL of 6.25mM monobromobimane was added and incubated for 30min to derivatize the GSH yielded by GSSG reduction. For GSH, the original sample was diluted 1:9 with SSA and then 100 µL was combined with 400µL phosphate buffered saline (pH 7.4), 50µL of 10% triethanolamine. 100 µL of this mixture was combined with 200 µL 100mM NaH_2PO_4, 1mM EDTA and 10 µL H_2O and then allowed 30min to incubate with 20 µL of 6.25mM monobromobimane. The fluorescent derivative of GSH and monobromobimane (excitation/emission of 375/475nm) was then quantified for all samples by HPLC (Shimadzu SCL-10AVP Columbia, MD).

Ex Vivo Mitochondrial Respiration

Freshly dissected, gently separated and permeabilized (50µg/ml saponin, 4°C, 40min) extensor digitorum longus (EDL) and soleus muscle fibers were stirred at 25°C in a 2ml vessel of an oxygen monitoring

apparatus (O2k system, Oroboros Instruments, Austria). Corresponding muscle from contralateral legs were run simultaneously, with one chamber receiving 5µL of 40mM SS31 (final concentration of 100µM SS31) and the other receiving 5µL of water for volume control. Each chamber was then provided with 10mM glutamate, 5mM pyruvate, and 2mM malate without ADP to measure proton leak-driven respiration ("state 4") and then given 2.5mM ADP to stimulate state 3 respiration with complex I substrate. To measure the contribution of non-mitochondrial oxygen consumption, 2.5µM antimycin A was added after achieving steady state 3 respiration. The amount of oxygen consumed was calculated by assuming the oxygen solubility factor of media to be 0.920 and by calibrating initial oxygen concentration in the buffer for each experiment and correcting for pressure, temperature, and instrumental oxygen consumption as described by Gnaiger et al. (55).

H_2O_2 Emission in Permeabilized Muscle Fibers

H_2O_2 production was measured using Amplex Red, which reacts with H_2O_2 to produce the fluorescent molecule resorufin (excitation/emission of 590/530-560nm). EDL muscles were dissected, mechanically separated, and permeabilized following the method used for ex vivo mitochondrial respiration measurements described above. Muscles were then combined with 12.5µM Amplex Red, 2U/mL horseradish peroxidase, 10µM succinate and either SS31 or volume-matched water in a total reaction volume of 200µL. SS31 concentrations of either 500nM or 100µM were used, with no difference in H_2O_2 production between the two concentrations. Succinate was used as substrate to achieve maximum H_2O_2 production by reverse electron flow through complex I (165). Fluorescence was measured on a standard plate-reader and calibrated using standards of known H_2O_2 concentration.

In Situ Muscle Force and Fatigue

In situ analysis of tibialis anterior (TA) muscle function was performed following a protocol described elsewhere (127). Forty-five minutes after injection with either 3mg/kg SS31 or volume-matched saline,

mice were anesthetized with Avertin and the distal TA tendon was surgically isolated. Mice were then positioned on a heated platform with the limb restrained at the knee joint and the distal tendon attached by silk sutures to the lever arm of a servomotor (Model 305B-LR, Aurora Scientific, Aurora, ON, Canada). The exposed surface of the muscle was kept moist with isotonic saline and muscle stimulation was delivered at a voltage of 4.5V through the peroneal nerve using two needle electrodes. Custom-written software in LabVIEW (National Instruments, Austin, TX) was used to control electrical stimulation and to acquire force vs. time data. After adjusting muscle length to optimize tetanic force output (tetanic stimulus: 200Hz stimulation frequency for 300msec), force-frequency measurements were made by delivering stimuli once per minute at frequencies ranging from 10 to 250 Hz to test muscle contractile response to submaximal and maximal stimulation frequencies. Fatigue measurements were then made by delivering tetanic stimuli at 2sec intervals for 4 minutes. Additional tetanic stimuli were delivered 1 minute and 5 minutes after the final fatigue stimulus to assess recovery from fatigue. If tetanic muscle force failed to reach >90% of pre-fatigue levels after 5 minutes of recovery muscle damage was likely to have occurred and data were discarded. After the completion of testing, muscle length and mass were measured and used to calculate specific tetanic force (127). Following in situ experiments, raw data were taken to custom-written MATLAB software for analysis. For twitch force and force-frequency measurements, peak force during contraction was recorded. For tetanic stimuli, the (force)(time) integral was calculated for the entire duration of contraction.

Treadmill Test

Following 8 days of daily IP injections with 3mg/kg SS31 or volume-matched saline, endurance capacity of mice was assessed by measuring time to failure during forced running on a treadmill (Eco 3/6, Columbus Instruments, Columbus, OH). Mice first underwent two days of acclimation (on injection days 6 and 7), during which they were allowed to explore motionless treadmill lanes for 1 minute, become familiar with the motivational shocking grid for 1 minute, and walk at a rate of 20m/min at a 0º incline for

2 minutes. On the following day (commencing one hour after injection on the 8th day), mice ran at a rate of 30m/min at a 10º incline until failure. Time to failure was recorded manually and failure was determined when mice were unable to maintain position on the treadmill despite electrical shock and light prodding for 10 seconds. Studies were carried out between 6pm and 8pm to observe mice during the active dark cycle.

Rotarod

Rotarod assays were carried out using a Rotamex-5 (Columbus Instruments) with an accelerating spindle protocol based on methods described elsewhere (117). Mice were placed in individual lanes on a rotating spindle which accelerated from standstill at a rate of 0.1 RPM/sec until mice failed to maintain balance. The Rotamex system and accompanying Rotamex-5 Software automatically recorded time to failure (latency time) using a system of photobeams; mice in position atop the spindle break the paths of 5 photobeams and failure was determined when no photobeams were broken. After one day of acclimation, during which a single turn on the spindle was taken by each mouse, old mice were injected with either 3mg/kg SS31 or volume-matched saline one hour prior to Rotarod assays on three consecutive days. On these experiment days, each mouse performed three tests on the Rotarod separated by at least 30min and median latency time was reported. Studies were carried out between 6pm and 8pm to observe mice during the active dark cycle.

Voluntary Wheel Running

Old mice were individually housed in standard cages containing low-profile wireless running wheels (ENV-044, Med Associates Inc, St. Albans, VT). After a 4 day acclimation period during which mice lived in cages with locked running wheels to gain familiarity, wheels were unlocked so that mice could run freely. Mice remained in cages with access to free wheels for a period of two weeks while receiving injections of either 3mg/kg SS31 or volume-matched saline approximately one hour before the onset of

the active dark cycle every day. The number of wheel revolutions per cage was transmitted wirelessly to a hub linked to a laptop computer and recorded once per minute. Total running distance was calculated assuming an average running radius of 6.02cm.

Statistics

Statistical analysis was carried out using Prism 5 software (GraphPad, La Jolla, CA). Two-tailed student's t-tests were used to compare groups. The boundary for statistical significance was set at $p = 0.05$.

Results

To determine whether SS31 improves mitochondrial energetics in old mice we administered 3mg of SS31 per kg of body weight by IP injection and used multi-modal in vivo spectroscopy to measure mitochondrial function after approximately one hour. As controls we administered volume matched doses of saline (C) to both young and old mice and the same dose of SS31 to young mice. As illustrated in Fig. 5.2, SS31 concentrations were significantly elevated in skeletal muscle, brain, and fat at this early time-point after administration to mice.

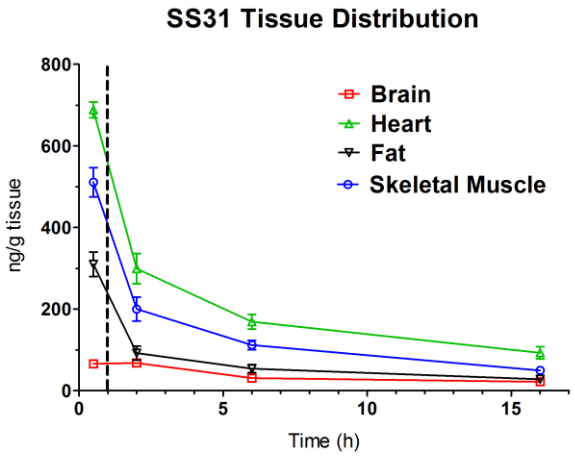

Figure 5.2. SS31 clears rapidly from most tissues of the mouse following a single injection. After one hour (dashed line), SS31 levels are elevated in heart, fat, and skeletal muscle.

Thus we aimed to study the direct interaction between SS31 and mitochondria rather than any downstream modifications that may take place as a result of SS31 treatment (e.g. mitochondrial biogenesis). No difference in protein expression of ETC complexes I-V was observed between old untreated and old SS31-treated mice (Fig. 5.3).

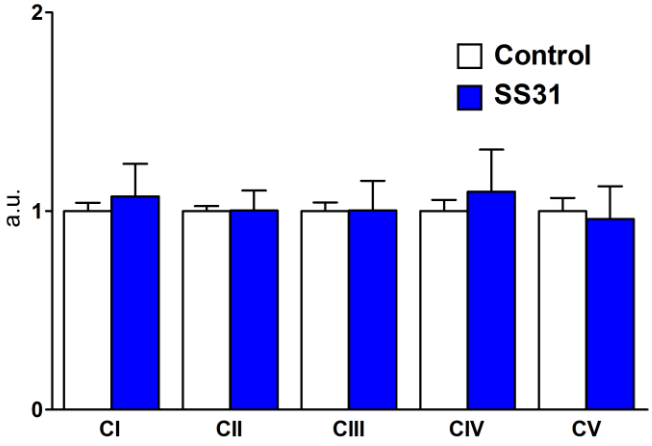

Figure 5.3. ETC complex protein expression was not different one hour after injection of 3mg/kg SS31 in old mice. Data are expressed as means ± SEM, normalized to control averages, with n=5 per group.

However, the presence of SS31 in skeletal muscle one hour after injection did significantly affect the intracellular oxidative environment in old mice, as measured by an increase in the ratio of reduced to oxidized glutathione (GSH/GSSG) to values typical of young mice (Fig. 5.4B). Glutathione is one of the most abundant and sensitive redox sensors in cells and its oxidation state is considered an important measure of the oxidative environment (141). To link this shift in redox state to the antioxidant benefits of SS31 we performed the H_2O_2-sensitive Amplex Red assay on permeabilized EDL muscle from old mice in the presence and absence of exogenous SS31. As illustrated in Fig. 5.4A, SS31 significantly reduced H_2O_2 emission.

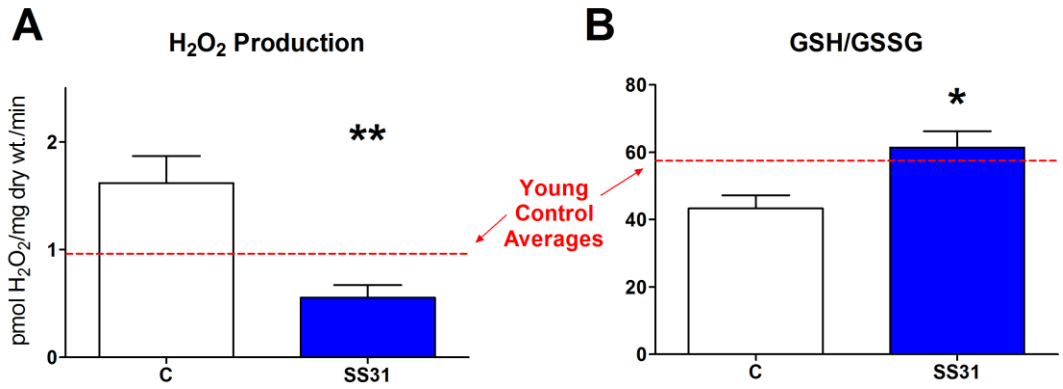

Figure 5.4. In old mice (A) H_2O_2 emission in permeabilized EDL was significantly lower in the presence of SS31, and (B) the GSH/GSSG was significantly elevated in gastrocnemius one hour after a single SS31 injection. Thus, SS31 lowers oxidative stress and adjusts the oxidative environment to reflect conditions similar to those in young mice (red dashed lines). Data are expressed as means ± SEM, n = 4 per group. *p<0.05, **p<0.01.

SS31 Rapidly Reverses Age-Related Energetic Deficits

As described in Chapters 2 and 4, our multi-modal in vivo spectroscopy approach uses a unique probe capable of simultaneously acquiring ^{31}P MR spectra and near infrared (NIR) optical spectra through the distal mouse hindlimb during periods of rest, brief ischemia, and recovery. Representative spectra acquired from mice used in this study and the associated analyses are presented in Figs. 5.5 and 5.6, respectively.

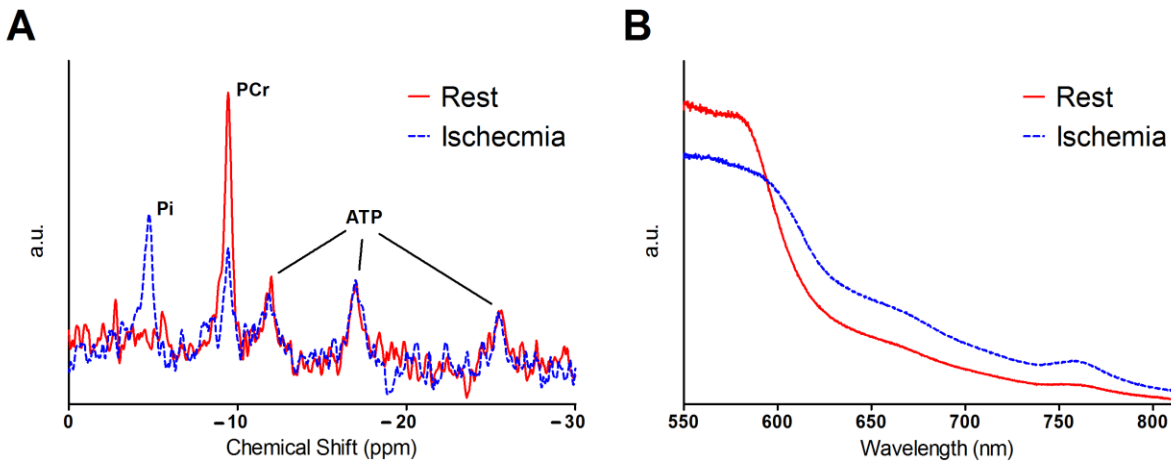

Figure 5.5. (A) Representative in vivo ^{31}P MR spectra acquired during dynamic experiment following 20Hz line-broadening and summing 3 consecutive FIDs. (B) Representative in vivo NIR optical spectra acquired during dynamic experiment.

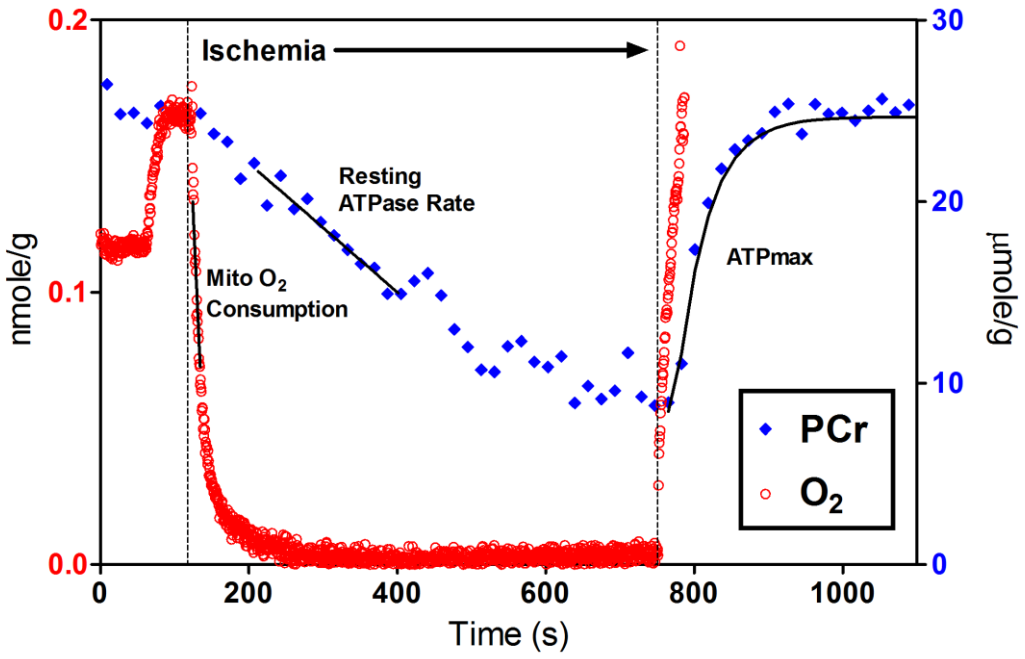

Figure 5.6. Analysis of dynamic in vivo spectra in conjunction with biochemical measures of hemoglobin, myoglobin, and ATP yields a noninvasive assessment of mitochondrial oxygen consumption, resting ATP demand (ATPase) rate, and oxidative phosphorylation capacity (ATPmax). Total oxygen content on the left axis and PCr concentration on the right.

Key in vivo measurements, illustrated in Fig. 5.6, include:

1. The resting rate of mitochondrial oxygen consumption, calculated as the rate of decrease in total oxygen in the closed system of the ischemic hindlimb.

2. Resting ATP demand (ATPase rate), calculated as the rate of decline in PCr concentration as activity of the creatine kinase reaction is used to meet ATP demand under anaerobic conditions.

3. Maximal rate of mitochondrial oxidative phosphorylation (ATPmax) calculated as the rate of return to resting concentration of PCr during recovery from ischemia.

4. The efficiency with which mitochondria couple the proton-pumping redox events of the ETC to the phosphorylation of ADP→ATP at complex V can be calculated as ½ the ATPase rate divided by the rate of oxygen consumption (P/O ratio).

As previously reported, P/O ratio was significantly depressed in old vs. young control mice (Chapter 4, (106)). One hour after SS31 treatment, P/O in old mice was fully recovered to the level of young mice (2.12±0.17 for old SS31-treated vs. 2.09±0.14 for young untreated) (Fig. 5.7C). These changes mirror the effect of SS31 upon resting ATP demand, as ATPase was significantly depressed with age and recovered with SS31 (Fig. 5.7A). Resting rate of oxygen consumption was not different between groups and

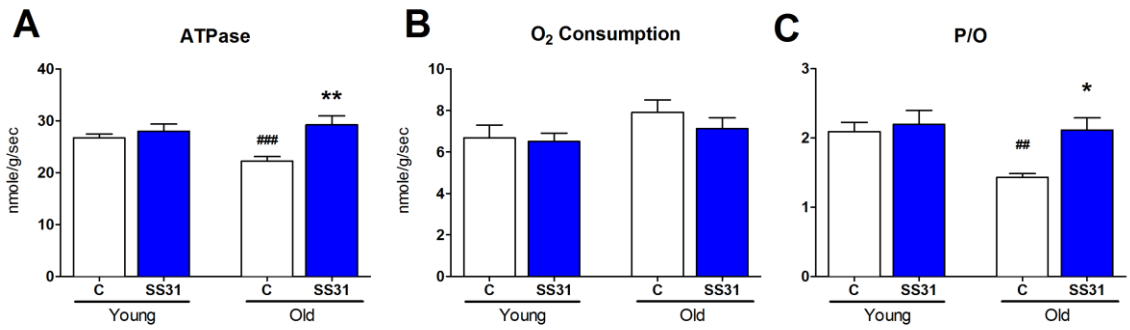

Figure 5.7. (A) ATPase was significantly lower in old mice and recovered one hour following SS31 treatment, while (B) oxygen consumption remained constant. As a result, (C) P/O ratio was rescued by SS31-treatment back to young levels. SS31 had no effect on ATPase rate or oxygen consumption in young mice. Data are expressed as means ± SEM. n=5-7 per group. *p<0.05, **p<0.01 relative to age-matched control. ##p<0.01, ###p<0.001 relative to young control.

SS31 treatment had no effect on young mice (Fig. 5.7B). Interestingly, we also observed a delay between the start of ischemia and the onset of PCr hydrolysis in old SS31 treated mice that was not present in old controls, suggesting that oxidative phosphorylation may have been able to persist under lower oxygen tensions in the presence of SS31 (Fig. 5.8).

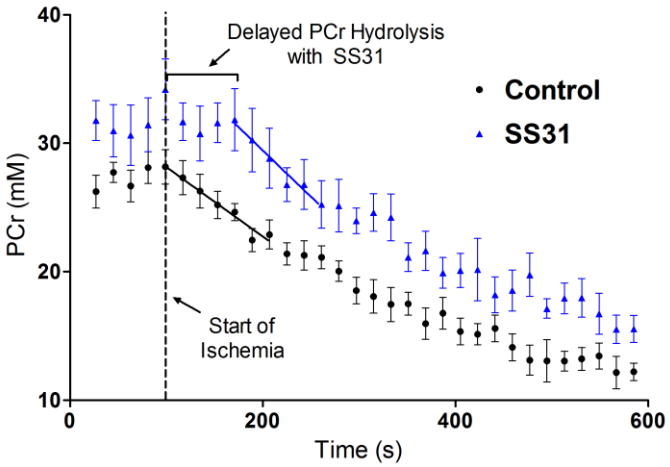

Figure 5.8. In addition to an elevated resting PCr concentration in old SS31-treated mice (Table 5.1), SS31 delayed the onset of PCr hydrolysis following ischemia and increased the rate of PCr decline. Data are expressed as means ± SEM. n = 5-7 per group.

Similar to the changes we observed in P/O ratio, cellular energy state, as measured by the PCr/ATP ratio, was significantly depressed with age and recovered to young levels one hour after SS31 treatment. As illustrated in Figs. 5.9, the fully-relaxed ^{31}P MR spectral peak area of PCr was larger relative to that of γATP in SS31 treated mice resulting in a significant increase in PCr/ATP.

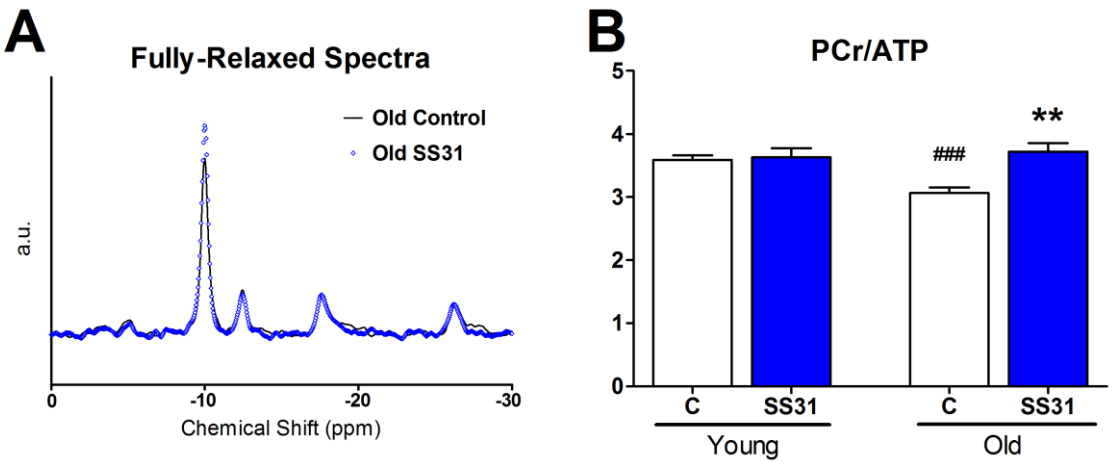

Figure 5.9. (A) Representative fully relaxed spectra from SS31-treated and control old mice illustrate an increase in relative peak area of PCr to ATP, resulting in (B) a net recovery of PCr/ATP ratio in old mice. Data are expressed as means ± SEM. n=5-7 per group. **p<0.01 relative to age-matched control. ###p<0.001 relative to young control.

Mitochondrial phosphorylation capacity was also improved by SS31 in old mice. The rate of PCr recovery after ischemia was faster in SS31-treated old mice resulting in a 72% increase in ATPmax (Fig. 5.10). A list of metabolite concentrations used for MR analysis is provided in Table 5.1.

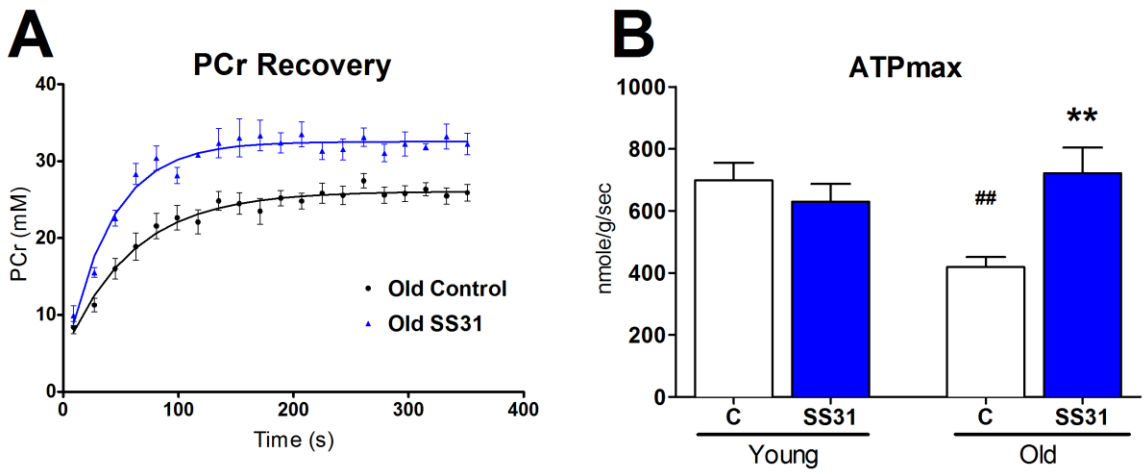

Figure 5.10. (A) After ischemia, PCr recovered to a greater concentration at a faster rate in old mice following SS31 treatment, revealing (B) a significant increase in ATPmax. Data are expressed as means ± SEM. n=5-7 per group. **p<0.01 relative to age-matched control. ##p<0.01 relative to young control.

Table 5.1. Metabolites from young and old SS31-treated skeletal muscle. Data for ATP and total creatine (Cr) are from HPLC and all other values were calculated from MR spectra. * p<0.05, ** p<0.01, *** p<0.001 relative to young control; # p<0.05, ## p<0.001 relative to age-matched control.

	YOUNG		OLD	
	C	**SS31**	**C**	**SS31**
ATP(mM)	10.26±0.29	9.20±0.14	7.98±0.22**	7.69±0.15
PCr(mM)	36.83±1.31	33.36±1.20	24.43±0.75***	29.29±1.89#
P_i(mM)	3.55±0.37	2.31±0.31	2.40±0.23*	2.18±0.22
Cr(mM)	43.19±1.40	41.48±0.61	38.11±1.16*	38.06±0.90
ADP(µM)	15.56±2.45	19.82±3.13	33.72±2.25 *	19.45±3.00
AMP(µM)	25.41±7.12	42.02±12.46	131.30±17.80***	51.07±18.33
pH_{Rest}	7.07±0.01	7.10±0.05	7.02±0.02	7.06±0.03
$pH_{Ischemia}$	6.96±0.01	6.95±0.01	6.90±0.03	6.88±0.02

SS31 Reduces Proton Leak in Permeabilized Muscle Fibers

To determine the source of the in vivo energetic differences that we observed in old mouse skeletal muscle, we measured ex vivo mitochondrial respiration in permeabilized muscle fibers from old mice in the presence and absence of 100μM SS31. Paired experiments were carried out on both the primarily Type I soleus and primarily Type II EDL, using muscle from the contralateral leg of the same animal as control. As depicted in Fig. 5.11, we observed no difference in ADP-driven respiration with saturating complex I substrates (state 3), however leak-driven respiration (saturating complex I substrates in the absence of ADP, state 4) was significantly lower in both soleus and EDL in the presence of SS31. This indicates that SS31 reduced proton leak across the mitochondrial inner membrane and is consistent with the improved P/O that we observed in vivo.

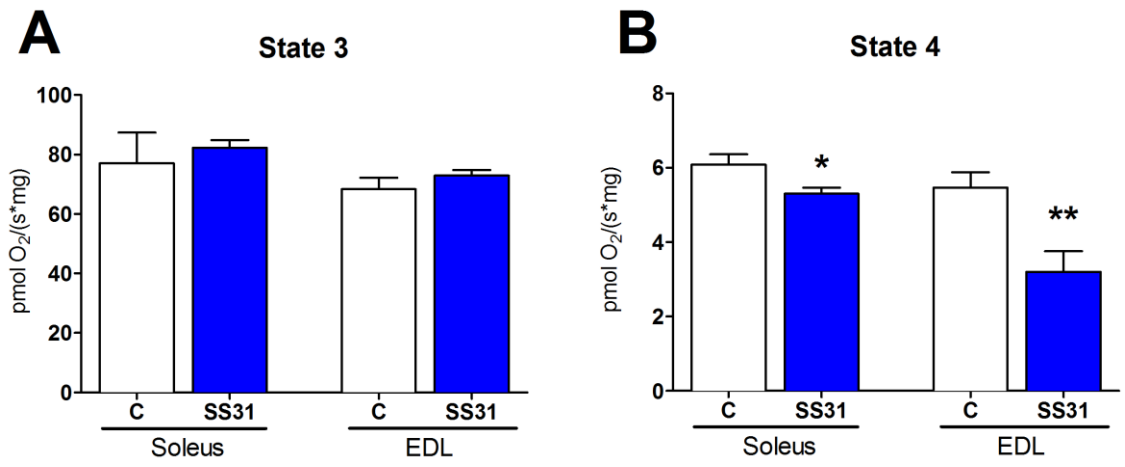

Figure 5.11. (A) Under state 3 conditions SS31 had no effect on oxygen flux in either the soleus or EDL of old mice. (B) Under state 4 conditions, SS31 was associated with reduced oxygen flux indicative of decreased proton leak across the IMM. Data are expressed as means ± SEM. n=4 per group. *p<0.05,**p<0.01 relative to same muscle type control.

SS31 Improves Fatigue Resistance in Old Mouse Muscle

Having detected improvements in mitochondrial energetics in vivo and a reduction in proton leak ex vivo we next sought to assess the effect that these improvements have on muscle performance in live mice. We hypothesized that improved mitochondrial energetics would lead to improved muscle endurance and resistance to fatigue. As a first step we measured in situ muscle fatigue in the tibialis anterior (TA) of old mice one hour after treatment with either 3mg/kg SS31 or volume-matched saline (control), according to the protocol described in (127). As illustrated in Fig. 5.12A, the rate of force decay slowed considerably in SS31-treated mice relative to control after approximately 18 seconds. After a full 4 minutes of repeated tetanic stimuli, the percent of total force maintained in the muscle of SS31-treated mice was significantly greater than control (Fig. 5.12B). Maximum tetanic force and force-frequency response were unaffected by SS31 (Fig. 5.13).

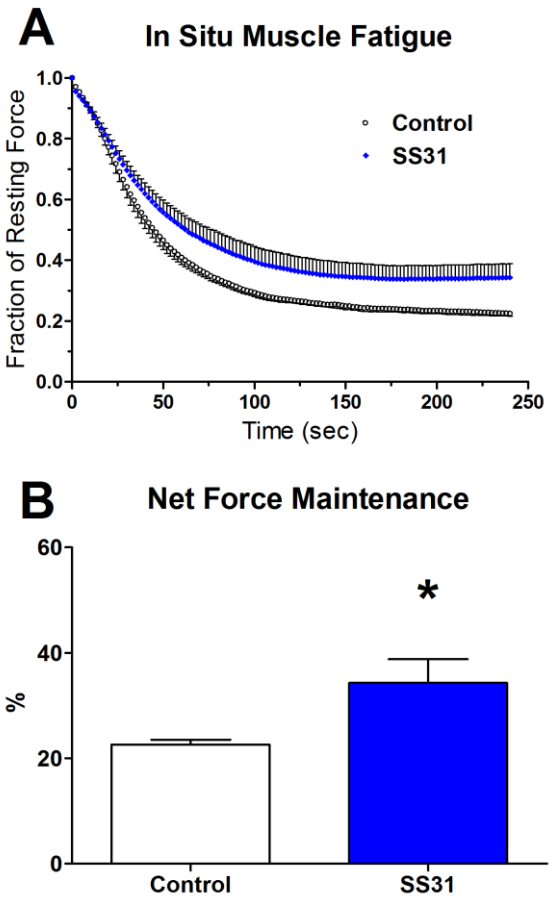

Figure 5.12. (A) Plots of force vs. time during repetitive tetanic stimuli were distinctly different in old control and old SS31-treated mice, with SS31 treatment slowing the rate and magnitude of force decay. (B) Net force maintained by TA muscle at the end of fatigue experiments was significantly higher in SS31-treated mice. Data are expressed as means ± SEM. n=6-7 per group. *p<0.05.

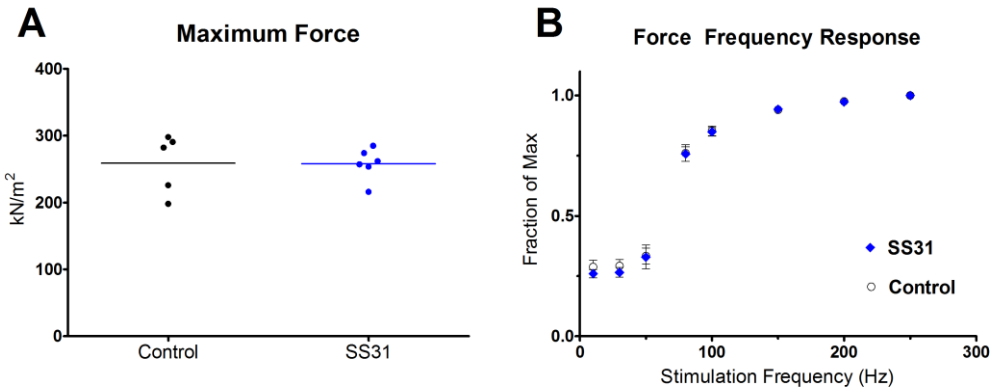

Figure 5.13. (A) Maximum tetanic force and (B) the force-frequency response in old muscle was the same regardless of SS31-treatment. Lines in (A) represent group means. Data in (B) presented as mean ± SEM, n = 5-6 per group.

SS31 Improves Whole Body Endurance in Old Mice

To see if the SS31-associated improvements in mitochondrial energetics and fatigue resistance translated into improvements in whole body exercise capacity we measured the time to failure of old mice subjected to forced treadmill running after one week of daily IP injections with 3mg/kg SS31. As illustrated in Fig. 5.14, SS31-treated mice were able to run at a rate of 30m/min and an upward incline of 10° for a longer period of time. In fact, 2 treated mice were still running at the end of the allotted 30min running session.

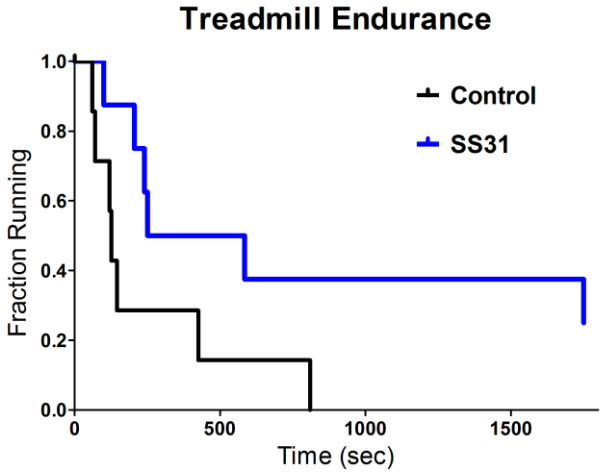

Figure 5.14. Old mice ran longer during forced treadmill running after one week of daily SS31 injections.

We also used the Rotarod assay to assess physical performance, encompassing factors including balance, coordination, and learning. Rotarod tests were conducted for three consecutive days on which old mice received either saline or 3mg/kg SS31 one hour prior to testing. As presented in Fig. 5.15, between the first and third day SS31-treated mice improved latency time on the Rotarod spindle significantly while saline-treated mice did not.

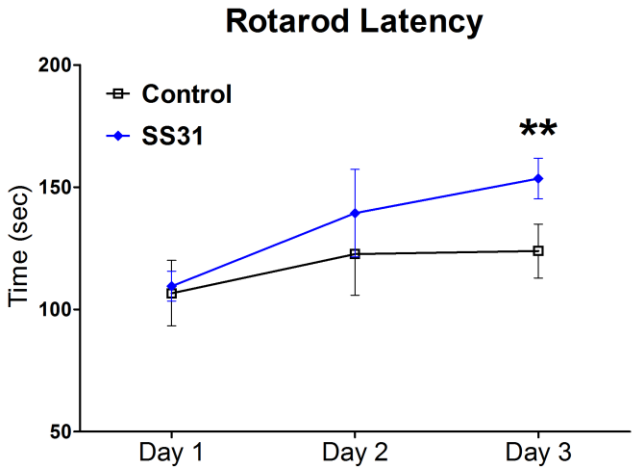

Figure 5.15. By the third day of Rotarod testing, latency time in SS31-treated old mice improved relative to Day 1 (**, $p<0.01$). The difference between SS31 and control on the third day approached, but did not achieve, significance ($p = 0.06$). Data presented as mean ±SEM. n = 6-8 per group.

To test the psychological motivation to run alongside physical endurance capacity, groups of old mice were given free access to running wheels for a period of two weeks, receiving daily IP injections of either 3mg/kg SS31 or volume matched saline. As illustrated in Fig. 5.16A, SS31-treatment did not improve daily running distance in old mice suggesting that SS31 does not improve the motivation to conduct physical activity despite an improved capacity to do so. Control and SS31-treated mice exhibited similar patterns of subtle, gradual weight-loss over the two-week period consistent with the benefits of a continuous exercise regimen (Fig. 5.16B, (148)).

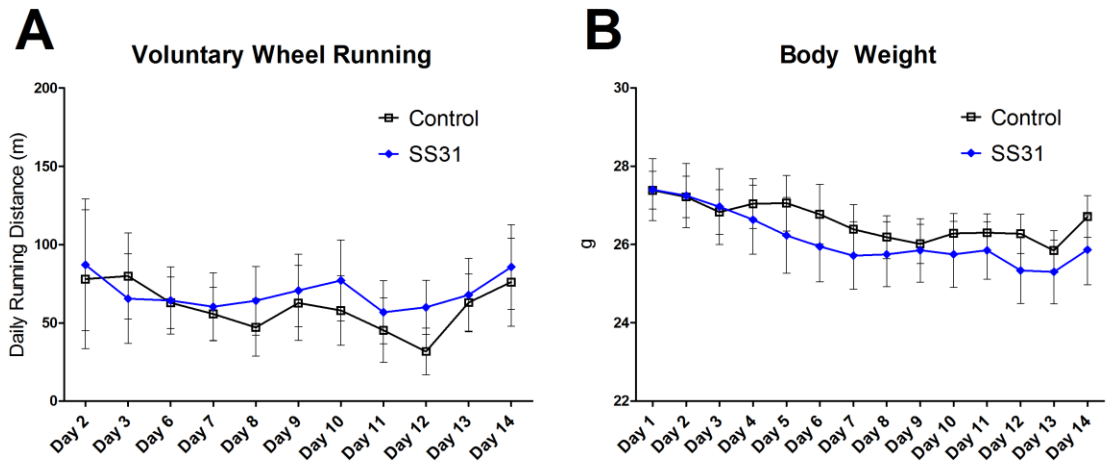

Figure 5.16. Daily SS31 treatment did not affect (A) voluntary running distance or (B) the gradual weight loss associated with daily exercise in old mice. Data presented as mean ±SEM. n = 6-7 per group. Day 1 is the first injection day when wheels were unlocked, so no distance data were recorded. Due to a software malfunction wheel data from days 4 and 5 were lost.

Voluntary Wheel Running Induced Energetic Benefits Similar to SS31

Following the two-week voluntary wheel running experiment, saline-treated mice were taken for in vivo spectroscopy to explore the possibility that the energetic benefits of regular exercise mimic the acute recovery that we observed following SS31 treatment. As illustrated in Fig. 5.17, voluntary exercise improved PCr/ATP ratio and ATPmax to a degree similar to SS31-treatment. Unlike SS31-treatment, however, P/O ratio was not different in exercised mice suggesting that these improvements in energy state and phosphorylation capacity were independent of mitochondrial phosphorylation efficiency.

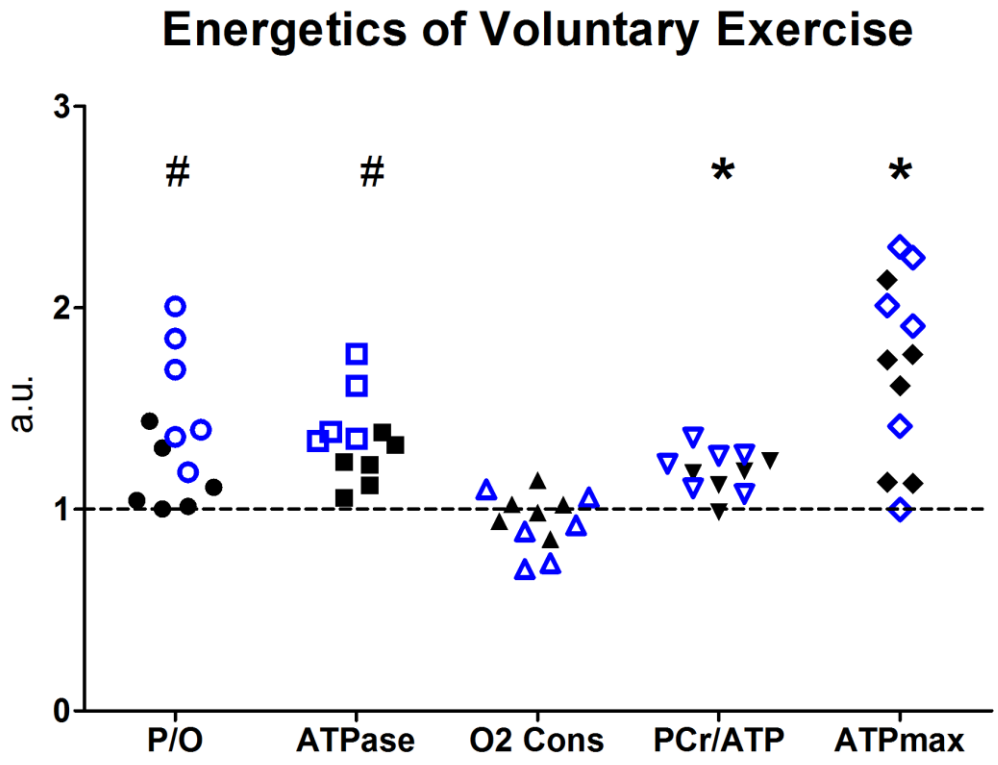

Figure 5.17. After two-weeks of voluntary wheel running, PCr/ATP and ATPmax were significantly improved in old mice and indistinguishable from SS31-treated mice. P/O ratio in exercised mice was lower than that of SS31-treated mice and indistinguishable from old controls. Values are normalized to old control average for each parameter. Closed black shapes (●...) represent voluntary wheel runners. Open blue shapes (○…) represent SS31-treated mice. Dashed line represents old control average. # $p<0.05$ wheel running vs. SS31, *$p<0.05$ wheel running vs. old control.

Discussion

In this chapter we demonstrate the reversal of depressed mitochondrial energetics in aged mice by acute treatment with the mitochondrial targeted peptide SS31. We used a unique in vivo approach to observe rapid changes in mitochondrial energetics and confirmed our findings using ex vivo analysis of respiration in permeabilized muscle fibers. Significantly, we observed improved in situ fatigue resistance and live endurance capacity in association with these energetic changes suggesting that improvement of mitochondrial function translates directly to improved physical ability in aged organisms. These phenomena occurred despite no change in mitochondrial protein expression, indicating that improvements were due to transient rescue of existing mitochondrial capacity by the shift in intracellular oxidative state associated with SS31 activity.

SS31 is a novel therapeutic peptide, imparting antioxidant benefits by reducing ROS production at the IMM where it localizes in high concentrations (170). Recent work has demonstrated the effectiveness of SS31 in treating hypertensive cardiomyopathy (36), disuse atrophy (112, 136), ischemia-reperfusion injury (172), high fat diet related oxidative stress (5), and neurodegeneration (102). Little attention has been paid, however, to the effect of SS31 on skeletal muscle metabolism in aged organisms. Increased oxidative stress associated with mitochondrial dysfunction is considered a major factor in the etiology of age-related skeletal muscle degeneration (33, 77), making the targeted mitigation of mitochondrial ROS production by SS31 a promising intervention.

Using a combined MR and optical spectroscopy approach we were in a unique position to assess metabolic changes on a timescale compatible with the rate at which SS31 clears from skeletal muscle tissue (Fig. 5.2) and before changes in mitochondrial content could occur (74). Thus, we measured mitochondria while they were being directly regulated by the presence of SS31 in vivo. Similarly, our ex

vivo approaches observed the rates of oxygen consumption or H_2O_2 emission in permeabilized muscle fibers in the presence of exogenous SS31.

SS31 improved in vivo and ex vivo coupling efficiency (↑P/O and ↓state 4 respiration, Figs. 5.7C and 5.11B, respectively), in vivo energy state (↑PCr/ATP, Fig. 5.9), and in vivo phosphorylation capacity (↑ATPmax, Fig. 5.10). These changes indicate a rapid reversal of depressed mitochondrial energetics in old mice by treatment with SS31. Unexpectedly, SS31-treatment also delayed the onset of PCr hydrolysis following induction of ischemia, suggesting that oxidative phosphorylation was able to persist at lower oxygen tensions in the presence of SS31 (Fig. 5.8). Elucidating the mechanism responsible for this observation is beyond the scope of this study and requires future attention. However the effectiveness of the related SS peptide, SS20, in preventing ischemia-reperfusion injury in heart despite lacking antioxidant properties (172), suggests that SS-peptides induce not yet understood functional changes under low-oxygen conditions.

We have previously reported reductions in P/O and PCr/ATP following acute treatment with the pro-oxidant paraquat in the absence of intrinsic mitochondrial changes (Chapter 3). This indicates that an increase in ROS and the associated oxidative shift in the intracellular environment reversibly depress mitochondrial energetics. As a result, paraquat treatment pushed young mitochondria towards an old energetic phenotype one day after treatment without signs of increased oxidative damage (Chapter 4). In this chapter we demonstrate the opposite effect. A reduction of ROS production (Fig. 5.4A) and the accompanying shift in oxidative state (Fig. 5.4B) improved mitochondrial energetics in old mice, returning them to a young energetic phenotype. Such a rapid reversal of depressed energetic function was not accompanied by changes in mitochondrial content as measured by ETC complex protein expression (Fig. 5.3) or intrinsic functional capacity as measured by state 3 respiration in permeabilized muscle fibers (Fig. 11A). Taken together, these results suggest that what is typically considered dysfunction in

old mitochondria is actually a condition of oxidative stress-associated damping rather than damage-associated loss of function. Thus, the oxidative state of the intracellular environment is exposed as a therapeutic target for rapid restoration of mitochondrial energetics in aged organisms.

Despite the in vivo energetic improvements that we observed with SS31 treatment in old mouse skeletal muscle, it would be possible that these changes did not manifest as improved physical performance at the whole-organism level. Such a situation would render these results interesting from a scientific perspective, but less exciting physiologically. Therefore, we tested the physiological significance of the energetic changes that we observed in old mice using measures of in situ muscle force and fatigue and whole body measures of endurance. In line with in vivo results, the TA muscle of old SS31-treated mice significantly resisted fatigue in situ (Fig. 5.12). Neither maximal tetanic force nor the force-frequency relationship changed with SS31 treatment in skeletal muscle in situ (Fig. 5.13), isolating mitochondria from the contractile apparatus and neuromuscular transmission, as SS31's site of action (127). However, potential cardiovascular modifications resulting from SS31 treatment cannot be ruled out from the study presented here. Thus future work using optical methods to assess tissue oxygenation and blood flow during contraction would increase confidence in the mitochondrial mechanism responsible for resistance to fatigue.

At the whole-organism level, SS31-treated mice exhibited superior endurance capacity during treadmill running and Rotarod assays (Figs. 5.14 and 5.15), drawing a connection from the oxidative state (reduced H_2O_2 emission and improved GSH/GSSG ratio), to the mitochondria (improved energetics), to the muscle (improved fatigue resistance), and finally to the whole body (improved exercise capacity). This finding is similar to one presented recently by Li et al., in which a targeted gene therapy approach to deliver catalase to mitochondria in neonatal mice and observed improved treadmill performance after 3 months (95). From a clinical standpoint SS31 has advantages over this approach due to its ease of delivery, quickness

in exerting an effect, and direct translatability for human use. From a scientific standpoint, one-hour treatment with SS31 more-clearly isolates the antioxidant mechanism responsible for improved endurance, as mice underwent 3 months of development in the presence of mitochondrial-targeted catalase which may have resulted in a population of functionally unique mitochondria.

Interestingly, SS31-treated mice did not run farther than untreated mice when given voluntary access to running wheels (Fig. 5.16). This finding helps to delineate skeletal muscle endurance from other benefits of SS31-treatment, as all endurance tests encompass both mental and physical components. Unlike forced treadmill running to exhaustion, this portion of the study tested an animal's motivation more than the limits of its endurance. So despite therapeutic benefits that SS31 has been reported to have on the nervous system of mice (31, 102, 192), such benefits do not include into an enhanced desire to exercise on the timescale of the study presented here.

We demonstrated similarities between SS31-treatment and the benefits of exercise in old organisms by measuring in vivo energetics in untreated mice following two weeks of voluntary treadmill running (Fig. 5.17). Regular exercise leads to numerous positive adaptations including increased mitochondrial biogenesis and antioxidant levels, and is often considered the best way to stave-off age-associated loss of skeletal muscle function (33, 81, 139, 183). Interestingly, two weeks of voluntary wheel running improved PCr/ATP ratio and ATPmax, similar to SS31-treatment, but did not affect P/O ratio. This suggests that mitochondrial biogenesis occurred over the two-week period leading to an increased phosphorylation capacity in exercised mice without any improvement in the oxidative environment or mitochondrial efficiency. This highlights ROS-mediated signaling as a parallel means for improving oxidative capacity. Unlike the modulation of mitochondrial efficiency through changes in the oxidative environment that we suggest here, this mechanism relies on oxidative stress to initiate signaling cascades responsible for mitochondrial biogenesis and other positive adaptations on a longer timescale (57, 144).

In conclusion, this chapter demonstrates the recovery of aged mitochondrial energetics with a single injection of SS31, in association with decreased ROS production and a more reduced oxidative environment. This capacity for rapid functional recovery supports the primary hypothesis of this dissertation, that what is typically considered age-related mitochondrial dysfunction is actually depressed function resulting from reversible modifications related to a shift in the oxidative environment. Significantly, the energetic improvements that we observed translate directly into enhanced physical capacity. These findings have important implications for the use of SS31 as a therapy for aged humans in the future.

Chapter 6

Conclusion

This dissertation presents the technical evolution of a non-invasive approach for measuring in vivo metabolism in mouse skeletal muscle. The methods foundation upon which this project is assembled was revolutionary in its own right, and expanded the window through which scientists could view the world of in vivo energetics (3, 105). The advances presented here widen this window to include a view of acute metabolic changes on a timescale compatible with many physiological phenomena. The value of this new view is demonstrated thorough an examination of the role of oxidative stress in regulating mitochondrial function during the aging process. This study built from a proof-of-principal (Chapter 3) to a demonstration of physiological relevance (Chapter 4) and culminated in the exploitation of the biological revelations for therapeutic benefit (Chapter 5).

Specifically, by combining in vivo magnetic resonance and optical spectroscopy approaches for studying in vivo energetics in mouse skeletal muscle the time it takes to acquire a complete set of in vivo data was reduced from over 24 hours to approximately one hour, endowing this noninvasive approach with the capacity to answer questions involving rapidly changing phenomena. One area of study that will benefit from such a capability is the pharmacodynamic profiling of drugs with known or suspected mitochondrial effects, which include anesthetics (114), targeted cancer therapies (71), and HIV-treatment drugs (149). Another area to benefit is the development of early biomarkers for disease or exposure to environmental toxins. From clinical and public health perspectives there are significant benefits to catching disease early, and this technique provides a method for detecting perturbations in mitochondrial energetics at an early state that may predate more obvious manifestations.

This technology also brings value to the study of chronic conditions, which were the target of the original single-mode spectroscopy approach. Significantly, it adds the ability to collect multiple data points over an extended period of time using a longitudinal study design. The value of this strategy in demonstrated in Chapter 2 (Fig. 2.10) as a longitudinal study demonstrated similarity between the effects of paraquat and repeat bouts of anesthetic over a three day period. The capacity should exist to conduct longer-term longitudinal studies, or studies of the effects of anesthesia which are relevant and interesting in their own right.

The present work addresses a highly relevant health problem by applying this new technology to a study of aging. A significant amount of aging research has been conducted during recent decades, providing a broad foundation of published work to frame research questions and drive study designs. Specifically, the mechanism by which oxidative stress contributes to the aging process has undergone a recent transformation from a traditional view involving macromolecular oxidative damage to a novel hypothesis involving more subtle functional modifications. Multi-modal spectroscopy provided a unique method to observe the in vivo response to modulations in the oxidative environment on a timescale that allowed meaningful conclusions to be drawn, unencumbered by adaptation or degeneration. To this end the effects of increased oxidative stress were measured after one day (Chapter 4) and the effects of reduced oxidative stress were measured after only one hour (Chapter 5).

This work contributes the new insight that mitochondrial coupling efficiency is sensitive to fluctuations in the oxidative environment in vivo. In Chapter 4 this sensitivity is demonstrated over a broad range of the mouse lifespan and a link is drawn from increased oxidative stress to energetic consequences that help explain common functional losses in old skeletal muscle. These findings shed doubt on the notion that oxidative damage is the source of age-related muscle degeneration. In Chapter 5 reversibility of

mitochondrial inefficiency is tested by treating old mice with the mitochondrial-targeted antioxidant SS31. By studying in vivo energetics before the antioxidant had cleared from skeletal muscle and before mitochondrial biogenesis or repair had time to compensate for pre-existing damage, the effect of reduced oxidative stress was isolated. Supporting the idea that age-related loss of function is reversible, mitochondrial energetics were rapidly improved by restoring the oxidative environment to that of a younger animal. Taken together these results support the view that age-related loss of mitochondrial function is related to a reversible shift in the oxidative environment rather than irreversible damage to mitochondrial components. This represents a new way of thinking about age-related degeneration and oxidative stress.

The in vivo, in situ, and whole-body effects of SS31 are particularly significant as they not only lend weight to a novel mechanism to explain age-related change, but also demonstrate an exciting recovery of muscle function in aged organisms. These findings have significant implications for the development of SS31 as a therapeutic intervention for humans in the future. Returning a degree of skeletal muscle function to elderly individuals would improve mobility and quality of life and reduce the physical and monetary burden on care givers and health care systems. Age is an inevitable consequence for all humans and the potential value of such a therapy cannot be understated.

One deficiency of the work presented here is that the non-invasive view of mitochondrial energetics does not provide insight into the mechanisms that underlie observed changes. For example, in Chapter 5 an association can be drawn between the presence of SS31 in muscle, recovery of the oxidative environment, improvement of in vivo energetics, and resulting benefits at the whole organism level. However, the mechanistic lines that connect these dots are not defined. While antioxidant benefits of SS31 have been established, the mechanism responsible for this benefit is poorly understood and SS31 may be responsible

for non-antioxidant related effects (172). Also, the transient modifications that allow oxidative stress to depress mitochondrial function in such a way that it can be recovered in as little as one hour are poorly understood. Ongoing research efforts by other groups examining the interaction between SS31 and cytochrome c and redox-sensitive post-translational modification of mitochondrial enzymes promise to have answers to these questions in the near future.

To keep pace with the increasing age of the human population, tools to help us understand the biology of aging and therapies to improve elderly quality of life must continue to evolve. The work presented here makes significant inroads toward both of these aims. Multi-modal spectroscopy provides unique insight into the in vivo biology of aging and can be used to approach questions in numerous mouse models of aging and disease. This project used this unique ability to support a shift in the understanding of depressed mitochondrial function in aging skeletal muscle and demonstrates a therapeutic benefit of this new way of thinking.

References

1. **Ababneh Z, Beloeil H, Berde CB, Gambarota G, Maier SE, and Mulkern RV**. Biexponential parameterization of diffusion and T2 relaxation decay curves in a rat muscle edema model: Decay curve components and water compartments. *Magnetic Resonance in Medicine* 54: 524-531, 2005.

2. **Alemayehu B, and Warner K**. The Lifetime Distribution of Health Care Costs. *Health Services Research* 39: 627-642, 2004.

3. **Amara C, Marcinek D, Shankland E, Schenkman K, Arakaki L, and Conley K**. Mitochondrial function in vivo: Spectroscopy provides window on cellular energetics. *Methods* 46: 312-318, 2008.

4. **Amara C, Shankland E, Jubrias S, Marcinek D, Kushmerick M, and Conley K**. Mild mitochondrial uncoupling impacts cellular aging in human muscles in vivo. *Proceedings of the National Academy of Science* 104: 1057-1062, 2007.

5. **Anderson E, Lustig M, Boyle K, Woodlief T, Kane D, Lin C, Price JI, Kang L, Rabinovitch P, Szeto H, Houmard J, Cortright R, Wasserman D, and Neufer P**. Mitochondrial H2O2 emission and cellular redox state link excess fat intake to insulin resistance in both rodents and humans. *The Journal of Clinical Investigation* 119: 573-581, 2009.

6. **Anderson E, Yamazaki H, and Neufer P**. Induction of Endogenous Uncoupling Protein 3 Suppresses Mitochondrial Oxidant Emission during Fatty Acid-supported Respiration. *The Journal of Biochemistry* 282: 31257-31266, 2007.

7. **Anderson R, Barger J, Edwards M, Braun K, O'Connor C, Prolla T, and Weindruch R**. Dynamic regulation of PGC-1α localization and turnover implicates mitochondrial adaptation in calorie restriction and the stress response. *Aging Cell* 7: 101-111, 2008.

8. **Antonini E, and Brunori M**. *Hemoglobin and myoglobin in their reactions with ligands*. North-Holland Pub. Co., 1971.

9. **Arakaki L, and Burns D**. Multispectral Analysis for Quantitative Measurements of Myoglobin Oxygen Fractional Saturation in the Presence of Hemoglobin Interference. *Applied Spectroscopy* 46: 1919-1928, 1992.

10. **Arakaki L, Burns D, and Kushmerick M**. Accurate Myoglobin Oxygen Saturation by Optical Spectroscopy Measured in Blood-Perfused Rat Muscle. *Applied Spectroscopy* 61: 978-985, 2007.

11. **Arakaki L, Ciesielski W, Thackray B, Feigl E, and Schenkman K**. Simultaneous Optical Spectroscopic Measurement of Hemoglobin and Myoglobin Saturations and Cytochrome aa3 Oxidation In Vivo. *Applied Spectroscopy* 64: 973-979, 2010.

12. **Arakaki L, Kushmerick M, and Burns D**. Myoglobin Oxygen Saturation Measured Independently of Hemoglobin in Scattering Media by Optical Reflectance Spectroscopy. *Applied Spectroscopy* 50: 697-707, 1996.

13. **Arias E**. United States Life Tables, 2007. *National Vital Statistics Reports* 59: 1-61, 2011.

14. **Barbieri E, and Sestili P**. Reactive oxygen species in skeletal muscle signaling. *J Signal Transduct* 2012: 982794, 2012.

15. **Bevilacqua L, Seifert E, Estey C, Gerrits M, and Harper M**. Absence of uncoupling protein-3 leads to greater activation of an adenine nucleotide translocase-mediated proton conductance in skeletal muscle mitochondria from calorie restricted mice. *Biochimica et Biophysica Acta* 1797: 1389-1397, 2010.

16. **Blei ML, Conley KE, and Kushmerick MJ**. Separate measures of ATP utilization and recovery in human skeletal muscle. *The Journal of Physiology* 465: 203-222, 1993.

17. **Bolster DR, Crozier SJ, Kimball SR, and Jefferson LS**. AMP-activated Protein Kinase Suppresses Protein Synthesis in Rat Skeletal Muscle through Down-regulated Mammalian Target of Rapamycin (mTOR) Signaling. *Journal of Biological Chemistry* 277: 23977-23980, 2002.

18. **Bourgeois JM, and Tarnopolsky MA**. Pathology of skeletal muscle in mitochondrial disorders. *Mitochondrion* 4: 441-452, 2004.

19. **Brand M**. The efficiency and plasticity of mitochondrial energy transduction. *Biochemical Society Transactions* 33: 897-904, 2005.

20. **Brand M**. Uncoupling to survive? The role of mitochondrial inefficiency in ageing. *Experimental Gerontology* 35: 811-820, 2000.

21. **Brand MD, and Nicholls DG**. Assessing mitochondrial dysfunction in cells. *Biochemical Journal* 435: 297-312, 2011.

22. **Brand MD, Pakay JL, Ocloo A, Kokoszka J, Wallace DC, Brookes PS, and Cornwall EJ**. The basal proton conductance of mitochondria depends on adenine nucleotide translocase content. *Biochem J* 392: 353-362, 2005.

23. **Brookes P, Levonen A, Shiva S, Sarti P, and Darley-Usmar V**. Mitochondria: Regulators of Signal Transduction by Reactive Oxygen and Nitrogen Species. *Free Radical Biology & Medicine* 33: 755-764, 2002.

24. **Brookes P, Yoon Y, Robotham J, Anders M, and Sheu S**. Calcium, ATP, and ROS: a mitochondrial love-hate triangle. *American Journal of Physiology - Cell Physiology* 287: C817-C833, 2004.

25. **Cabo RD, Burgess J, and Navas P**. Adaptations to oxidative stress induced by vitamin E deficiency in rat liver. *Journal of Bioenergetics and Biomembranes* 38: 309-317, 2006.

26. **Calabrese V, Scapagnini G, Giuffrida Stella A, Bates T, and Clark J**. Mitochondrial involvement in brain function and dysfunction: relevance to aging, neurodegenerative disorders and longevity. *Neurochemical Research* 26: 739-764, 2001.

27. **Carpenter C, Pogue B, Jiang S, Dehghani H, Wang X, Paulsen K, Wells W, Forero J, Kogel C, Weaver J, Poplack S, and Kaufman P**. Image-guided optical spectroscopy provides molecular-specific information in vivo: MRI-guided spectroscopy of breast cancer hemoglobin, water, and scatterer size. *Optics Letters* 32: 933-935, 2007.

28. **Carreras MC, and Poderoso JJ**. Mitochondrial nitric oxide in the signaling of cell integrated responses. *American Journal of Physiology - Cell Physiology* 292: C1569-C1580, 2007.

29. **Chaturvedi R, and Beal M**. Mitochondrial approaches for neuroprotection. *Annals of the New York Academy of Sciences* 1147: 395-412, 2008.

30. **Chen L, Xu B, Liu L, Luo Y, Yin J, Zhou H, Chen W, Shen T, Han X, and Huang S**. Hydrogen peroxide inhibits mTOR signaling by activation of AMPKalpha leading to apoptosis of neuronal cells. *Lab Invest* 90: 762-773, 2010.

31. **Cho S, Szeto HH, Kim E, Kim H, Tolhurst AT, and Pinto JT**. A Novel Cell-permeable Antioxidant Peptide, SS31, Attenuates Ischemic Brain Injury by Down-regulating CD36. *Journal of Biological Chemistry* 282: 4634-4642, 2007.

32. **Cocheme H, and Murphy M**. Complex I Is the Major Site of Mitochondrial Superoxide Production by Paraquat. *The Journal of Biological Chemistry* 283: 1786-1798, 2008.

33. **Conley K, Jubrias S, Amara C, and Marcinek D**. Mitochondrial dysfunction: impact on exercise performance and cellular aging. *Exercise and Sport Science Reviews* 35: 43-49, 2007.

34. **Conley K, Jubrias S, and Esselman P**. Oxidative capacity and ageing in human muscle. *Journal of Physiology* 526: 203-210, 2000.

35. **Cortopassi GA, Shibata D, Soong NW, and Arnheim N**. A pattern of accumulation of a somatic deletion of mitochondrial DNA in aging human tissues. *Proc Natl Acad Sci U S A* 89: 7370-7374, 1992.

36. **Dai D-F, Chen T, Szeto H, Nieves-Cintrón M, Kutyavin V, Santana LF, and Rabinovitch PS**. Mitochondrial Targeted Antioxidant Peptide Ameliorates Hypertensive Cardiomyopathy. *Journal of the American College of Cardiology* 58: 73-82, 2011.

37. **Dai D, Chen T, Wanagat J, Laflamme M, Marcinek D, Emond M, Ngo C, Prolla T, and Rabinovitch P**. Age-dependent cardiomyopathy in mitochondrial mutator mice is attenuated by overexpression of catalase targeted to mitochondria. *Aging Cell* 9: 536-544, 2010.

38. **Dai DF, Santana LF, Vermulst M, Tomazela DM, Emond MJ, MacCoss MJ, Gollahon K, Martin GM, Loeb LA, Ladiges WC, and Rabinovitch PS**. Overexpression of catalase targeted to mitochondria attenuates murine cardiac aging. *Circulation* 119: 2789-2797, 2009.

39. **Davies SMK, Poljak A, Duncan MW, Smythe GA, and Murphy MP**. Measurements of protein carbonyls, ortho- and meta-tyrosine and oxidative phosphorylation complex activity in mitochondria from young and old rats. *Free Radical Biology and Medicine* 31: 181-190, 2001.

40. **Dey M, Breeze R, Hayton W, Karara A, and Krieger R**. Paraquat Pharmacokinetics Using a Subcutaneous Toxid Low Dose in the Rat. *Fundamental and Applied Toxicology* 14: 208-216, 1990.

41. **Drabkin DL, With the technical assistance of Priscilla Fourer JMF, Anna May Dych, Charlotte Glauser,, and Randall J**. The Distribution of the Chromoproteins, Hemoglobin, Myoglobin, and Cytochrome C, in the Tissues of Different Species, and the Relationship of the Total Content of Each Chromoprotein to Body Mass. *Journal of Biological Chemistry* 182: 317-334, 1950.

42. **Drew R, and Gram TE**. Vehicle alteration of paraquat lethality in mice. *Toxicol Appl Pharmacol* 48: 479-487, 1979.

43. **Du ZX, Zhang HY, Meng X, Guan Y, and Wang HQ**. Role of oxidative stress and intracellular glutathione in the sensitivity to apoptosis induced by proteasome inhibitor in thyroid cancer cells. *BMC Cancer* 9: 56, 2009.

44. **Dzeja P, and Terzic A**. Adenylate Kinase and AMP Signaling Networks: Metabolic Monitoring, Signal Communication and Body Energy Sensing. *International Journal of Molecular Sciences* 10: 1729-1772, 2009.

45. **Echtay K**. Mitochondrial uncoupling proteins - What is their physiological role? *Free Radical Biology & Medicine* 43: 1351-1371, 2007.

46. **Echtay K, Esteves T, Pakay J, Jekabsons M, Lambert A, Portero-Otin M, Pamplona R, Vidal-Puig A, Wang S, Roebuck S, and Brand M**. A signalling role for 4-hydroxy-2-nonenal in regulation of mitochondrial uncoupling. *The EMBO Journal* 22: 4103-4110, 2003.

47. **Echtay K, Roussel D, St-Pierre J, Jekabsons M, Cadenas S, Stuart J, Harper J, Roebuck S, Morrison A, Pickering S, Clapham J, and Brand M**. Superoxide activates mitochondrial uncoupling proteins. *Nature* 415: 96-99, 2002.

48. **Echtay KS, Pakay JL, Esteves TC, and Brand MD**. Hydroxynonenal and uncoupling proteins: a model for protection against oxidative damage. *Biofactors* 24: 119-130, 2005.

49. **Ellington W**. Evolution and physiological roles of phosphagen systems. *Annual Review of Physiology* 63: 289-325, 2001.

50. **Flock ST, Jacques SL, Wilson BC, Star WM, and van Gemert MJC**. Optical properties of intralipid: A phantom medium for light propagation studies. *Lasers in Surgery and Medicine* 12: 510-519, 1992.

51. **Forbes SC, Paganini AT, Slade JM, Towse TF, and Meyer RA**. Phosphocreatine recovery kinetics following low- and high-intensity exercise in human triceps surae and rat posterior hindlimb muscles. *American Journal of Physiology - Regulatory, Integrative and Comparative Physiology* 296: R161-R170, 2009.

52. **Franco AA, Odom RS, and Rando TA**. Regulation of antioxidant enzyme gene expression in response to oxidative stress and during differentiation of mouse skeletal muscle. *Free Radical Biology and Medicine* 27: 1122-1132, 1999.

53. **Gibson GE, Starkov A, Blass JP, Ratan RR, and Beal MF**. Cause and consequence: Mitochondrial dysfunction initiates and propagates neuronal dysfunction, neuronal death and behavioral abnormalities in age-associated neurodegenerative diseases. *Biochimica et Biophysica Acta (BBA) - Molecular Basis of Disease* 1802: 122-134, 2010.

54. **Gnaiger E**. Capacity of oxidative phosphorylation in human skeletal muscle: New perspectives of mitochondrial physiology. *The International Journal of Biochemistry & Cell Biology* 41: 1837-1845, 2009.

55. **Gnaiger E**. Capacity of oxidative phosphorylation in human skeletal muscle: new perspectives of mitochondrial physiology. *Int J Biochem Cell Biol* 41: 1837-1845, 2009.

56. **Golding E, Teague W, and Dobson G**. Adjustment of K' to varying pH and pMg for the creatine kinase, adenylate kinase and ATP hydrolysis equilibria permitting quantitative bioenergetic assessment. *J Exp Biol* 198: 1775-1782, 1995.

57. **Gomez-Cabrera M, Domenech E, Romagnoli M, Arduini A, Borras C, Pallardo F, Sastre J, and Vina J**. Oral administration of vitamin C decreases muscle mitochondrial biogenesis and hampers training-induced adaptations in endurance performance. *The American Journal of Clinical Nutrition* 87: 142-149, 2008.

58. **Gong D, Monemdjou S, Gavrilova O, Leon L, Marcus-Samuels B, Chou C, Everett C, Kozak L, Li C, Deng C, Harper M, and Reitman M**. Lack of Obesity and Normal Response to Fasting and Thyroid Hormone in Mice Lacking Uncoupling Protein-3. *The Journal of Biological Chemistry* 275: 16251-16257, 2000.

59. **Haaland DM, and Thomas EV**. Partial least-squares methods for spectral analyses. 1. Relation to other quantitative calibration methods and the extraction of qualitative information. *Analytical Chemistry* 60: 1193-1202, 1988.

60. **Hajnóczky G, Csordás G, Das S, Garcia-Perez C, Saotome M, Sinha Roy S, and Yi M**. Mitochondrial calcium signalling and cell death: Approaches for assessing the role of mitochondrial Ca2+ uptake in apoptosis. *Cell Calcium* 40: 553-560, 2006.

61. **Haller T, Ortner M, and Gnaiger E**. A Respirometer for Investigating Oxidative Cell Metabolism: Toward Optimization of Respiratory Studies. *Analytical Biochemistry* 218: 338-342, 1994.

62. **Han E-S, Muller FL, Pérez VI, Qi W, Liang H, Xi L, Fu C, Doyle E, Hickey M, Cornell J, Epstein CJ, Roberts LJ, Van Remmen H, and Richardson A**. The in vivo gene expression signature of oxidative stress. *Physiological Genomics* 34: 112-126, 2008.

63. **Han Z, Varadharaj S, Giedt RJ, Zweier JL, Szeto HH, and Alevriadou BR**. Mitochondria-Derived Reactive Oxygen Species Mediate Heme Oxygenase-1 Expression in Sheared Endothelial Cells. *Journal of Pharmacology and Experimental Therapeutics* 329: 94-101, 2009.

64. **Harman D**. Aging: a theory based on free radical and radiation chemistry. *J Gerontol* 11: 298-300, 1956.

65. **Harman D**. The biologic clock: the mitochondria? *Journal of the American Geriatrics Society* 20: 145-147, 1972.

66. **Harper JA, Stuart JA, Jekabsons MB, Roussel D, Brindle KM, Dickinson K, Jones RB, and Brand MD**. Artifactual uncoupling by uncoupling protein 3 in yeast mitochondria at the concentrations found in mouse and rat skeletal-muscle mitochondria. *Biochem J* 361: 49-56, 2002.

67. **Harper M, Green K, and Brand M**. The Efficiency of Cellular Energy Transduction and Its Implications for Obesity. *Annual Review of Nutrition* 28: 13-33, 2008.

68. **Harper ME, Bevilacqua L, Hagopian K, Weindruch R, and Ramsey JJ**. Ageing, oxidative stress, and mitochondrial uncoupling. *Acta Physiologica Scandinavica* 182: 321-331, 2004.

69. **Hatakenaka M, Ueda M, Ishigama K, Otsuka M, and Masuda K**. Effects of aging on muscle T2 relaxation time: difference between fast- and slow-twitch muscles. *Investigative Radiology* 36: 692-698, 2001.

70. **Heineman FW, Eng J, Berkowitz BA, and Balaban RS**. NMR spectral analysis of kinetic data using natural lineshapes. *Magn Reson Med* 13: 490-497, 1990.

71. **Hilf R**. Mitochondria are targets of photodynamic therapy. *J Bioenerg Biomembr* 39: 85-89, 2007.

72. **Hinerfeld D, Traini MD, Weinberger RP, Cochran B, Doctrow SR, Harry J, and Melov S**. Endogenous mitochondrial oxidative stress: neurodegeneration, proteomic analysis, specific respiratory chain defects, and efficacious antioxidant therapy in superoxide dismutase 2 null mice. *J Neurochem* 88: 657-667, 2004.

73. **Hollander J, Bejma J, Ookawara T, Ohno H, and Ji LL**. Superoxide dismutase gene expression in skeletal muscle: fiber-specific effect of age. *Mechanisms of Ageing and Development* 116: 33-45, 2000.

74. **Hood DA**. Invited Review: Contractile activity-induced mitochondrial biogenesis in skeletal muscle. *Journal of Applied Physiology* 90: 1137-1157, 2001.

75. **Hutter E, Unterluggauer H, Garedew A, Jansen-Durr P, and Gnaiger E**. High-resolution respirometry - a modern tool in aging research. *Experimental Gerontology* 41: 103-109, 2006.

76. **Jackson MJ, Pye D, and Palomero J**. The production of reactive oxygen and nitrogen species by skeletal muscle. *Journal of Applied Physiology* 102: 1664-1670, 2007.

77. **Jang Y, Lustgarten M, Liu Y, Muller F, Bhattacharya A, Liang H, Salmon A, Brooks S, Larkin L, Hayworth C, Richardson A, and Remmen HV**. Increased superoxide in vivo accelerates age-associated muscle atrophy through mitochondrial dysfunction and neuromuscular junction degeneration. *The FASEB Journal* 24: 1376-1390, 2010.

78. **Jang YC, Pérez VI, Song W, Lustgarten MS, Salmon AB, Mele J, Qi W, Liu Y, Liang H, Chaudhuri A, Ikeno Y, Epstein CJ, Van Remmen H, and Richardson A**. Overexpression of Mn Superoxide Dismutase Does Not Increase Life Span in Mice. *The Journals of Gerontology Series A: Biological Sciences and Medical Sciences* 64A: 1114-1125, 2009.

79. **Jeneson JAL, Schmitz JPJ, van den Broek NMA, van Riel NAW, Hilbers PAJ, Nicolay K, and Prompers JJ**. Magnitude and control of mitochondrial sensitivity to ADP. *American Journal of Physiology - Endocrinology and Metabolism* 297: E774-E784, 2009.

80. **Jones DP**. Radical-free biology of oxidative stress. *American Journal of Physiology - Cell Physiology* 295: C849-C868, 2008.

81. **Jørgensen SB, Richter EA, and Wojtaszewski JFP**. Role of AMPK in skeletal muscle metabolic regulation and adaptation in relation to exercise. *The Journal of Physiology* 574: 17-31, 2006.

82. **Kamo N, Muratsugu M, Hongoh R, and Kobatake Y**. Membrane potential of mitochondria measured with an electrode sensitive to tetraphenyl phosphonium and relationship between proton electrochemical potential and phosphorylation potential in steady state. *J Membr Biol* 49: 105-121, 1979.

83. **Karatzaferi C, De Haan A, Offringa C, and Sargeant AJ**. Improved high-performance liquid chromatographic assay for the determination of "high-energy" phosphates in mammalian skeletal muscle. Application to a single-fibre study in man. *J Chromatogr B Biomed Sci Appl* 730: 183-191, 1999.

84. **Kelly OM, McNamara YM, Manzke LH, Meegan MJ, and Porter RK**. The preservation of in vivo phosphorylated and activated uncoupling protein 3 (UCP3) in isolated skeletal muscle mitochondria following administration of 3,4-methylenedioxymethamphetamine (MDMA aka ecstasy) to rats/mice. *Mitochondrion* 12: 110-119, 2012.

85. **Kemp G, Meyerspeer M, and Moser E**. Absolute quantification of phosphorus metabolite concentrations in human muscle in vivo by 31P MRS: a quantitative review. *NMR In Biomedicine* 20: 555-565, 2007.

86. **Kerner J, Turkaly PJ, Minkler PE, and Hoppel CL**. Aging skeletal muscle mitochondria in the rat: decreased uncoupling protein-3 content. *American Journal of Physiology - Endocrinology and Metabolism* 281: E1054-E1062, 2001.

87. **Koh HJ, Toyoda T, Fujii N, Jung MM, Rathod A, Middelbeek RJ, Lessard SJ, Treebak JT, Tsuchihara K, Esumi H, Richter EA, Wojtaszewski JF, Hirshman MF, and Goodyear LJ**. Sucrose nonfermenting AMPK-related kinase (SNARK) mediates contraction-stimulated glucose transport in mouse skeletal muscle. *Proc Natl Acad Sci U S A* 107: 15541-15546, 2010.

88. **Korshunov SS, Skulachev VP, and Starkov AA**. High protonic potential actuates a mechanism of production of reactive oxygen species in mitochondria. *FEBS Letters* 416: 15-18, 1997.

89. **Kupriyanov VV, Dai G, Shaw RA, Sun J, Jilkina O, Luo Z, Mantsch H, and Deslauriers R**. Noninvasive assessment of cardiac ischemic injury using 87Rb and 23Na MR imaging, 31P MR, and optical spectroscopy. *Magnetic Resonance in Medicine* 44: 899-908, 2000.

90. **Kushmerick M**. Energy balance in muscle activity: Simulations of ATPase coupled to oxidative phosphorylation and to creatine kinase. *Comparative Biochemistry and Physiology Part B: Biochemistry and Molecular Biology* 120: 109-123, 1998.

91. **Kushmerick MJ**. Multiple equilibria of cations with metabolites in muscle bioenergetics. *American Journal of Physiology - Cell Physiology* 272: C1739-C1747, 1997.

92. **Lang T, Streeper T, Cawthon P, Baldwin K, Taaffe D, and Harris T**. Sarcopenia: etiology, clinical consequences, intervention, and assessment. *Osteoporosis International* 21: 543-559, 2010.

93. **Lanza IR, Befroy DE, and Kent-Braun JA**. Age-related changes in ATP-producing pathways in human skeletal muscle in vivo. *Journal of Applied Physiology* 99: 1736-1744, 2005.

94. **Lanza IR, Tevald MA, Befroy DE, and Kent-Braun JA**. Intracellular energetics and critical Po2 in resting ischemic human skeletal muscle in vivo. *American Journal of Physiology - Regulatory, Integrative and Comparative Physiology* 299: R1415-R1422, 2010.

95. **Li D, Lai Y, Yue Y, Rabinovitch PS, Hakim C, and Duan D**. Ectopic Catalase Expression in Mitochondria by Adeno-Associated Virus Enhances Exercise Performance in Mice. *PLOS ONE* 4: e6673, 2009.

96. **Li X-D, Rebrin I, Forster MJ, and Sohal RS**. Effects of age and caloric restriction on mitochondrial protein oxidative damage in mice. *Mechanisms of Ageing and Development* 133: 30-36, 2012.

97. **Ljubicic V, and Hood DA**. Diminished contraction-induced intracellular signaling towards mitochondrial biogenesis in aged skeletal muscle. *Aging Cell* 8: 394-404, 2009.

98. **Mahler M, Louy C, Homsher E, and Peskoff A**. Reappraisal of diffusion, solubility, and consumption of oxygen in frog skeletal muscle, with applications to muscle energy balance. *J Gen Physiol* 86: 105-134, 1985.

99. **Mailloux RJ, Adjeitey CN-K, Xuan JY, and Harper M-E**. Crucial yet divergent roles of mitochondrial redox state in skeletal muscle vs. brown adipose tissue energetics. *The FASEB Journal* 2011.

100. **Mailloux RJ, and Harper M-E**. Uncoupling proteins and the control of mitochondrial reactive oxygen species production. *Free Radical Biology and Medicine* 51: 1106-1115, 2011.

101. **Mailloux RJ, Seifert EL, Bouillaud F, Aguer C, Collins S, and Harper M-E**. Glutathionylation Acts as a Control Switch for Uncoupling Proteins UCP2 and UCP3. *Journal of Biological Chemistry* 286: 21865-21875, 2011.

102. **Manczak M, Mao P, Calkins MJ, Cornea A, Reddy AP, Murphy MP, Szeto HH, Park B, and Reddy PH**. Mitochondria-Targeted Antioxidants Protect Against Amyloid-β Toxicity in Alzheimer's Disease Neurons. *Journal of Alzheimer's Disease* 20: 609-631, 2010.

103. **Marcinek D, Ciesielski W, Conley K, and Schenkman K**. Oxygen regulation and limitation to cellular respiration in mouse skeletal muscle in vivo. *Americal Journal of Physiology - Heart and Circulatory Physiology* 285: H1900-H1908, 2003.

104. **Marcinek D, Kushmerick M, and Conley K**. Lactic acidosis in vivo: testing the link between lactate generation and H+ accumulation in ischemic mouse muscle. *Journal of Applied Physiology* 108: 1479-1486, 2010.

105. **Marcinek D, Schenkman K, Ciesielski W, and Conley K**. Mitochondrial coupling in vivo in mouse skeletal muscle. *The American Journal of Cell Physiology* 286: C457-C463, 2004.

106. **Marcinek D, Schenkman K, Ciesielski W, Lee D, and Conley K**. Reduced mitochondrial coupling in vivo alters cellular energetics in aged mouse skeletal muscle. *Journal of Physiology* 569: 467-473, 2005.

107. **Marzetti E, and Leeuwenburgh C**. Skeletal muscle apoptosis, sarcopenia and frailty at old age. *Experimental Gerontology* 41: 1234-1238, 2006.

108. **McConnachie LA, Mohar I, Hudson FN, Ware CB, Ladiges WC, Fernandez C, Chatterton-Kirchmeier S, White CC, Pierce RH, and Kavanagh TJ**. Glutamate Cysteine Ligase Modifier Subunit Deficiency and Gender as Determinants of Acetaminophen-Induced Hepatotoxicity in Mice. *Toxicological Sciences* 99: 628-636, 2007.

109. **McLain AL, Szweda PA, and Szweda LI**. α-Ketoglutarate dehydrogenase: A mitochondrial redox sensor. *Free Radical Research* 45: 29-36, 2011.

110. **Meyer R**. Linear dependence of muscle phosphocreatine kinetics on total creatine content. *Americal Journal of Physiology* 257: C1149-C1157, 1989.

111. **Meyer RA, Kuchmerick MJ, and Brown TR**. Application of 31P-NMR spectroscopy to the study of striated muscle metabolism. *American Journal of Physiology - Cell Physiology* 242: C1-C11, 1982.

112. **Min K, Smuder AJ, Kwon O-s, Kavazis AN, Szeto HH, and Powers SK**. Mitochondrial-targeted antioxidants protect the skeletal muscle against immobilization-induced muscle atrophy. *Journal of Applied Physiology* 2011.

113. **Mitchell P**. Chemiosmotic coupling in oxidative and photosynthetic phosphorylation. *Biol Rev Camb Philos Soc* 41: 445-502, 1966.

114. **Morgan PG, Hoppel CL, and Sedensky MM**. Mitochondrial Defects and Anesthetic Sensitivity. *Anesthesiology* 96: 1268-1270, 2002.

115. **Morrow JD, and Roberts LJ, 2nd**. Mass spectrometric quantification of F2-isoprostanes in biological fluids and tissues as measure of oxidant stress. *Methods Enzymol* 300: 3-12, 1999.

116. **Muller F, Lustgarten M, Jang Y, Richardson A, and Remmen HV**. Trends in oxidative aging theories. *Free Radical Biology & Medicine* 43: 477-503, 2007.

117. **Muller F, Song W, Liu Y, Chaudhuri A, Pieke-Dahl S, Strong R, Huang T, Epstein C, II LR, Csete M, Faulkner J, and Remmen HV**. Absence of CuZn superoxide dismutase leads to elevated oxidative stress and acceleration of age-dependent skeletal muscle atrophy. *Free Radical Biology & Medicine* 40: 1993-2004, 2006.

118. **Murkin JM, and Arango M**. Near-infrared spectroscopy as an index of brain and tissue oxygenation. *British Journal of Anaesthesia* 103: i3-i13, 2009.

119. **Murphy M, Echtay K, Blaikie F, Asin-Cayuela J, Cocheme H, Green K, Buckingham J, Taylor E, Hurrell F, Hughes G, Miwa S, Cooper C, Svistunenko D, Smith R, and Brand M**. Superoxide Activates Uncoupling Proteins by Generating Carbon-centered Radicals and Initiating Lipid Peroxidation. *The Journal of Biological Chemistry* 278: 48534-48545, 2003.

120. **Nabben M, Hoeks J, Briedé JJ, Glatz JFC, Moonen-Kornips E, Hesselink MKC, and Schrauwen P**. The effect of UCP3 overexpression on mitochondrial ROS production in skeletal muscle of young versus aged mice. *FEBS Letters* 582: 4147-4152, 2008.

121. **Nicholls D**. Mitochondrial membrane potential and aging. *Aging Cell* 3: 35-40, 2004.

122. **Nicholls DG, and Ferguson SJ**. *Bioenergetics*. London: Academic Press, 2002.

123. **Paganini A, Foley J, and Meyer R**. Linear dependence of muscle phosphocreatine kinetics on oxidative capacity. *Americal Journal of Physiology* 272: C501-C510, 1997.

124. **Papa S**. Mitochondrial oxidative phosphorylation changes in the life span. Molecular aspects and physiopathological implications. *Biochimica et Biophysica Acta (BBA) - Bioenergetics* 1276: 87-105, 1996.

125. **Parker N, Affourtit C, Vidal-Puig A, and Brand MD**. Energization-dependent endogenous activation of proton conductance in skeletal muscle mitochondria. *Biochem J* 412: 131-139, 2008.

126. **Percival J, Anderson K, Huang P, Adams M, and Froehner S**. Golgi and sarcolemmal neuronal NOS differentially regulate contraction-induced fatigue and vasoconstriction in exercising mouse skeletal muscle. *The Journal of Clinical Investigation* 120: 816-826, 2010.

127. **Percival JM, Anderson KNE, Gregorevic P, Chamberlain JS, and Froehner SC**. Functional Deficits in nNOSμ-Deficient Skeletal Muscle: Myopathy in nNOS Knockout Mice. *PLOS ONE* 3: e3387, 2008.

128. **Pérez VI, Van Remmen H, Bokov A, Epstein CJ, Vijg J, and Richardson A**. The overexpression of major antioxidant enzymes does not extend the lifespan of mice. *Aging Cell* 8: 73-75, 2009.

129. **Perry CGR, Kane DA, Lin CT, Kozy R, Cathey BL, Lark DS, Kane CL, Brophy PM, Gavin TP, Anderson EJ, and Neufer PD**. Inhibiting myosin-ATPase reveals a dynamic range of mitochondrial respiratory control in skeletal muscle. *Biochemical Journal* 437: 215-222, 2011.

130. **Petersen KF, Befroy D, Dufour S, Dziura J, Ariyan C, Rothman DL, DiPietro L, Cline GW, and Shulman GI**. Mitochondrial Dysfunction in the Elderly: Possible Role in Insulin Resistance. *Science* 300: 1140-1142, 2003.

131. **Picard M, Ritchie D, Thomas MM, Wright KJ, and Hepple RT**. Alterations in intrinsic mitochondrial function with aging are fiber type-specific and do not explain differential atrophy between muscles. *Aging Cell* 10: 1047-1055, 2011.

132. **Picard M, Taivassalo T, Ritchie D, Wright KJ, Thomas MM, Romestaing C, and Hepple RT**. Mitochondrial Structure and Function Are Disrupted by Standard Isolation Methods. *PLOS ONE* 6: e18317, 2011.

133. **Pollack M, Phaneuf S, Dirks A, and Leeuwenburgh C**. The Role of Apoptosis in the Normal Aging Brain, Skeletal Muscle, and Heart. *Annals of the New York Academy of Sciences* 959: 93-107, 2002.

134. **Ponticos M, Lu QL, Morgan JE, Hardie DG, Partridge TA, and Carling D**. Dual regulation of the AMP-activated protein kinase provides a novel mechanism for the control of creatine kinase in skeletal muscle. *EMBO J* 17: 1688-1699, 1998.

135. **Powers S, and Jackson M**. Exercise-Induced Oxidative Stress: Cellular Mechanisms and Impact on Muscle Force Production. *Physiology Review* 88: 1243-1276, 2008.

136. **Powers SK, Hudson MB, Nelson WB, Talbert EE, Min K, Szeto HH, Kavazis AN, and Smuder AJ**. Mitochondria-targeted antioxidants protect against mechanical ventilation-induced diaphragm weakness*. *Critical Care Medicine* 39: 1749-1759 1710.1097/CCM.1740b1013e3182190b3182162, 2011.

137. **Prior BM, Ploutz-Snyder LL, Cooper TG, and Meyer RA**. Fiber type and metabolic dependence of T2 increases in stimulated rat muscles. *Journal of Applied Physiology* 90: 615-623, 2001.

138. **Pryor W**. Oxy-Radicals and Related Species: Their Formation, Lifetimes, and Reactions. *Annual Review of Physiology* 48: 657-667, 1986.

139. **Radak Z, Chung H, and Goto S**. Exercise and hormesis: oxidative stress-related adaptation for successful aging. *Biogerontology* 6: 71-75, 2005.

140. **Rasbach K, and Schnellmann R**. Signaling of Mitochondrial Biogenesis following Oxidant Injury. *The Journal of Biological Chemistry* 282: 2355-2362, 2007.

141. **Rebrin I, and Sohal RS**. Pro-oxidant shift in glutathione redox state during aging. *Advanced Drug Delivery Reviews* 60: 1545-1552, 2008.

142. **Remmen HV, and Richardson A**. Oxidative damage to mitochondria and aging. *Experimental Gerontology* 36: 957-968, 2001.

143. **Reznick RM, Zong H, Li J, Morino K, Moore IK, Yu HJ, Liu Z-X, Dong J, Mustard KJ, Hawley SA, Befroy D, Pypaert M, Hardie DG, Young LH, and Shulman GI**. Aging-Associated Reductions in AMP-Activated Protein Kinase Activity and Mitochondrial Biogenesis. *Cell Metabolism* 5: 151-156, 2007.

144. **Ristow M, Zarse K, Oberbach A, Kloting N, Birringer M, Kiehntopf M, Stumvoll M, Kahn C, and Bluher M**. Antioxidants prevent health-promoting effects of physical exercise in humans. *Proceedings of the National Academy of Science* 106: 8665-8670, 2009.

145. **Robertson R**. Chronic oxidative stress as a central mechanism for glucose toxicity in pancreatic islet beta cells in diabetes. *Journal of Biological Chemistry* 279: 42351-42354, 2004.

146. **Romanello V, Guadagnin E, Gomes L, Roder I, Sandri C, Petersen Y, Milan G, Masiero E, Del Piccolo P, Foretz M, Scorrano L, Rudolf R, and Sandri M**. Mitochondrial fission and remodelling contributes to muscle atrophy. *EMBO J* 29: 1774-1785, 2010.

147. **Rump J, Braun J, Papazoglou S, Taupitz M, and Sack I**. Alterations of the proton-T2 time in relaxed skeletal muscle induced by passive extremity flexions. *Journal of Magnetic Resonance Imaging* 23: 541-546, 2006.

148. **Samorajski T, Delaney C, Durham L, Ordy JM, Johnson JA, and Dunlap WP**. Effect of exercise on longevity, body weight, locomotor performance, and passive-avoidance memory of C57BL/6J mice. *Neurobiology of Aging* 6: 17-24, 1985.

149. **Samuels DC**. Mitochondrial AZT metabolism. *IUBMB Life* 58: 403-408, 2006.

150. **Scaduto Jr RC, and Grotyohann LW**. Measurement of Mitochondrial Membrane Potential Using Fluorescent Rhodamine Derivatives. *Biophysical Journal* 76: 469-477, 1999.

151. **Scheffler IE**. *Mitochondria*. Hoboken, New Jersey: J. Wiley and Sons, Inc, 2008.

152. **Schenkman K, Marble D, Burns D, and Feigl E**. Myoglobin oxygen dissociation by multiwavelength spectroscopy. *Journal of Applied Physiology* 82: 86-92, 1997.

153. **Schenkman K, Marble D, Burns D, and Feigl E**. Optical Spectroscopic Method for in Vivo Measurement of Cardiac Myoglobin Oxygen Saturation. *Applied Spectroscopy* 53: 332-338, 1999.

154. **Schenkman KA**. Cardiac performance as a function of intracellular oxygen tension in buffer-perfused hearts. *American Journal of Physiology - Heart and Circulatory Physiology* 281: H2463-H2472, 2001.

155. **Schenkman KA, Marble DR, Feigl EO, and Burns DH**. Near-Infrared Spectroscopic Measurement of Myoglobin Oxygen Saturation in the Presence of Hemoglobin Using Partial Least-Squares Analysis. *Appl Spectrosc* 53: 325-331, 1999.

156. **Schmidt-Neilsen K, and Larimer JL**. Oxygen Dissociation Curves of Mammalian Blood in Relation To Body Size. *American Journal of Physiology -- Legacy Content* 195: 424-428, 1958.

157. **Schriner SE, Linford NJ, Martin GM, Treuting P, Ogburn CE, Emond M, Coskun PE, Ladiges W, Wolf N, Van Remmen H, Wallace DC, and Rabinovitch PS**. Extension of Murine Life Span by Overexpression of Catalase Targeted to Mitochondria. *Science* 308: 1909-1911, 2005.

158. **Siegel MP, Kruse SE, Knowels G, Salmon A, Beyer R, Xie H, Van Remmen H, Smith SR, and Marcinek DJ**. Reduced Coupling of Oxidative Phosphorylation In Vivo Precedes Electron Transport Chain Defects Due to Mild Oxidative Stress in Mice. *PLOS ONE* 6: e26963, 2011.

159. **Skulachev V**. Role of uncoupled and non-coupled oxidations in maintenance of safely low levels of oxygen and its one-electron reductants. *Quarterly Reviews of Biophysics* 29: 169-202, 1996.

160. **Skulachev VP**. Bioenergetic aspects of apoptosis, necrosis and mitoptosis. *Apoptosis* 11: 473-485, 2006.

161. **Sohal RS, and Allen RG**. Oxidative stress as a causal factor in differentiation and aging: a unifying hypothesis. *Experimental Gerontology* 25: 499-522, 1990.

162. **Sohal RS, and Orr WC**. The redox stress hypothesis of aging. *Free Radical Biology and Medicine* 52: 539-555, 2012.

163. **Sohal RS, and Sohal BH**. Hydrogen peroxide release by mitochondria increases during aging. *Mechanisms of Ageing and Development* 57: 187-202, 1991.

164. **Speakman J, Talbot D, Selman C, Snart S, McLaren J, Redman P, Krol E, Jackson D, Johnson M, and Brand M**. Uncoupled and surviving: individual mice with high metabolism have greater mitochondrial uncoupling and live longer. *Aging Cell* 2004.

165. **St-Pierre J, Buckingham J, Roebuck S, and Brand M**. Topology of Superoxide Production from Different Sites in the Mitochondrial Electron Transport Chain. *The Journal of Biological Chemistry* 277: 44784-44790, 2002.

166. **St-Pierre J, Drori S, Uldry M, Silvaggi J, Rhee J, Jager S, Handschin C, Zheng K, Lin J, Yangg W, Simon D, Bachoo R, and Spiegelman B**. Suppression of Reactive Oxygen Species and Neurodegeneration by the PGC-1 Transcriptional Coactivators. *Cell* 127: 397-408, 2006.

167. **Starkov AA**. The Role of Mitochondria in Reactive Oxygen Species Metabolism and Signaling. *Annals of the New York Academy of Sciences* 1147: 37-52, 2008.

168. **Stoetzer OJ, Pogrebniak A, Pelka-Fleischer R, Hasmann M, Hiddemann W, and Nuessler V**. Modulation of apoptosis by mitochondrial uncouplers: apoptosis-delaying features despite intrinsic cytotoxicity. *Biochemical Pharmacology* 63: 471-483, 2002.

169. **Sutton JR, Toews CJ, Ward GR, and Fox IH**. Purine metabolism during strenuous muscular exercise in man. *Metabolism* 29: 254-260, 1980.

170. **Szeto H**. Cell-permeable, mitochondrial-targeted, peptide antioxidants. *The AAPS Journal* 8: E277-E283, 2006.

171. **Szeto HH**. Development of Mitochondria-targeted Aromatic-cationic Peptides for Neurodegenerative Diseases. *Annals of the New York Academy of Sciences* 1147: 112-121, 2008.

172. **Szeto HH**. Mitochondria-Targeted Cytoprotective Peptides for Ischemia–Reperfusion Injury. *Antioxidants & Redox Signaling* 10: 601-620, 2008.

173. **Szeto HH, Liu S, Soong Y, Wu D, Darrah SF, Cheng F-Y, Zhao Z, Ganger M, Tow CY, and Seshan SV**. Mitochodria-Targeted Peptide Accelerates ATP Recovery and Reduces Ischemic Kidney Injury. *Journal of the American Society of Nephrology* 2011.

174. **Taylor D, Bore P, Styles P, Gadian D, and Radda G**. Bioenergetics of intact human muscle. A 31P nuclear magnetic resonance study. *Molecular Biology & Medicine* 1: 77-94, 1983.

175. **Toime L, and Brand M**. Uncoupling protein-3 lowers reactive oxygen species production in 3 isolated mitochondria. *Free Radical Biology & Medicine* 49: 606-611, 2010.

176. **Towler MC, and Hardie DG**. AMP-Activated Protein Kinase in Metabolic Control and Insulin Signaling. *Circulation Research* 100: 328-341, 2007.

177. **Turturro A, Witt WW, Lewis S, Hass BS, Lipman RD, and Hart RW**. Growth curves and survival characteristics of the animals used in the Biomarkers of Aging Program. *J Gerontol A Biol Sci Med Sci* 54: B492-501, 1999.

178. **Van Slyke DD, Hiller A, Weisiger JR, Cruz WO, and Plazin WttaoJ**. Determination of carbon monoxide in blood and of total and active hemoglobin by carbon monoxide capacity, inactive hemoglobin and methemoglobin contents of normal human blood. *Journal of Biological Chemistry* 166: 121-148, 1946.

179. **Vidal-Puig A, Solanes G, Grujic D, Flier JS, and Lowell BB**. UCP3: An Uncoupling Protein Homologue Expressed Preferentially and Abundantly in Skeletal Muscle and Brown Adipose Tissue. *Biochemical and Biophysical Research Communications* 235: 79-82, 1997.

180. **Volpi E, Nazemi R, and Fujita S**. Muscle tissue changes with aging. *Current Opinion in Clinical Nutrition & Metabolic Care* 7: 405-410, 2004.

181. **Wanagat J, Dai D-F, and Rabinovitch P**. Mitochondrial oxidative stress and mammalian healthspan. *Mechanisms of Ageing and Development* 131: 527-535, 2010.

182. **Wang H, Liu D, Cao P, Lecker S, and Hu Z**. Atrogin-1 affects muscle protein synthesis and degradation when energy metabolism is impaired by the antidiabetes drug berberine. *Diabetes* 59: 1879-1889, 2010.

183. **Wang L, Mascher H, Psilander N, Blomstrand E, and Sahlin K**. Resistance exercise enhances the molecular signaling of mitochondrial biogenesis induced by endurance exercise in human skeletal muscle. *Journal of Applied Physiology* 111: 1335-1344, 2011.

184. **Wang LC, and Kernell D**. Fibre type regionalisation in lower hindlimb muscles of rabbit, rat and mouse: a comparative study. *Journal of Anatomy* 199: 631-643, 2001.

185. **Wang W, Fang H, Groom L, Cheng A, Zhang W, Liu J, Wang X, Li K, Han P, Zheng M, Yin J, Wang W, Mattson MP, Kao JPY, Lakatta EG, Sheu S-S, Ouyang K, Chen J, Dirksen RT, and Cheng H**. Superoxide Flashes in Single Mitochondria. *Cell* 134: 279-290, 2008.

186. **Weldy CS, White CC, Wilkerson H-W, Larson TV, Stewart JA, Gill SE, Parks WC, and Kavanagh TJ**. Heterozygosity in the glutathione synthesis gene Gclm increases sensitivity to diesel exhaust particulate induced lung inflammation in mice. *Inhalation Toxicology* 23: 724-735, 2011.

187. **White CC, Krejsa CJ, Eaton DL, and Kavanagh TJ**. HPLC-Based Assays for Enzymes of Glutathione Biosynthesis. In: *Current Protocols in Toxicology*John Wiley & Sons, Inc., 2001.

188. **Wilson M-MG, and Morley JE**. Invited Review: Aging and energy balance. *Journal of Applied Physiology* 95: 1728-1736, 2003.

189. **Wiseman R, Moerland T, Chase P, Stuppard R, and Kushmerick M**. High-performance liquid chromatographic assays for free and phosphorylated derivatives of the creatine analogues beta-guanidopropionic acid and 1-carboxy-methyl-2-iminoimidazolidine (cyclocreatine). *Analytical Biochemistry* 204: 383-389, 1992.

190. **Wittenberg BA, and Wittenberg JB**. Myoglobin-mediated oxygen delivery to mitochondria of isolated cardiac myocytes. *Proceedings of the National Academy of Sciences* 84: 7503-7507, 1987.

191. **Wittenberg BA, and Wittenberg JB**. Transport of Oxygen in Muscle. *Annual Review of Physiology* 51: 857-878, 1989.

192. **Yang L, Zhao K, Calingasan NY, Luo G, Szeto HH, and Beal MF**. Mitochondria Targeted Peptides Protect Against 1-Methyl-4-Phenyl-1,2,3,6-Tetrahydropyridine Neurotoxicity. *Antioxidants & Redox Signaling* 11: 2095-2104, 2009.

193. **Yfanti C, Akerstrom T, Nielsen S, Nielsen AR, Mounier R, Mortensen OH, Lykkesfeldt J, Rose AJ, Fischer CP, and Pedersen BK**. Antioxidant supplementation does not alter endurance training adaptation. *Med Sci Sports Exerc* 42: 1388-1395, 2010.

194. **Zarse K, Schmeisser S, Groth M, Priebe S, Beuster G, Kuhlow D, Guthke R, Platzer M, Kahn CR, and Ristow M**. Impaired Insulin/IGF1 Signaling Extends Life Span by Promoting Mitochondrial L-Proline Catabolism to Induce a Transient ROS Signal. *Cell Metabolism* 15: 451-465, 2012.

195. **Zhang X, Toronov V, and Webb A**. Simultaneous integrated diffuse optical tomography and functional magnetic resonance imaging of the human brain. *Optics Express* 13: 5513-5521, 2005.

196. **Zhao K, Zhao G-M, Wu D, Soong Y, Birk AV, Schiller PW, and Szeto HH**. Cell-permeable Peptide Antioxidants Targeted to Inner Mitochondrial Membrane inhibit Mitochondrial Swelling, Oxidative Cell Death, and Reperfusion Injury. *Journal of Biological Chemistry* 279: 34682-34690, 2004.

197. **Zong H, Ren JM, Young LH, Pypaert M, Mu J, Birnbaum MJ, and Shulman GI**. AMP kinase is required for mitochondrial biogenesis in skeletal muscle in response to chronic energy deprivation. *Proc Natl Acad Sci U S A* 99: 15983-15987, 2002.

198. **Zurlo F, Larson K, Bogardus C, and Ravussin E**. Skeletal muscle metabolism is a major determinant of resting energy expenditure. *J Clin Invest* 86: 1423-1427, 1990.

Vita

Michael Patrick Siegel

Education

Doctor of Philosophy in Bioengineering 2012
University of Washington – Seattle, WA

Master of Science in Biomedical Engineering 2005
Northwestern University – Evanston, IL

Bachelor of Science in Biomedical Engineering 2002
Washington University – St. Louis, MO

Publications

Siegel MP, Wilbur T, Mathis CM, Shankland EG, Trieu A, Harper ME, Marcinek DJ. "Impaired Adaptability of In Vivo Mitochondrial Energetics to Acute Oxidative Insult in Aged Skeletal Muscle." *Mechanisms of Ageing and Development*. Under Review, May 2012

Siegel MP, Kruse SE, Knowels G, Salmon A, Beyer R, Xie H, Van Remmen H, Smith SR, Marcinek DJ. "Reduced Coupling of Oxidative Phosphorylation In Vivo Precedes Electron Transport Chain Defects Due to Mild Oxidative Stress in Mice." *PLoS ONE*, November 2011; 6(11): e26963.

Siegel MP, Kim YL, Roy HK, Wali RK, Backman V. "Assessment of Blood Supply in Superficial Tissue by Polarization Gated Elastic Light Scattering Spectroscopy." *Applied Optics*, January 2006; 45(2): 335-342.

Kamper DG, Cruz EG, **Siegel MP**. "Stereotypical Fingertip Trajectories During Grasp." *Journal of Neurophysiology*, December 2003; 90(6): 3702-3710.